A Search for Strange Quark Matter in the -0.75T Field Setting of E864

by

Gene Edward Van Buren

B.S. Physics, B.S. Electrical Engineering
Washington University in Saint Louis (1993)

Submitted to the Department of Physics
in partial fulfillment of the requirements for the degree of

Doctor of Philosophy in Physics

at the

MASSACHUSETTS INSTITUTE OF TECHNOLOGY

June 1998

Author .....
Department of Physics
June 30, 1998

Certified by ....
Irwin A. Pless
Professor
Thesis Supervisor

Accepted by .....
Thomas J. Greytak
Associate Department Head for Education

A Search for Strange Quark Matter in the -0.75T Field Setting of E864

by

Gene Edward Van Buren

Submitted to the Department of Physics
on June 30, 1998, in partial fulfillment of the
requirements for the degree of
Doctor of Philosophy in Physics

Abstract

E864 was designed as a high sensitivity search for strange quark matter produced in heavy ion collisions at the AGS accelerator at Brookhaven National Laboratory. In this thesis, we analyze data taken at the -0.75T field setting of the experiment, which is optimal for finding negatively charged strangelet candidates, from Au + Pt collisions at 11.6 GeV/c per nucleon. A measurement of the antiproton invariant multiplicities is made and is in reasonable agreement with previous E864 antiproton measurements. No conclusive strangelet candidates are found, and upper limits are set on the production of charge -1 and charge -2 strangelets of approximately 1×10^{-8} and 4×10^{-9} per 10% central collision respectively. These represent world's best limits to date.

Thesis Supervisor: Irwin A. Pless
Title: Professor

Acknowledgments

Zhangbu Xu deserves much credit for his well-thought observations and recommendations for all of us who tried to analyze E864 data. By the same token, Jamie Nagle contributed to every detail he could on the experiment - it usually helped, and E864 and its analyses are better for it. But before them were the folks who paved the way for E864 analysis. Ken Barish and John Lajoie not only were the first to push the data through, but stuck around to help others out too. Thanks go to Rob Hoversten for working with me on preparing for the run and doing some of the calibrations.

At MIT, Jeff Tomasi and Aaron Tustin helped out in many ways during their UROPs. Haridas deserves credit for all the hard work he put into building and testing the beam counters with me. And Mario Bertaina was much more helpful than he will ever admit down the stretch. I most certainly owe gratitude to my advisor, Irwin Pless, who took me on before I was even a student at MIT, was patient through my exams, and constantly pushed me to think things through for myself.

I also want to thank those who gave a young scientist an opportunity to learn physics outside the classroom before I ever came to MIT: Richard Haglund, Alan Barnes, Randy Ruchti, and Lee Sobotka.

To the E864 collaboration as a whole, from whom there were too many favors to enumerate, and to our "heroic" spokesman, Jack Sandweiss, I give thanks for the experiment which made this thesis possible.

E864 Collaboration

G. De Cataldo, N. Giglietto, A. Raino, P. Spinelli
University of Bari/INFN

C.B. Dover[†]
Brookhaven National Laboratory

K.N. Barish, H.Z. Huang
University of California, Los Angeles

J.C. Hill, R.A. Hoversten, J.G. Lajoie, B.P. Libby, F.K. Wohn
Iowa State University

M. Bertaina, P. Haridas, I.A. Pless, G. Van Buren
Massachusetts Institute of Technology

T.A. Armstrong, R.A. Lewis, G.A. Smith, W.S. Toothacker
Pennsylvania State University

R.R. Davies, A.S. Hirsch, N.T. Porile, A. Rimai,
R.P. Scharenberg, M.L. Tincknell
Purdue University

M.S.Z. Rabin
University of Massachusetts

T. Lainis
United States Military Academy

S.V. Greene, T. Miller, J.D. Reid, A. Rose

Vanderbilt University

S.J. Bennett, T.M. Cormier, P. Dee, P. Fachini, B. Kim, Q. Li, Y. Li,
M.G. Munhoz, C.A. Pruneau, W.K. Wilson, K.H. Zhao

Wayne State University

S. Batsouli, A. Chikanian, S.D. Coe, G.E. Diebold, W. Emmet, L.E. Finch,
N.K. George, B.S. Kumar, R.D. Majka, J.L. Nagle, J.K. Pope, F.S. Rotondo,
J. Sandweiss, A.J. Slaughter, E. Wolin, Z. Xu

Yale University

† Deceased

Vita

Gene Van Buren was born in Delaware, Ohio on April 30, 1971. His parents, Paul Van Buren and Donna Lou Van Buren, were home between mission assigments with the United Methodist Church in the Philippines. Gene and his three elder siblings, Mark, Lisa, and Randy, lived in the Mindanao region of the Philippines from 1971 until 1975.

After living in several Ohio communities, Gene's family moved to Nashville, Tennessee in 1985, where he attended John Overton Comprehensive High School. Gene was named an honorary member of the Tennessee State House of Representatives and received an official Recognition of Honor from the state legislature before finishing high school as valedictorian.

From 1989 through 1993 Gene attended the Engineering School at Washington University in Saint Louis as a Langsdorf Fellow. He completed bachelors degrees in Physics and Electrical Engineering along with an exhaustive Computer Science minor and graduated magna cum laude.

Gene pursued graduate studies in high energy physics at the Massachusetts Institute of Technology from 1993 until 1998. He finished his dissertation on "A Search for Strange Quark Matter in the -0.75T Field Setting of E864" before marrying Marie Castro on July 11, 1998.

For my parents and family, who brought a smile to my face nearly every day with emails from around the world.

For Marie...

Contents

List of Figures

List of Tables

Chapter 1

Introduction

1.1 Motivations

1.1.1 Quark Matter and Strange Quark Matter

Kendall, Friedman, and Taylor discovered the existence of quarks nearly three decades ago. Their work ushered in the age of quark matter. The simplest forms of quark matter are composed predominantly of up (u) and down (d) quarks like those observed by Kendall, Friedman, and Taylor. Since then four additional quark types, or flavors, have been found. Of these, the u and d quarks are the lightest. The next lightest quark is called the strange (s) quark. At higher masses lie the charm (c), bottom (b), and top (t) quarks. The t quark has only just recently been discovered, and is believed to be the last of the line.

The heavier quarks are able to shed mass through decay processes which convert them into lower mass quarks. The u and d quarks are at the bottom of this decay chain and so cannot decay further. Quarks can also be made through pair production, following Einstein's famous formula $E = mc^2$, where a quark and its antimatter complement are created from available energy. Because the u and d quarks are so light - in fact, nearly massless - they are the easiest of the quarks to create this way. These two reasons are why u and d quarks are the most prevalent in the world in which we live. Ordinary atomic nuclei, which account for nearly the entire mass of

any atom, are simply collections of protons and neutrons, objects which contain only the u and d quarks.

Another property has been given to quarks to explain the nature of the systems in which quarks have been found. This property is called color. A quark can have any one of three colors, and antiquarks can have any of the three anti-colors. The combination of a color and its anti-color, or of all three colors or anti-colors, is termed a "color-singlet" state. Thus, a quark and an antiquark with matching color/anti-color can be put together in one object. Such objects are called mesons. Alternatively, three quarks, each with a different color, can combine to form objects known as baryons. All objects which interact through the same forces as mesons and baryons fall under the class of hadrons.

Quarks have never been observed outside of a color-singlet state. Additionally, no conclusive evidence has been found for color-singlet states larger than baryons. Yet the current understanding of quarks does not prohibit larger systems of quarks within a single object from occurring. One can imagine a much larger system with many quarks which still forms a color-singlet state. If no antiquarks are included, then the number of quarks in such a system must be a multiple of 3. Thus, the system is defined to have 3A quarks, where A is the *baryon number* of the system as it represents the size of the system in terms of a single baryon, which has only 3 quarks. Such a system of quarks is referred to as quark matter (QM).

There are certain principles, however, which can make large QM systems less favorable than simple baryons. In particular, the Pauli exclusion principle stipulates that no two fermions (a class of objects which includes the quarks) in a single system may occupy the same quantum state. In the case of quarks (ignoring the possibility of antiquarks), the quantum state is essentially defined by spin (of which there are two possible states for a quark), flavor (6 states), color (3 states), and energy level. For a small system of quarks, the total energy of the system (including the masses of the quarks inside) is minimized by using the light u and d quarks. Such quark matter is called *non-strange quark matter*. But for a system of many quarks, one must either add quarks to the system which are in a very high energy level, or have a different

flavor. At some point, the addition of the next lightest quark, the s quark, becomes more favorable than adding another u or d quark in some highly excited energy state. Quark matter which contains s quarks is called *strange quark matter* (SQM).

1.1.2 Strangelets

After the discovery of quarks, many predictions were made for the existence of large systems of SQM [2, 3, 4, 5, 6, 7]. In particular, Witten proposed stable, bound systems on astronomical scales, such as neutron stars [6], before Farhi and Jaffe [8] began studying systems of smaller sizes ($A \leq 10^7$, and in particular $A \leq 10^2$) using the recently formulated MIT Bag Model of quark containment [9]. They termed these smaller systems of strange quark matter *strangelets*, and the possible properties of these objects, their decay modes and regions of mass, charge, and strange quark content required for stability, were soon explored in greater detail [10, 11, 12]. Some even predicted the possibility of actually producing strangelets in the laboratory, in the dense medium of heavy ion collisions [3].

A hypothetical strangelet is depicted in Figure 1-1. Shown side-by-side are a ^{12}C nucleus with 36 u and d quarks arranged in neutrons and protons, and a strangelet of the same baryon number ($A = 12$). The roughly equivalent numbers of u, d, and s quarks, which carry charges of +2/3, -1/3, and -1/3 that of a proton respectively, lead to a distinctive property of strangelets: low charge-to-mass ratios. This property is the basis for all present strangelet searches.

If indeed strangelets exist, the implications are very important to the fields of cosmology, and nuclear and particle physics. Strangelet production may be a signature of the quark gluon plasma (QGP), a predicted, but as yet undetected phase of nuclear matter at very high energy densities in which quarks are no longer confined [13]. It is believed that the formation of strangelets is much more probable among the unbound, and theoretically strangeness-rich quarks of a QGP. The discovery of the QGP is one of the major focuses of high energy heavy ion physics today.

If a QGP is produced in a heavy ion collision, its lifetime is only expected to be on the order of 10^{-22} seconds. A QGP must therefore be detected indirectly through

Strange Quark Matter

Stable or metastable massive multiquark states involving u,d and s quarks.

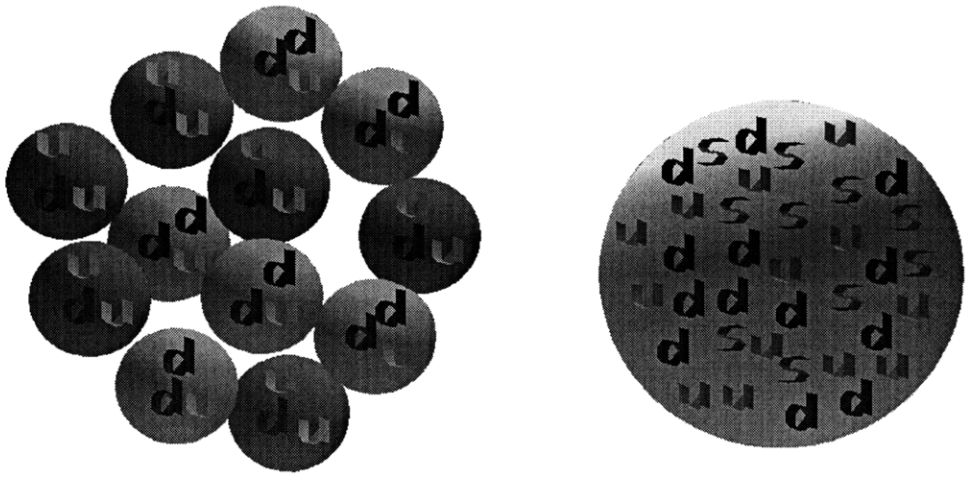

Artist's Interpretation

Nuclear Matter	Strange Matter
(Carbon)	(Strangelet)
Z=6	Z=1
A=12	A=12 (36 quarks)
Z/A=1/2	Z/A=0.083
	N_S=10, f_S=N_S/A=.83

Figure 1-1: A hypothetical strangelet with the same baryon number as a ^{12}C nucleus. The strangelet is characterized by a very low charge-to-mass ratio (Z/A).

its remnants, or its effects on other observables in final products of the collision. For example, at beam momenta like those produced at the Alternating Gradient Synchrotron (AGS) at Brookhaven National Laboratory (on the order of 10 GeV/c per nucleon), nucleons in the target and beam are believed to "stop" in the center of mass frame for very central collisions. If a QGP forms in this impact region of dense baryons, it will have a significant constituency of u and d quarks from the original nuclei. Of course, the high energy densities in this region will also lead to a great deal of quark pair production. This leads to equal numbers of strange and antistrange quarks in the early stages of the QGP. The excess of u and d quarks makes it easier for anti-strange ($\bar{s}$) quarks to pair up in mesons which may escape the QGP than for s quarks. This distillation of the QGP into a strangeness-rich system is expected to be a favorable environment for strangelets, which are predicted to have roughly equal numbers of u, d, and s quarks. Thus, if strangelets are observed in heavy ion collisions, they may be a "smoking gun" signal of QGP existence.

Even more consequential is the possibility that SQM could be the true ground state of matter. This would only be confirmed by observation of strangelets with lower energy densities than typical nucleons. If such strangelets exist, they would be stable against strong nuclear decays (whereby nucleons are emitted from the strangelet) because this would only serve to further reduce the energy density of the remaining strangelet. Strangelets of this nature might grow arbitrarily large in size.

While QGPs may be the only way to produce large strangelets in the laboratory, there are reasons to believe that smaller strangelets can be built up through coalescence. Coalescence describes the process whereby nucleons which leave the collision zone relatively close to each other in phase space may join together. The model asserts that the joining of each additional nucleon suffers a penalty factor in probability. An additional strangeness penalty factor is applied for each strange quark included in the system [14].

Recent results from heavy ion collisions show strong support for the coalescence model in the formation of light nuclei [15, 16]. Although early estimates for the strangeness penalty factor have been found to be optimistic, using rough factors

with the model allows simple coalescence estimates for the probability of strangelet production in heavy ion collisions of the order $10^{3-A-|S|}$, where A is the baryon number of the object we wish to coalesce, and S denotes the strangeness content [17]. This formula expresses both penalty factors as a single order of magnitude. Even this optimistic probability calculation impresses the point that large, highly strange objects are difficult to produce this way.

While early speculation on what charges and masses for stable or meta-stable strangelets indicated that neutral, and lightly positively charged objects would be favorable, recent calculations have actually run contrary, pointing towards improved stability at negative charges [17]. Strangelet experiments have until this point spent more effort on searching for positive candidates. But there are several experiments which have already conducted searches for strangelets with negative charges. These experiments are described briefly below.

1.2 History of Negative Strangelet Searches

E858

The first search for negatively charged strangelets was conducted in 1990 with the E858 focusing spectrometer at the AGS. Collisions of Si + Au at 14.6 GeV/c were examined, and upper limits were set in a range between 2×10^{-10} and 1×10^{-8} per interaction for production of negatively charged strangelets with masses between A = 2 and A = 15 [18].

E886

Experiment E886 ran during the fall of 1993 and looked for negative strangelets in a focusing spectrometer. They studied Au + Pt collisions at 10.8 GeV/c using an AGS beam line for rigidity (P/Z) selection. Maximum rigidity for the experiment was 1.7 GeV/c, which meant that massive objects could only be detected at very low rapidities. Their quoted negative strangelet limits are of the order 10^{-8} per interaction but are highly production model dependent [19].

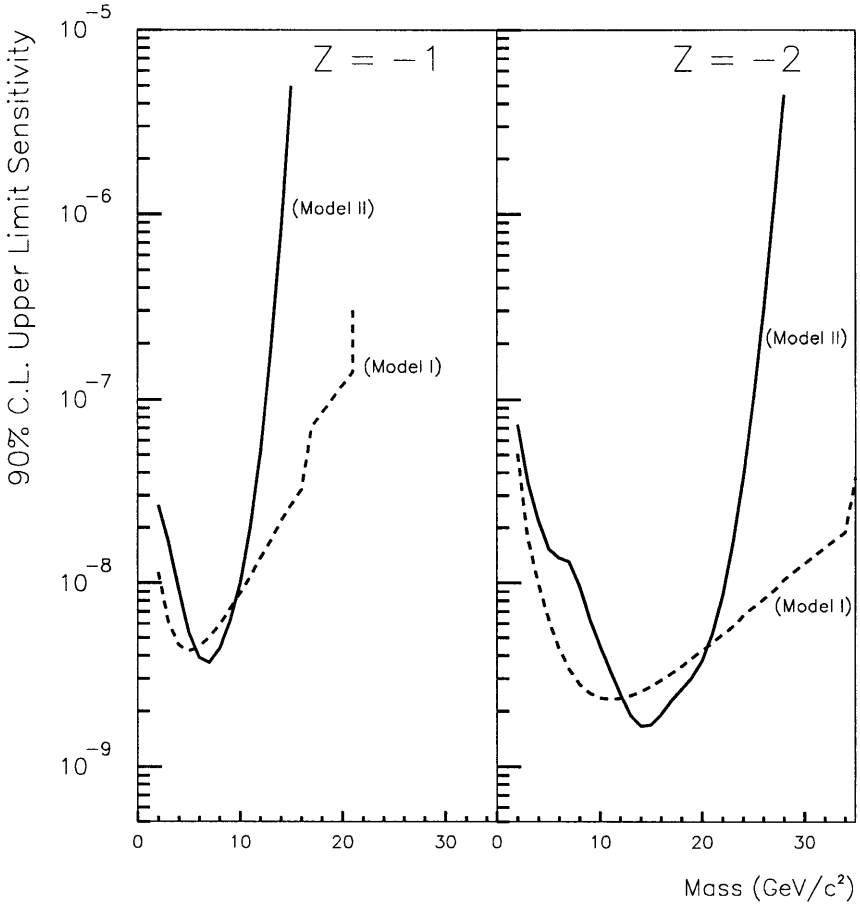

Figure 1-2: Negatively charged strangelet upper limits from the E878 experiment. Upper limits are shown for two production models at both charge -1 and charge -2.

E878

During the same AGS running period, E878 examined negatively charged strangelets in Au + Au collisions using a two-segment focusing spectrometer. They were able to run with a much wider range of rigidities, which made their acceptance much less model dependent than E886. However, acceptance for very large masses was inhibited by the time-of-flight limits of the spectrometer [20]. Limits from this experiment are shown in Figure 1-2 and are at best in the 10^{-9} to 10^{-8} per interaction range.

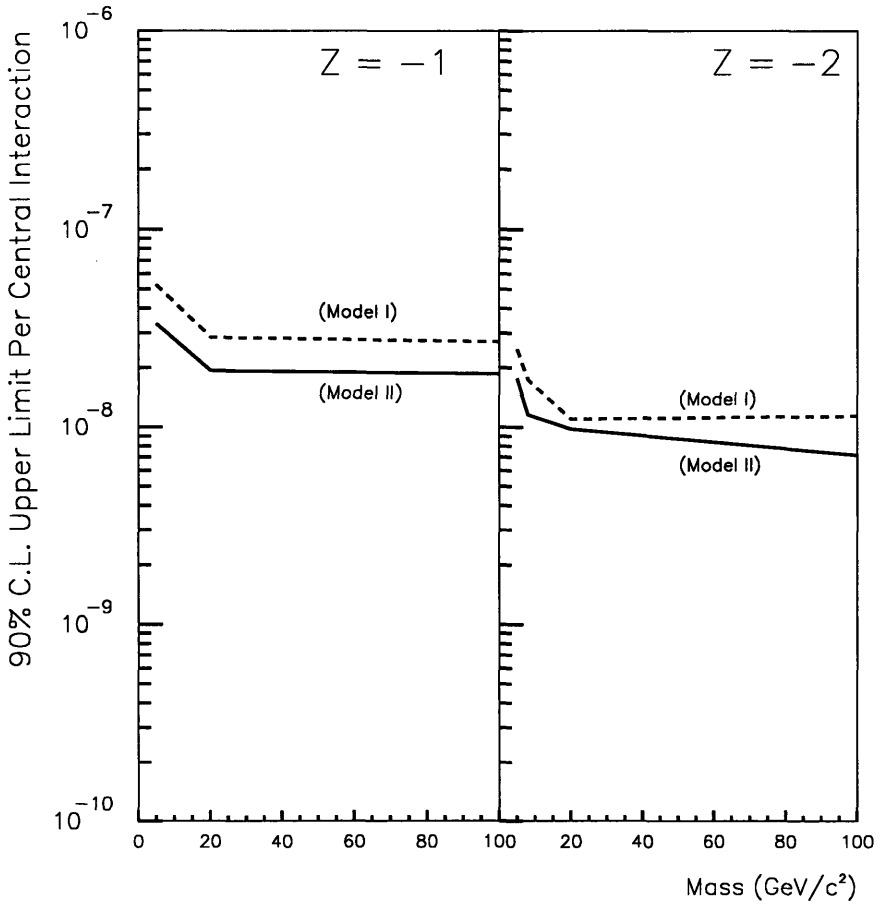

Figure 1-3: Previous negatively charged strangelet upper limits from the E864 experiment. Upper limits are shown for two production models at both charge -1 and charge -2.

E864

Experiment E864 collected data for negatively charged strangelets in 1995 at the AGS. These limits are the best to date before this analysis. E864's limits are around 10^{-8} per 10% central Au + Pb interaction at 11.6 GeV/c per nucleon [21]. The upper limits set from the 1995 run are shown in Figure 1-3.

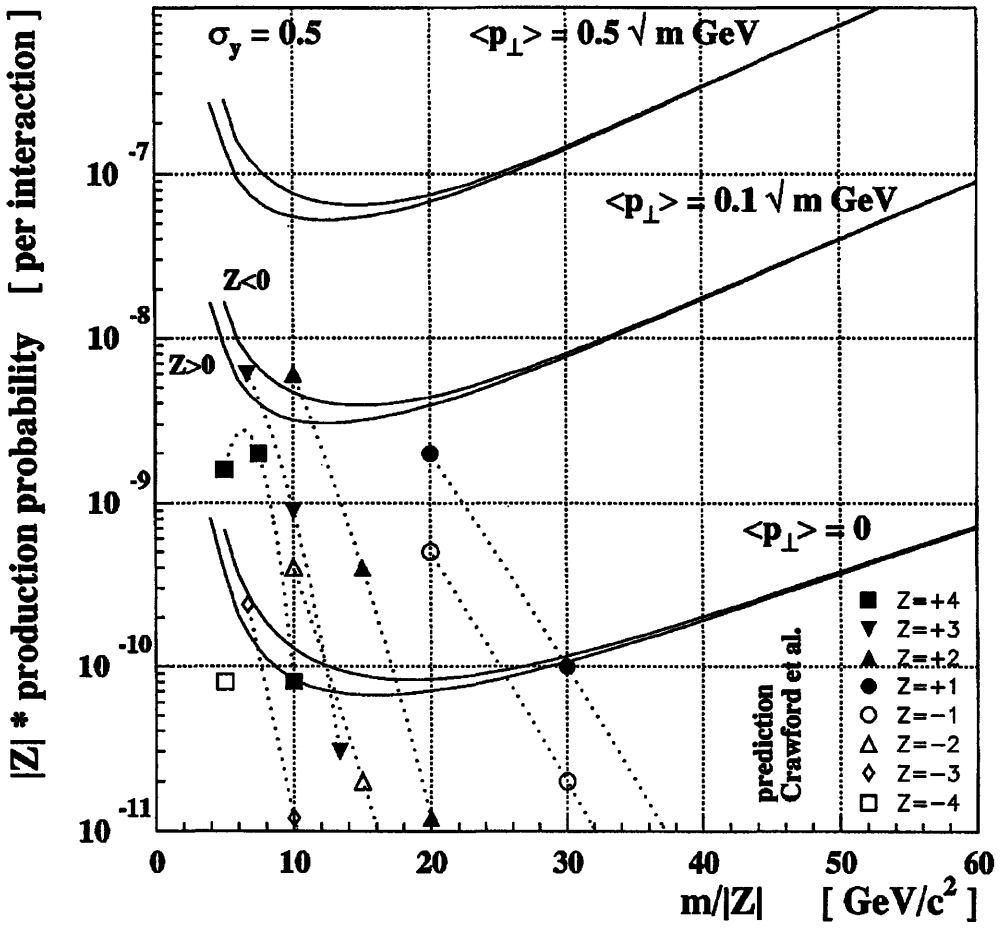

Figure 1-4: Strangelet upper limits from the NA52 experiment. The three sets of curves are for different strangelet production models. In each pair, the upper curve is for negatively charged strangelets and the lower curve is for positives.

NA52

NA52 was a strangelet search conducted at CERN using Pb + Pb at 158 GeV/c. As it was also a focusing spectrometer, its acceptance for strangelets was very production model dependent. The collaboration's best limits for negatively charged strangelets ranged from 10^{-10} to 10^{-7} depending on the model and are shown in Figure 1-4.

1.3 Goals

The intent of this thesis is to search for negatively charged strangelets in high energy heavy ion collisions, either as a byproduct of the formation of a QGP, or through coalescence. We use data taken during the 1996-1997 run of the E864 spectrometer experiment at the AGS to conduct this search. Approximately 200 million events representing 14 billion sampled collisions of Au + Pt at 11.6 A GeV/c are analyzed using the Abacus computing facility at the MIT Laboratory for Nuclear Science. The calibrated data is converted to a Data Summary Tape format which drastically improves the data storage size and processing speed efficiencies of the entire data set. To gain a better understanding of the data and our analysis methods, a measurement is made of the invariant multiplicity spectra for antiprotons produced in these collisions. The measurements are compared with previous E864 data over similar rapidity and transverse momentum ranges ($2.8 < y < 2.4$, 75 MeV/c $< p_t <$ 300 MeV/c), and new measurements for E864 are made at high rapidities ($2.4 < y < 2.6$). The data set is then analyzed for negatively charged strangelet candidates. The final sensitivity of the searches are new world's best to date.

Chapters 2 and 3 of this thesis describe the E864 experiment and the calibrations necessary to analyze data from the experiment. Chapter 4 summarizes the global results of passing through the data to create the DST. The analyses of the data for antiproton and strangelet measurements are detailed in Chapter 5. Discussion of the results of these analyses follows in Chapter 6. Chapter 7 concludes with a summary of what has been done in this thesis.

Chapter 2

Experiment

2.1 Overview

The E864 experiment was devised specifically to search for low charge to mass ratio (-1 < Z/A < +1) long-lived ($\tau \geq 50$ ns) exotic particles produced near midrapidity ($y_{cm} \pm 0.5$) in fixed target Au + Au collisions at a beam momentum of 11.6 GeV/c per nucleon [22]. At this momentum, the beam rapidity is ~3.2 in the lab frame, yielding a midrapidity of $y_{cm} = 1.6$, where $y = \tanh^{-1}(\beta_z)$.

For the purpose of this search, E864 was designed as a non-focusing spectrometer with an open geometry configuration, permitting searches over a wide range of masses simultaneously. Particle identification is performed through measurements of track rigidity ($\vec{R}$), velocity ($\beta = v/c$), and charge (Z) as follows:

$$\vec{P} = \vec{R} \cdot Z \tag{2.1}$$

$$M = \frac{|\vec{P}|}{\gamma\beta} \tag{2.2}$$

where $\vec{P}$ is the momentum of the particle, M is the mass, and $\gamma = 1/\sqrt{1-\beta^2}$. Because the experiment yields only charge and mass information on particles, it cannot distinguish particles as new which may appear with the same mass and charge as a known particle. For example, a strangelet of mass 3A, charge +1 is indistinguishable from a triton.

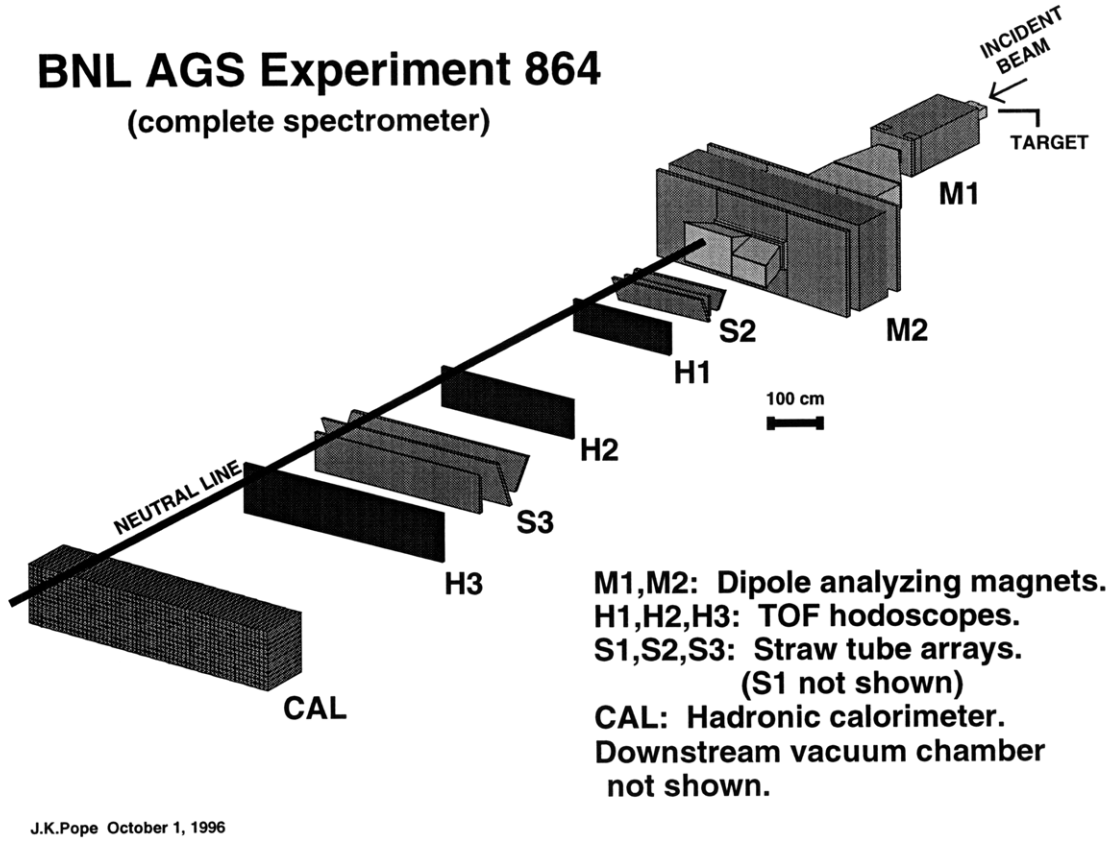

Figure 2-1: Perspective view of the E864 Spectrometer. The vacuum chamber over the downstream portion of the experiment is not shown.

The E864 experimental apparatus is located on the A3 beam line of the Alternating Gradient Synchrotron (AGS) at Brookhaven National Laboratory. A perspective view of the experiment is shown in Figure 2-1. Plan and elevation views are shown in Figure 2-2. The z axis is chosen to lie along the beam vector as it strikes the target, the y axis is along the vertical, and the x axis is along the horizontal perpendicular to the beam (in a right-handed coordinate system). With the origin at the target, the bulk of the apparatus lies in the region of positive z (downstream of the target), negative y (below the beam), and positive x (beam left).

The AGS provides an 11.6 GeV/c per nucleon beam of fully-stripped, charge +79 Au ions to the experiment. For the 1996-1997 run, a Pt target approximately

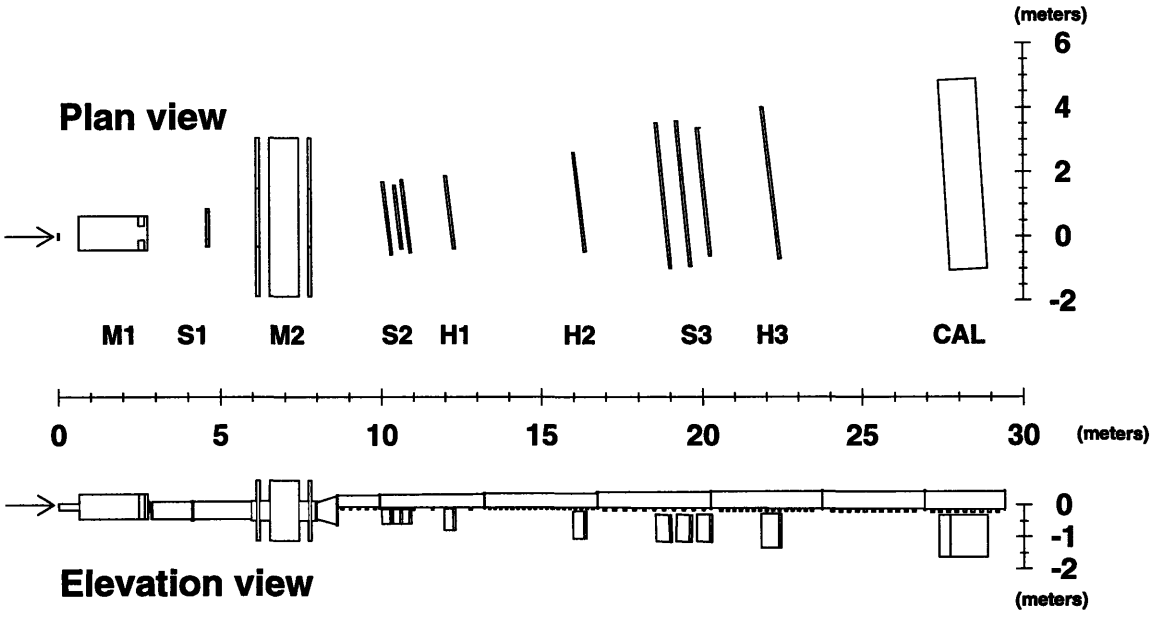

Figure 2-2: Plan and elevation views of the E864 Spectrometer. The vacuum chamber over the downstream portion of the experiment is not shown in the plan view, but can be seen as a series of large boxes above the detectors in the elevation view.

1.5 cm thick (60% of an interaction length) is used which sits in vacuum. Several beam detectors reside immediately upstream of the target, and a multiplicity detector stands just downstream of the target. These front-end components will be discussed more thoroughly in Section 2.2.

Most of the interaction products and beam fragments then continue in a vacuum chamber which extends through the two dipole bending magnets of the spectrometer (M1 and M2). Acceptance is limited in this region by a collimator inside M1, the aperture of M2, and a plug located just before M2, as shown in Figures 2-3 and 2-4. The purpose of the plug is to obscure the floor of the downstream vacuum chamber from the target so that particles do not scatter from the chamber floor into the downstream apparatus. Experimental acceptance is quite large in horizontal angles, covering -32 mr to 171 mr. Angles from -17.5 mr down to -51.3 mr are accepted in the vertical.

At this point, uninteracted beam particles remain in vacuum as they continue

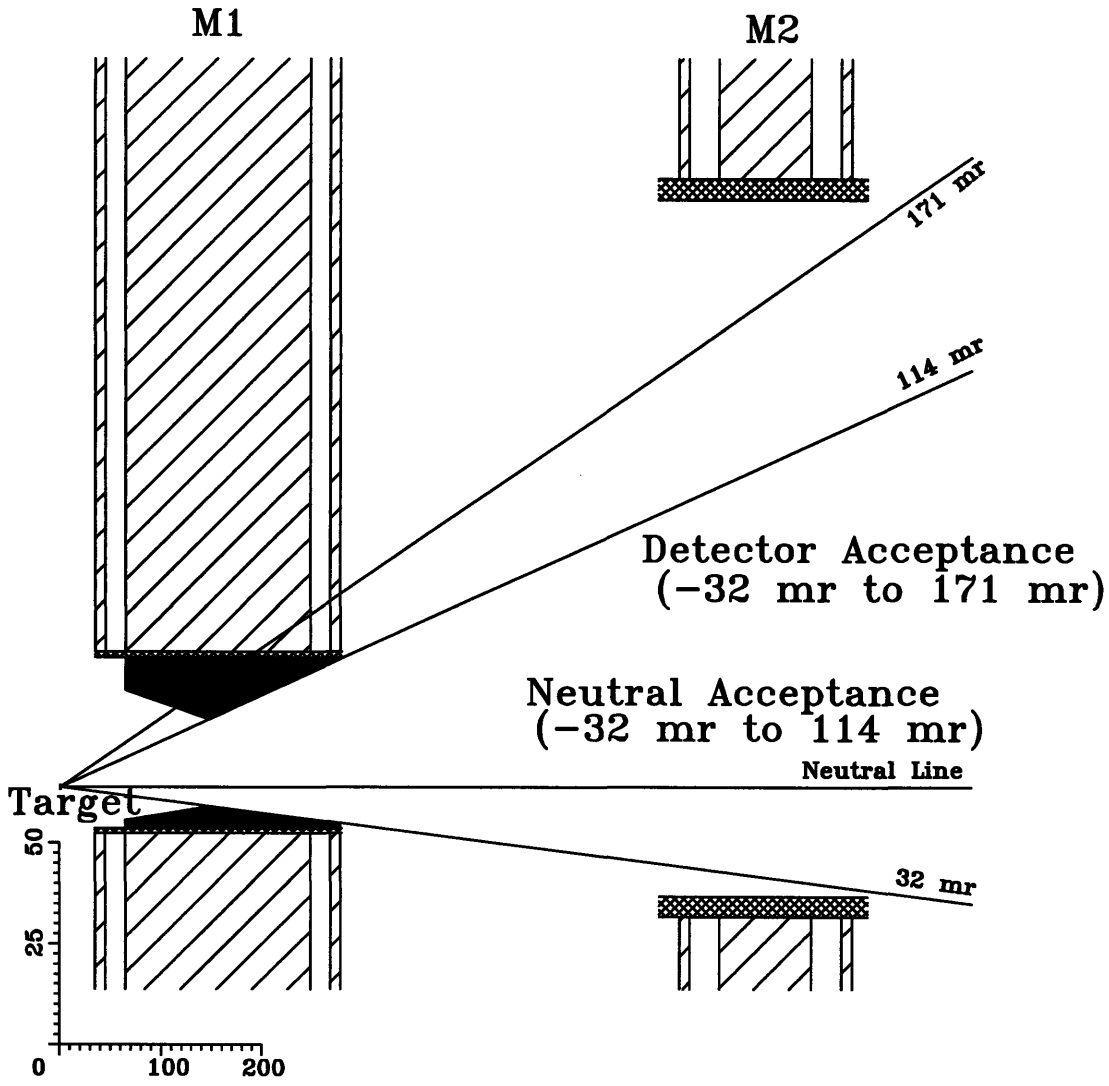

Figure 2-3: Collimation of particles from the target in the horizontal plane.

above the downstream detectors of the apparatus. This portion of the vacuum is shown in the elevation view in Figure 2-2. Since the uninteracted beam also bends in M1 and M2, this vacuum chamber expands in the x direction downstream to contain all intended beam trajectories and many of the particles which pass above the plug in collimation.

Particles of interest exit the vacuum just after M2 through a thin Mylar-Kevlar vacuum window into the downstream portion of the apparatus. This portion includes three time-of-flight scintillating hodoscope planes, three straw wire tube tracking

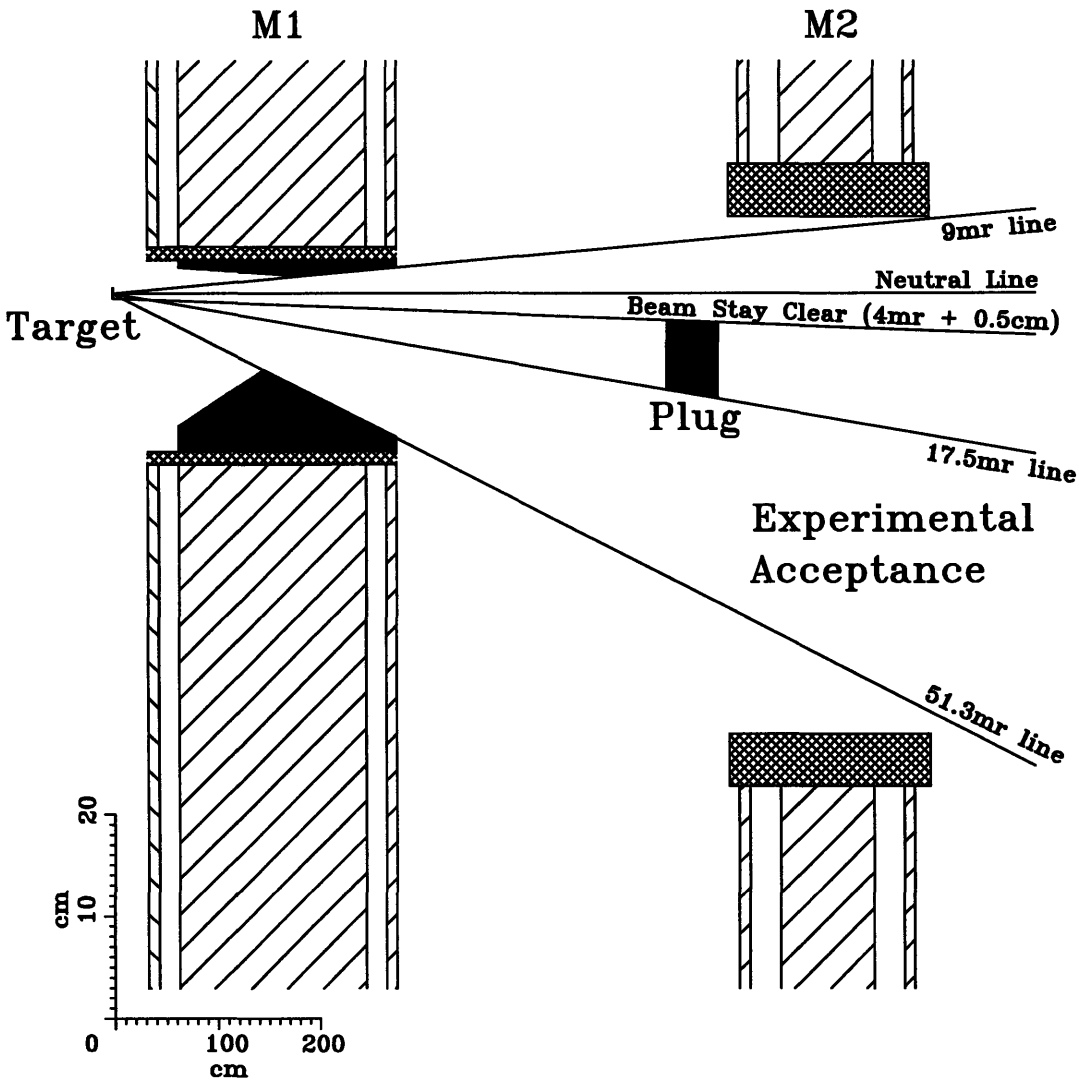

Figure 2-4: Collimation of particles from the target in the vertical plane.

stations, and an hadronic calorimeter. Detector positions and sizes are shown in Table 2.1. The hodoscopes are used for finding initial charged track candidates via linear fits to the space-time points of hits in successive planes. These candidate tracks are projected to the straw chambers to locate associated straw tube hits which can improve the accuracy of the track vector. Assuming the track comes from the target, and knowing the fields of the magnets, the track rigidities can be reconstructed.

The hodoscope linear fits also yield a velocity for the track. Additionally, the three hodoscopes are able to make triply redundant measurements of the tracked particle's

Detector	Location of Center			Size (cm)		Rotation About
	x (cm)	y (cm)	z (cm)	Horizontal	Vertical	the Vertical (mr)
S1	27.20	-21.0	473.54	101.3	25.2	0.0
S2	58.60	-36.5	1013.54	187.1	40.0	115.2
H1	73.03	-43.8	1213.54	223.5	48.0	115.2
H2	109.81	-58.4	1613.54	313.7	64.0	115.2
S3	131.40	-73.0	2013.54	411.0	80.0	115.2
H3	153.75	-80.3	2213.54	451.0	88.0	115.2
CAL	192.00	-98.7	2813.54	580.0	130.0	57.6

Table 2.1: E864 detector positions and sizes.

charge through dE/dx. This is enough information to find the mass of the particle via Equations 2.1 and 2.2.

Because the experiment suffers background from scattered particles whose rigidity is reconstructed improperly, and thus whose mass is calculated incorrectly, a redundant mass measurement can be made with the hadronic calorimeter located at the downstream end of the experiment. Typical light nuclei stop in the calorimeter depositing their kinetic energy into a shower of charged particles. The calorimeter records the energy of these showers (E) and a mass can be found with the formula

$$M = \frac{E}{\gamma - 1} \tag{2.3}$$

Different field settings in the dipole magnets alter the range of charge to mass ratios accepted in the spectrometer. For most topics of interest, both magnets are maintained at identical field settings. Table 2.2 enumerates the physics topics which are most emphasized at various standard E864 magnetic field settings. Positive fields are defined as those which bend positively charged particles towards the plus x direction, bringing them into the experimental acceptance. Similarly, negative fields bring negatively charged particles into the acceptance. Greater field strengths sweep particles with large charge to mass ratios beyond the experimental acceptance. The analysis detailed herein uses data recorded with the -0.75T field setting, which is optimal for negatively charged strangelets and antideuterons because positively charged

particles, antiprotons and other, lighter negatively charged particles tend to be swept from the acceptance.

Field Setting	Primary Physics Topics
-0.75T	Antideuterons and Negative Strangelets
-0.45T	Antiprotons and Chiral Solitons
-0.20T	Negative Kaons and Protons
+0.20T	Positive Kaons and Protons
+0.45T	Protons and Deuterons
+0.75T	Light Nuclei
+1.50T	Positive Strangelets and Rare Isotopes

Table 2.2: E864 magnetic field settings for emphasis of various physics topics.

2.2 Beam Counters

The beam counters actually consist of several different particle detectors. The presence of a beam ion is detected in Mitch and MIC, which are quartz plate Čerenkov counters. There are two hole veto counters, one used to veto off-center beam ions, and one used to veto beam ions which may have interacted upstream of the target. Downstream of the target there is a segmented scintillating interaction multiplicity counter (MULT). And downstream of the spectrometer magnets is a segmented quartz plate beam counter (MAC) used for beam tuning. The section of the spectrometer upstream of the magnets, including several of the beam counters, can be seen in Figure 2-5.

2.2.1 Beam Trigger Counter (Mitch)

The primary beam trigger counter for the experiment is a counter called Mitch (for MIT Čerenkov counter). Mitch actually performs several functions for the experiment:

1. Beam particle trigger

2. Experiment electronics gate start

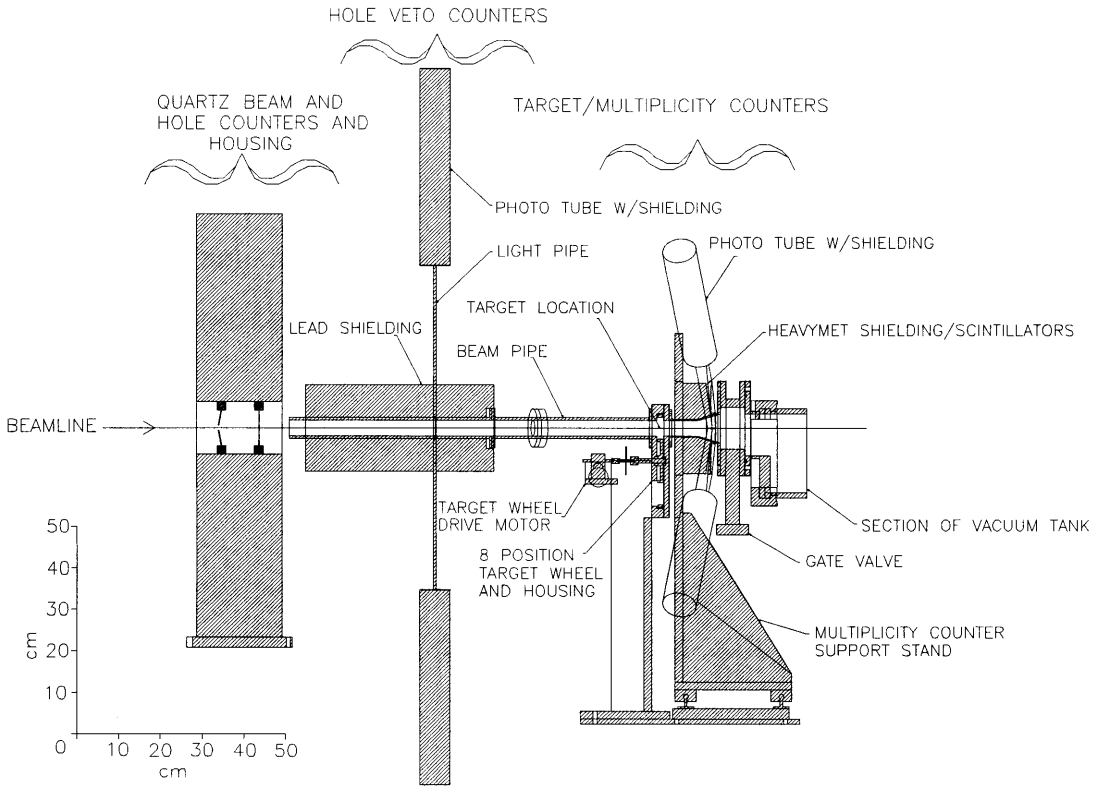

Figure 2-5: The E864 front-end assembly. Items of note are the Mitch housing (containing the quartz beam and hole veto counters), the interaction veto counter and its lead shielding, the target, and the multiplicity counter.

3. Time zero reference for time of flight measurements

4. Multiple beam rejection[1]

For Item 3, it is necessary for Mitch to have very good timing characteristics. Item 4 requires good pulse height resolution.

Optical Components

Using solid scintillator for the beam trigger counter was ruled out because of its susceptibility to radiation damage in an intense heavy ion beam. Supersil-1, the

[1]Multiple beams are when more than one beam particle enters the spectrometer while the electronics gates are active.

quartz selected for the initial incarnation of Mitch, is considered to be relatively resilient to radiation damage. And because it is free of striations along all axes, it is ideal for the production and transmission of Čerenkov light.

The original optical components of Mitch include a 5.0 cm $\times$ 8.8 cm quartz plate with a thickness of 150 μm held in a frame between upper and lower two inch diameter photomultiplier tubes (PMTs). For a beam of particles traveling at speed βc in a medium of index of refraction n, the angle to the beam at which Čerenkov light is produced follows the formula

$$\cos\theta_c = \frac{1}{n\beta c} \tag{2.4}$$

In the case of an 11.6 GeV/c per nucleon ion beam traveling through quartz with $n = 1.458$, this works out to an angle $\theta_c = 46.5°$. This angle is greater than that required for total internal reflection with a beam trajectory normal to the plane of the quartz plate:

$$\sin\theta_{IR_{min}} = \frac{n_{air}}{n_{quartz}} \tag{2.5}$$

$$\approx \frac{n_{vacuum}}{n_{quartz}} \tag{2.6}$$

which works out to be $\theta_{IR_{min}} = 43.3°$. Thus, all the Čerenkov light is internally reflected, much of it traveling to the edges at which the PMTs are located.

The frame for the quartz plate is made of polyester terephthalate (PET), chosen because of its insensitivity to humidity. Lucite brackets, fit into the top and bottom of the frame, support the quartz plate and provide a coupling to the face of the PMTs. An optical grease compound between the lucite and PMT surfaces helps guarantee that the optical coupling is good. A schematic of the system can be seen in Figure 2-6. The frame also holds two light emitting diodes (LEDs), one pointed at each PMT, which allow monitoring of the PMTs and testing when beam is absent. The entire assembly of frame, PMTs, and bases for Mitch are encased in a light-tight housing

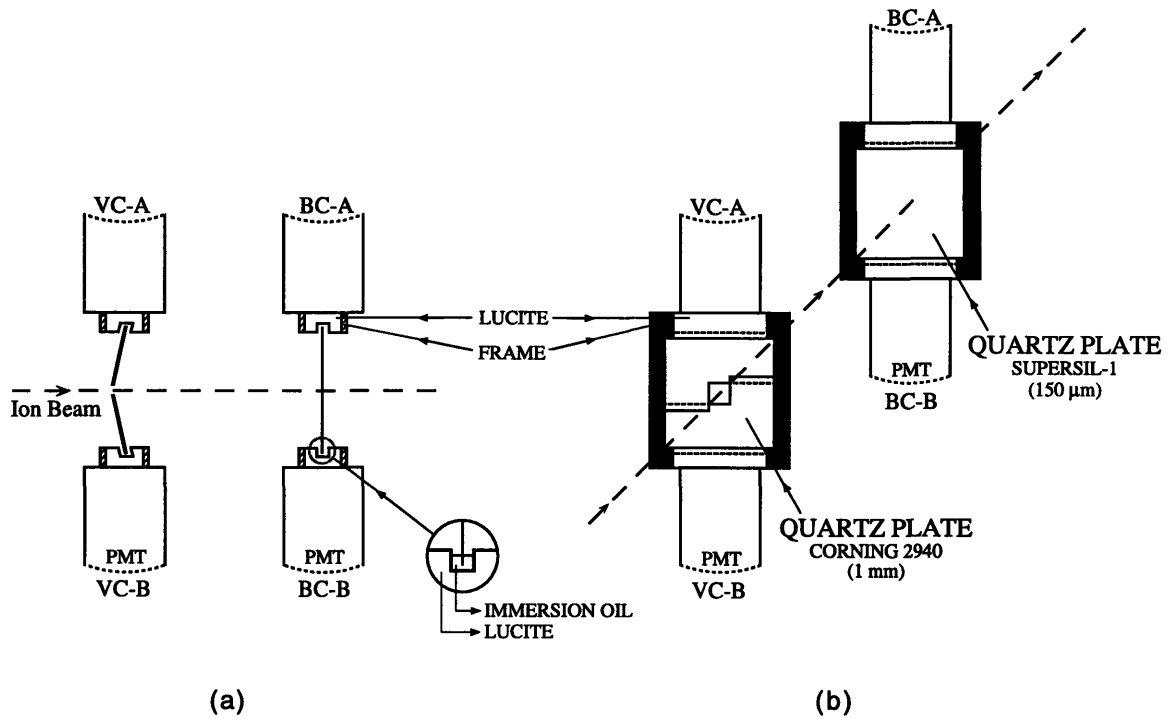

Figure 2-6: The optical assembly of the quartz beam (BC, or Mitch) and hole veto (VC) counters. Side and perspective views are shown.

along with those for the Čerenkov beam hole veto counter as shown in Figure 2-5.

To avoid stresses on the fragile quartz plate, and to insure good optical contact between the plate and the lucite bracket, the quartz plate is suspended in an immersion oil whose index of refraction is very close to that of the quartz and lucite ($\sim$1.5). The oil fills a slit in the lucite which is slightly wider than the quartz plate. Because of capillary action, the oil stays in the slit without dripping or running regardless of its orientation. Care is taken to make sure no air bubbles are left in the immersion oil.

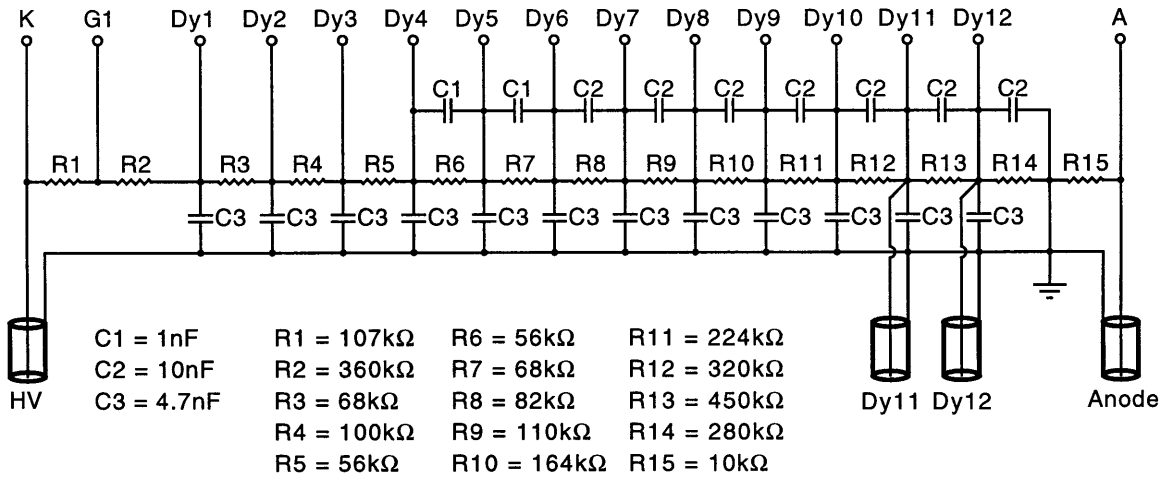

Figure 2-7: The MIT designed and built PMT base for the Mitch beam trigger counters. Small capacitors provide high frequency noise filtering, and connections to the eleventh and twelfth dynodes allow booster current supplies to prevent dynode voltages from sagging.

Electrical Components

The PMTs for the beam counter were selected for their fast rise times (1.4 ns at a recommended 2500 V) and reasonably high anode current limit within a set cost. Despite the high current limit, it turns out that the anode current drawn at the recommended voltage at the intended 10^7 Hz beam rate of E864 would still be excessive. The PMTs have been found to operate well enough at a reduced main voltage of $\sim$1600 V with a custom designed PMT base as shown in Figure 2-7.

Additional care has to be taken to avoid voltage sagging in the last couple dynodes of the PMT. With the high pulse rates, a significant amount of current is pulled from the last dynodes into the electron cascades. Because the voltages of the dynodes are set by a simple bleeder resistor chain, the decrease in current flowing through the last few resistors changes the potential drop across them. This introduces an instability in the gain characteristics of the PMT, which are highly sensitive to the dynode voltages. By introducing current supplies to the last two dynodes (where the most current for the electron cascade is required), the resistors are able maintain the

desired voltage drops regardless of the beam rate.

Pre-trigger electronics sum the signals from the two PMTs into a $\sum_{Mitch}$ signal, which is then split for its many functions. A typical single Au ion produces an 80 mV $\sum_{Mitch}$ signal. A low threshold (10 mV) discriminator fires on the leading edge of the pulse for a gate start signal.[2]

Other copies of $\sum_{Mitch}$ are discriminated just below and just above 80 mV to create a *pulse height window* around the single Au ion pulse height. This prevents anything other than a single Au ion from starting the gate.

Another $\sum_{Mitch}$ pulse is used to create a *pulse time window.* This causes the gate to be vetoed if any other Mitch pulses come within a specified time before or after the one being examined.

The actual time for the passage of the Au beam particle through Mitch is not taken from $\sum_{Mitch}$ in the analysis. Instead, each PMT's signal is also run through a low threshold discriminator for precise timing, and the mean time of the two is used as the time zero.

Radiation Damage

Despite the precautions taken to avoid radiation damage, it became apparent during the 1995 run of the experiment that indeed the beam trigger counter was incurring some sort of beam-related damage. A thin film of material had developed on the surface of the quartz plate in the region where the beam passed. The material diminished the internal reflection of Čerenkov light in this region, degrading the performance of the counter's pulse height and time resolutions. The film was later found to contain carbon and oxygen compounds through spectroscopic analysis. However, the mechanism of the film's manifestation has not been determined.

For the second half of the 1995 run, nitrogen was flowed through the Mitch housing in an effort to reduce the radiation damage, targeting the likelihood that the carbon

[2]Because $\sum_{Mitch}$ is a sum of two pulses, the earlier of the two pulses actually sets the timing of the gate. Some disparity was seen in the 1995 data between time of flight measurements obtained when different Mitch PMTs set the gate, so one PMT's signal was specifically set approximately one nanosecond earlier in 1996 to make sure it always set the gate.

and hydrogen in the films were drawn from the air surrounding the quartz plate. Additionally, a 1 mm quartz plate was substituted which required fewer internal light reflections and was therefore less sensitive to any manifestation of surface films. While the nitrogen may have helped, some film was found to have formed on the quartz by the end of this period also.

A redesign of the frame was made for the 1996 run to allow the quartz plate to reside in vacuum. The 1 mm quartz plate from the 1995 run demonstrated that thicker plates reduced the sharpness of the light pulse emanating from the plate, thus reducing timing precision. A plate thickness of $\sim$300 μm was chosen as a compromise, and for the additional strength needed to handle any air pressure gradients associated with changes in the vacuum. The quartz plate used in the 1996 experiment run was a 4.57 cm $\times$ 7.98 cm $\times$ 305 μm piece of DYNASIL 1107 (believed to be equivalent in performance to the Supersil, but easier to obtain).

The quartz plate has remained inside the vacuum-tight frame since the 1996 run to keep it well protected before the 1998 run of E864, so the plate has not been visibly examined. However, no deterioration of the beam trigger counter signals was seen during the 1996 run which could be attributed to damage to the quartz plate.[3] Additionally, data taken during the 1998 run gave no indication of damage to the plate.

Performance

The design goal for the Mitch beam counter was 100 ps time resolution at a Au ion beam rate of 10^7 Hz. However, to avoid the radiation damage which had been seen the previous year, the beam rate was reduced for the 1996 runs to an average rate of approximately 2×10^6 Hz (the interaction rate was kept high by using a target of greater interaction length). At this rate, Mitch achieved a time resolution of $\sim$40 ps.

Two runs were conducted at the end of the data collecting, and after an integrated

[3]There was a loss of signal from one of the two PMTs during the run, but this was attributed to either the PMT itself or its base. The problem was corrected when both the PMT and its base were replaced.

exposure of 5×10^{12} Au ions, to determine if there had been any significant radiation damage. The first run was taken at the standard rate of 2×10^6 Hz and showed a time resolution of 42 ps. Because the beam rate fluctuates significantly about the average, it is important that the resolution is similar at higher rates. So the second run was taken at a rate of close to 10^7 Hz. The determined resolution of 53 ps for this run is still much better than the design goal.

Pulse height resolution was also very good. Double-beam rejection was performed easily enough in off-line analysis for any double-beam events not caught by the pre-trigger logic of the experiment.

2.2.2 Beam Hole Veto Counter (VC)

The VC counter is located immediately upstream of Mitch inside the Mitch housing. Its primary function is to veto beam particles which are not close to the beam axis, and therefore not well centered on the target. The design of VC is similar to Mitch in many ways, but is not constrained by the need for precision timing nor good pulse height characteristics. Additionally, since the majority of the beam is meant to pass through the hole, beam rate is not a significant issue.

Optical Components

Like Mitch, VC uses Čerenkov light produced in quartz mounted inside a PET frame to detect beam particles. Unlike Mitch, VC uses two L-shaped quartz plates tilted at a 10° angle to the beam as seen in Figure 2-6. The two-piece construction makes it easy to design a 1 cm $\times$ 1 cm hole without the difficulty of attempting to machine a hole in the center of one fragile piece of quartz. As each quartz plate is viewed by only one PMT, the plates need not be set perpendicular to the beam. By tilting the plates as shown the Čerenkov light collection efficiency is improved.

The quartz plates themselves are 1 mm thick Corning 2940, which is cheaper and easier to machine without breaking. Each plate is held fixed in the slit of its lucite bracket with an optical cement. Two LEDs are also mounted on VC for similar

purposes as on Mitch.

Because the percentage of beam passing through the quartz plates is small, radiation damage in the quartz plates for VC is negligible. So there is no need to place the quartz plates in vacuum.

Electrical Components

Bases identical to those for Mitch are used in VC. With the lower firing rates, no booster current supplies are necessary for the last dynodes.

The output pulses from both PMTs are summed in the pre-trigger logic. If any pulse significantly above noise is seen, a veto signal prevents any Mitch triggers within a small time window from being registered.

2.2.3 Secondary Beam Trigger Counter (MIC)

A second beam trigger counter, MIC, was tested in 1995 and installed for the 1996 run. It is meant as a backup for and possible improvement over Mitch for some of the tasks Mitch performs. Because space is limited in the front-end of the experiment, MIC is placed about 1.5 m upstream of Mitch along the beamline.

Optical Components

MIC's optical construction is also similar to that of Mitch, with a PET frame supporting a single quartz plate. Since its location is upstream of lead shielding which constricts particles coming down the beamline to an area just a few cm in diameter, the MIC quartz plate is larger, at 7.00 cm $\times$ 13.82 cm. The same 305 μm thick DYNASIL 1107 quartz is used.

This location also requires that MIC's light-tight housing has to be integrated into the beam pipe so that the beam remains in vacuum as long as possible, while passing through as few vacuum windows as possible. The advantage of this approach is that MIC does not need its own vacuum; it sits in the vacuum of the upstream beam pipe. Figure 2-8 details the major points of MIC's construction.

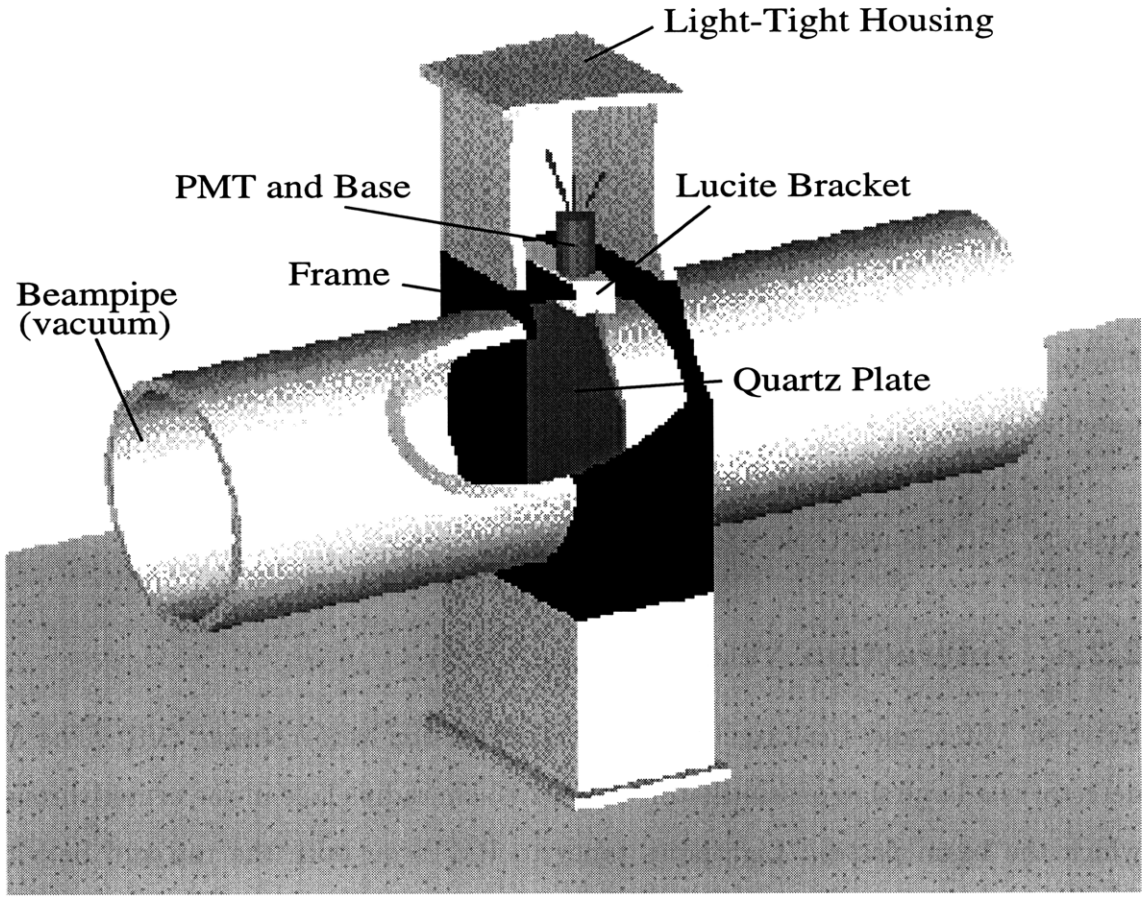

Figure 2-8: A cut-away view of the MIC counter showing the layout of the major components. The MIC counter is designed to be integrated with the upstream beampipe.

An LED is mounted opposite each PMT inside the MIC frame for monitoring and testing.

Electrical Components

MIC's PMTs are specially fabricated Hamamatsu R5600s, which are known to have especially sharp rise times ($\sim$0.5 ns). However, with a photocathode face less than 1 cm in diameter, their integrated light collection is poor at such a distance from the beam. This degrades the pulse height resolution of the counter and may also

degrade the time resolution through uncorrected slewing effects. It may also help the time resolution by limiting the geometrical acceptance to that Čerenkov light which is produced within a small cone of solid angle, which would intrinsically be less spread out in time.

Performance

MIC attained a time resolution of ~32 ps during the typical 2×10^6 Hz beam rate running. By the end of the 1996-1997 run, the time resolution was 35 ps for MIC. During the 10^7 high-rate run taken at the end of the data collection, MIC's resolution remained close to 40 ps.

Pulse height resolution for MIC was not as sharp as it was for Mitch. In this analysis, Mitch is used solely for the beam trigger counter.

2.2.4 Interaction Veto Counter (VS)

Between Mitch and the target stands the interaction veto counter (VS). The VS detector is a large slab of scintillator with a 2.75 cm radius hole in the center through which the beam passes. Lightpipes taper to PMTs on both the top and bottom. Its purpose is to detect secondary particles resulting from upstream interactions, providing a veto on any such interactions. To prevent VS from triggering on knock-on electrons (δ-rays) produced by good beam particles traversing vacuum windows and beam trigger counters, a significant amount of lead shielding is placed upstream of VS. Additional lead shielding is placed between VS and the target to prevent target back-scattering from passing through the scintillator.

2.2.5 Multiplicity Detector (MULT)

A segmented multiplicity detector is located 13 cm downstream of the target as shown in Figure 2-5. A view of MULT from along the beamline is shown in Figure 2-9. This detector is used as a gauge of the total multiplicity of the heavy ion collisions. Because the total multiplicity is correlated to the centrality of the collision, the counter is also

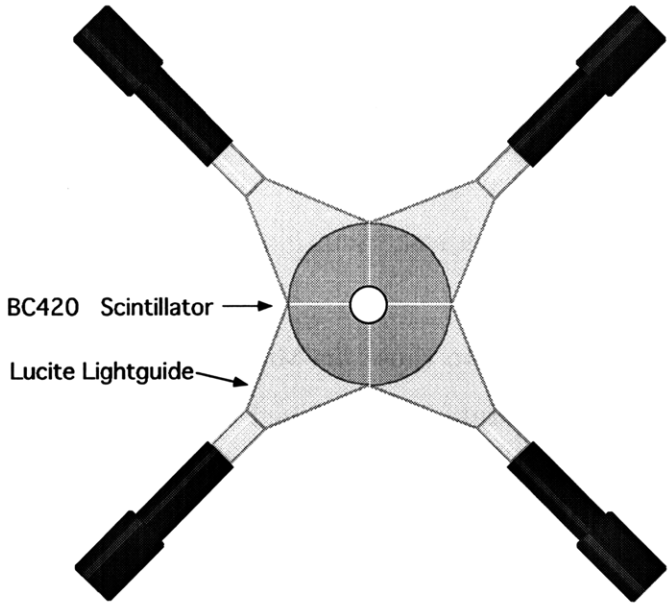

Figure 2-9: The segmented MULT detector as viewed by the beam.

intended as a measurement of centrality, or impact parameter.

Components

MULT is constructed of four circular quadrant-shaped pieces of 1 cm thick fast BC420 scintillator. Each quadrant is tilted 8° from the plane normal to the beam axis to better face the target, and covers an angular range between 16.6° and 45.0° from the target (pseudo rapidity $\eta = 1.92$ to 2.44). One PMT views the light from each quadrant through a tapered lightguide.

Before the experiment began, studies were performed with cosmic rays and a ^{90}Sr source to see whether permitting reflections inside the scintillator and light pipe yielded better performance than not. Because the amount of light produced by the scattered particles passing through the scintillator pads is known to be abundant, light losses through reduced surface reflectivity can be afforded. A black paint was used to coat various surfaces on the scintillator and light pipe for the tests. It was found that the time resolutions and insensitivity of the pulse heights and rise times to the locations of the passing particles in the scintillator are optimal when the entire surface was made unreflective. All surfaces of the scintillator and light pipe are painted black and then covered in light-tight wrappings for the experiment.

A Monte Carlo performed before the experiment also showed that a significant amount of energy (a few hundred MeV, depending on the target) would be deposited it the MULT scintillators from δ-ray production at the target. To limit this effect, a 6 cm thick ring of Heavymet[4] shields the scintillators from the target, as seen in Figure 2-5.

The PMTs and bases are similar to those for Mitch and VC. No booster current supplies are needed since the pulse rate is determined by the number of interactions, not the beam rate itself.

Interaction Trigger

By adding the four signals from the individual MULT PMTs, a $\sum_{MULT}$ signal is found which should be directly related to the total multiplicity of the collision. Discrimination is set to various pulse heights to be used as trigger criteria. A low threshold discriminator set to fire on anything above background noise provides a minimum bias trigger criterion. This INT0 trigger is our minbias trigger.

A second discriminator is set to fire for half of the pulses which fire the INT0 discriminator. This upper 50% criterion is for the INT1 trigger. A third discriminator fires on only the top 10% highest pulses for the INT2 trigger. For all three of these triggers, there is an additional criterion that all four individual MULT PMTs registered a signal above noise. This last item helps prevent upstream interactions from contributing to these triggers. These criteria are used to select whether or not to allow the experiment gate to be active, but the timing of the gate is still set by Mitch.

A histogram of MULT pulse sizes as measured through an ADC is shown in Figure 2-10. A second histogram of pulse sizes for INT2 triggers is overlaid (dashed line). Because pulse sizes are not evenly distributed among all collisions, the 10% largest pulses actually correspond to the upper $\sim$60% of the pulse sizes.

Monte Carlo studies were also performed to study the relationship between MULT

[4]Heavymet is a 95% tungsten, 3.5% nickel, and 1.5% copper alloy with a density of 18.5 g/cm^2.

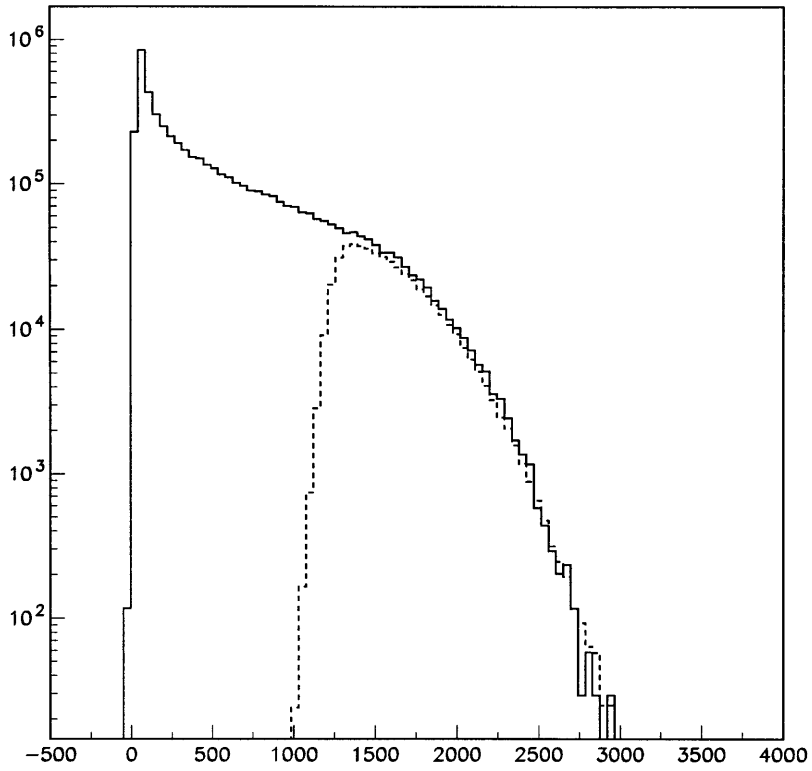

Figure 2-10: MULT ADC distribution for INT0 triggers (solid line) and INT2 triggers (dashed line).

signals, multiplicity, and centrality. The Monte Carlo was conducted with an 11.71 GeV/c per nucleon Au beam incident upon 10% of an interaction length of Pb used as the target. A total of 17,500 collisions were simulated in HIJET, and then run through GEANT with all physics processes turned on. GEANT's simulation produced the number of photoelectrons expected in the MULT PMTs after considering the energy deposited in the scintillator, the emission spectrum for the scintillator, the physical geometry of the scintillator and lightguide, and the spectral response of the PMT's photocathode.

A comparison of Monte Carlo data and experimental MULT data is shown in which lead to the 10% highest ADC values is shown in Figure 2-11. The experimental data

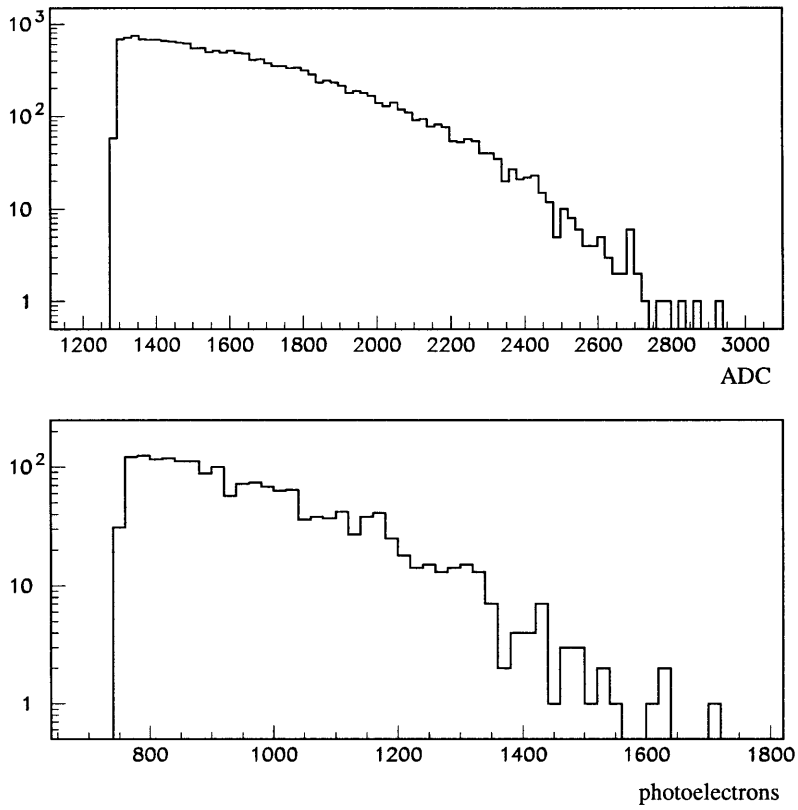

Figure 2-11: A comparision between experimental data ADC values for those events with the 10% highest ADC values from a minbias sample of events, and Monte Carlo events with the 10% most photoelectrons respectively.

shows the ADC spectrum of MULT for the 10% highest ADC values. The Monte Carlo data shows the 10% highest photoelectron yields. The spectra appear to match very well.

The Monte Carlo also permitted impact parameter studies. Figure 2-12, part a) shows histograms of impact parameter distributions for those events with the 10%, 5%, and 1% most energies deposited in the MULT scintillators. Shown in part b) of Figure 2-12 are the probabilities that a given impact parameter will pass a cut which selects those events with the 10%, 5%, and 1% most energies. In both histograms, the solid line corresponds to 10%, the dashed line to 5%, and the dotted line to 1%.

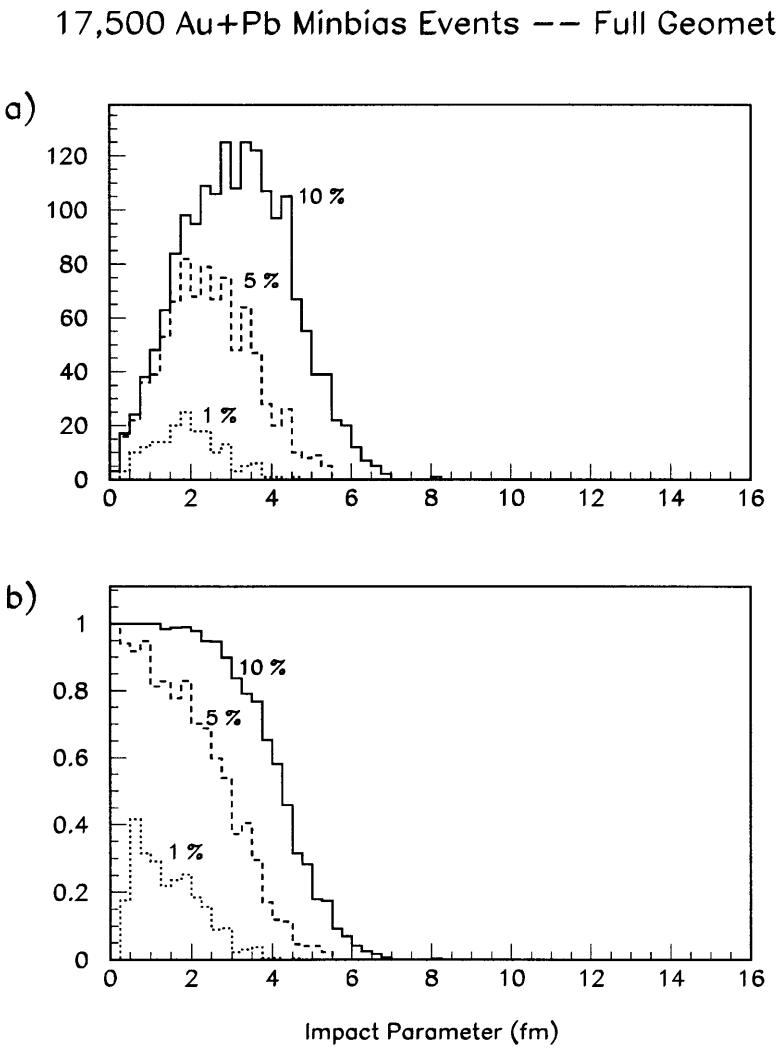

Figure 2-12: Monte Carlo impact parameter studies. See text.

The relationship between centrality and energy deposited in MULT is complicated by several issues. These include the non-linear relationship between centrality and multiplicity, event by event fluctuations in multiplicity, and the fact that MULT does not actually measure the total multiplicity (its solid angle coverage is not 4π). However, it is clear that placing cuts on the MULT spectrum does in fact constrain the impact parameter. The Monte Carlo shows that 88% of those events selected for the 10% most photoelectrons (largest pulse sizes) are in fact among the events with the 10% smallest impact parameters.

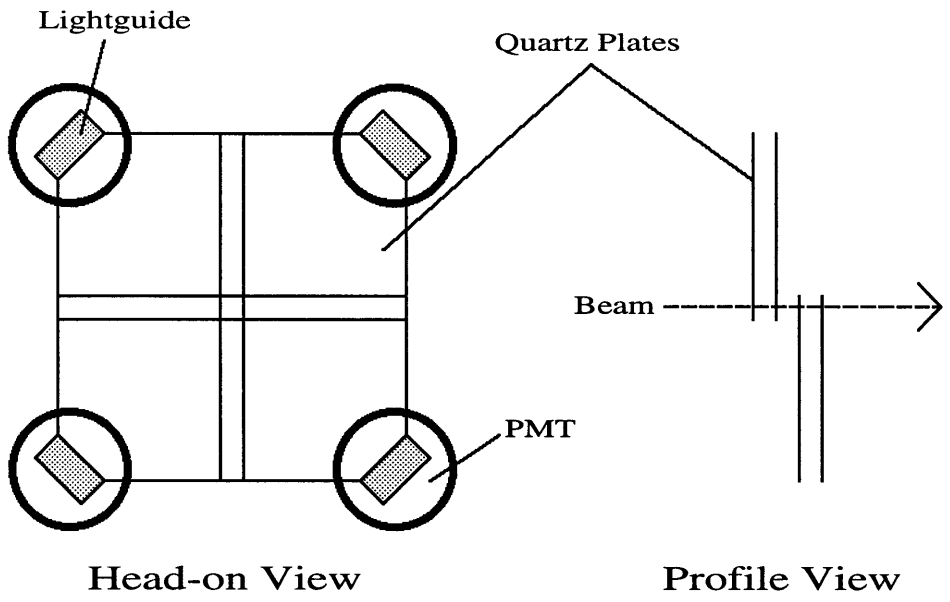

Figure 2-13: The MAC detector.

2.2.6 End Counter (MAC)

At the downstream end of the experiment there is another Čerenkov beam counter. It sits in a cavity within the beam dump beyond the calorimeter and last vacuum window. This counter, called MAC (for Massachusetts Čerenkov counter), is segmented into four overlapping quadrants, as seen in Figure 2-13.

Components

Each quadrant is a 10 cm $\times$ 10 cm piece of 1 mm quartz viewed by its own PMT. The quadrants are aligned with their edges horizontal and vertical. Overlap between quadrants is 1 cm, creating a 1 cm square area in the middle which is viewed by all four quartz plates.

A lightguide with a 90° bend (via a 45° beveled corner) brings a portion of the Čerenkov light for the quartz plates into their PMTs. Because good pulse char-

acteristics are not critical, significant losses from light exiting other edges are not important.

MAC is equipped with LEDs, one mounted next to its lightguide on each PMT. The same MIT-designed PMTs and bases from Mitch are used since MAC is also an in-beam counter. The last two dynodes of each PMT are current supplied just as well.

The entire assembly of quartz plates and PMTs is housed in a light-tight box with a thin stainless steel window at the front where the beam enters. This box sits on rails the allow MAC to move in the x direction. This permits MAC to be aligned with the beam under different magnetic field settings.

Functionality

The geometry of MAC makes it extremely helpful for beam tuning. It is important that the beam is not only centered on the target, but that it is straight (its momentum lies solely in the z direction).

Four SWICs (segmented wire ion chambers) upstream of the experiment provide both horizontal and vertical beam profiles allowing for beam tuning up to the target. With the spectrometer magnets off, and MAC positioned such that its center is in line with the z axis, the beam can also be centered horizontally and vertically on the four MAC quadrants, insuring a straight trajectory through the experiment.

With the beam tuned, MAC was also used during by E864 to calibrate the current settings for the spectrometer magnets to reach desired fields. A particular field in the magnets corresponds to a particular x position at MAC to which the beam will bend. With MAC set to these positions, the magnets were adjusted to center the beam on MAC.

MAC is additionally capable of providing a profile of the beam along the x axis. This is done by requiring the beam particles to pass through horizontally overlapping sections, and plotting the rate (divided by the rate seen in Mitch for a given spill) as a function of x while sweeping MAC's position across the beam. Such a profile is shown in Figure 2-14 and demonstrates the spatial resolving power of the system.

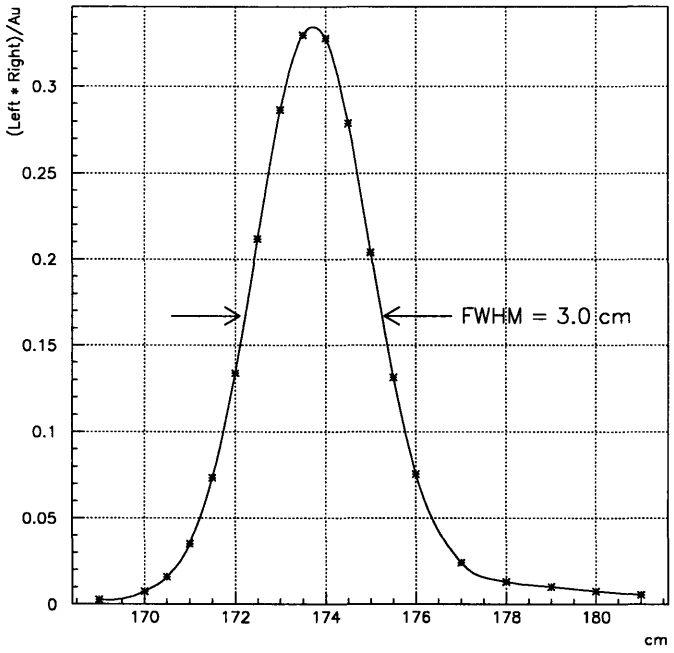

Figure 2-14: Horizontal profile of the beam as seen by a scan of MAC positions across the beam trajectory. The vertical axis is the number of counts per spill from beam particles going through the horizontal center of MAC, divided by the number of Au ions counted in Mitch. MAC Left is defined as the logical OR of signals seen in the two beam left quadrants of MAC, and MAC Right is the logical OR of the two on beam right. The logical AND of Left and Right implies that the beam particles passed through the overlap of the left and right halves of MAC, describing a 1 cm wide vertical slat defined as the horizontal center. The profile seen is thus a convolution of the actual beam profile and a 1 cm wide square function.

Because MAC detects non-interacting Au beam particles, it can be used in event selections to allow for double-beam events in which the second beam particle did not interact. This feature is not necessary in the 1996-1997 data set because of sufficient multiple-beam rejection in the pre-trigger electronics, but was used in part of the 1995 data analysis.

Lastly, MAC was used in analysis of the 1995 data as a method of subtracting the gate when trying to calibrate Mitch. MIC was able to better serve this purpose in the 1996-1997 data set.[5]

[5]See section 3.1 for details on Mitch calibrations.

2.3 Hodoscopes

The scintillator hodoscopes provide time, position, and charge magnitude information on charged particles which traverse the spectrometer. These are the fundamental characteristics necessary for particle identification with a spectrometer. As such they are vital to the experiment.

Table 2.3 provides the physical specifications for the scintillator slats. Each scintillator slat is wrapped loosely in aluminized mylar to allow for total internal reflection at scintillator-air interfaces while preventing optical cross-talk between slats. Light-tightness is achieved for the entire planes with additional layers of aluminized mylar.

Plane	Number of Slats	Width (cm)	Height (cm)	Depth (cm)	Material
H1	206	1.105	63.6	1.0	BC404
H2	206	1.506	81.3	1.0	BC404
H3	206	2.306	106.4	1.0	BC404

Table 2.3: Hodoscope scintillator slat physical specifications.

At the upper and lower ends of each slat is a lightguide which bends through 90° into a PMT. Slats are alternated between bending forwards and backwards as shown in Figure 2-15. The vertical offset of the slats with respect to their frame is also staggered. This configuration is necessary for two reasons. The bend prevents the PMTs and their bases from extending upwards, allowing placement of the hodoscopes relatively close to the vacuum chamber within the limited vertical space. The PMT and base arrangements are much wider than the slats themselves, necessitating the directional alternation and vertical stagger.

Cockroft-Walton bases are used to power the PMTs. These transform a low voltage input to the high voltage necessary for the PMTs. They also split the anode signal internally and include on-board discrimination of one of the two signals for timing information. This improves timing resolution by discriminating on the signal pulses before any deterioration of the analog signal caused by noise and attenuation in the long cables between the hodoscopes and the data acquisition system.

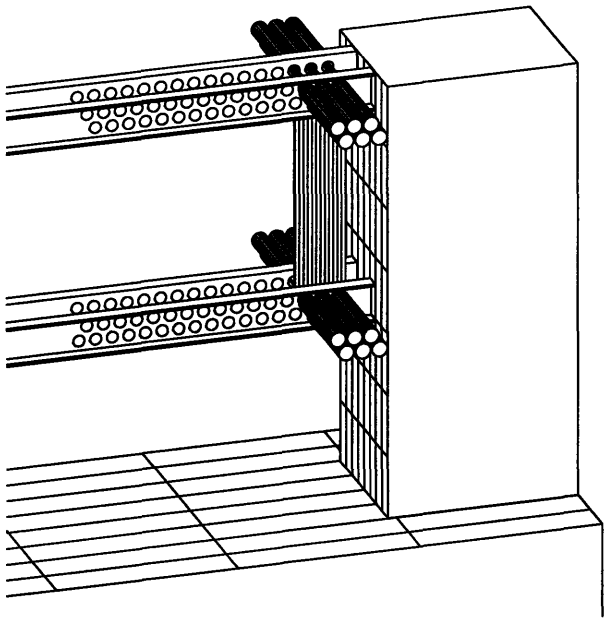

Figure 2-15: Construction of the hodoscope scintillator planes. Slats are arranged with their PMTs and bases pointing alternately forwards and backwards, and are staggered in vertical offset to allow for tight packing.

Charge information comes from the fact that a scintillator's light production is proportional to the square of the charge for a minimum ionizing particle. The mean time between the signals measured at the top and bottom of the hodoscope slat provide timing information for tracks, while the time difference of the two relates to the y position of the track. The x and z positions of the hodoscope slats themselves provide additional positional information.

2.4 Straw Chambers

The straw wire chambers serve solely to provide precision positional measurements of tracks. The hodoscopes yield adequate information for determining whether a track exists, but good resolution in rigidity reconstruction requires better knowledge of the track vector. The straws make this possible through high granularity. Each straw tube is cylindrical with dimensions as shown in Table 2.4. With the straws, mass resolution is reduced to less than 6% for all particle species.

Plane	Number of Straws	Straw Radius (cm)	Straw Length (cm)	Angle to Vertical
S2X	960	0.2	48.55	0.0°
S2U	960	0.2	48.55	+20.0°
S2V	960	0.2	48.55	-20.0°
S3X	1920	0.2	90.20	0.0°
S3U	1920	0.2	90.20	+20.0°
S3V	1920	0.2	90.20	-20.0°

Table 2.4: Straw chamber physical specifications. Positive angles to the vertical mean the straw tube goes from small x to large x from bottom to top.

S2 and S3

In all, there are six utilized planes of straws in two stations, S2 and S3. Each station has three planes at various angles to the vertical. S2 has a fiducial area of 40 cm $\times$ 200 cm, and S3 80 cm $\times$ 400 cm. The straws in an individual plane are staggered such that odd-numbered straws are adjacent in one plane, and the even-numbered straws are offset to lie in the groves between the odd-numbered straws as in the lower schematic of Figure 2-16. An additional layer of empty straw tubes was added to both sides of each plane in S3 to support the planes and help prevent bending.

The individual straw tubes are made of two layers of mylar. The inner layer is aluminized to serve as the cathode. The wires inside are gold tungsten with a diameter of 25 μm and are held with 50 gm of tension in S2, 70 gm in S3. Gold-plated crimp pins hold the straws at either end and allow good electrical contact. The wires are held at -1250V during the experiment, with the aluminized tubes at ground. A gas mixture of $Ar/CO_2/CH_4$ in the proportions 90:9:1 flows continuously through each tube as a dielectric.

Humidity fluctuations in the experimental area were a concern during the run as they affected bowing in the tubes. The bowing led to frequent sparking as the anode wires saw asymmetric fields and in turn bowed closer to the aluminized tubes. The humidity ranged from 16%-80% before humidifiers and dehumidifiers were placed next the the stations to maintain near 50% humidity.

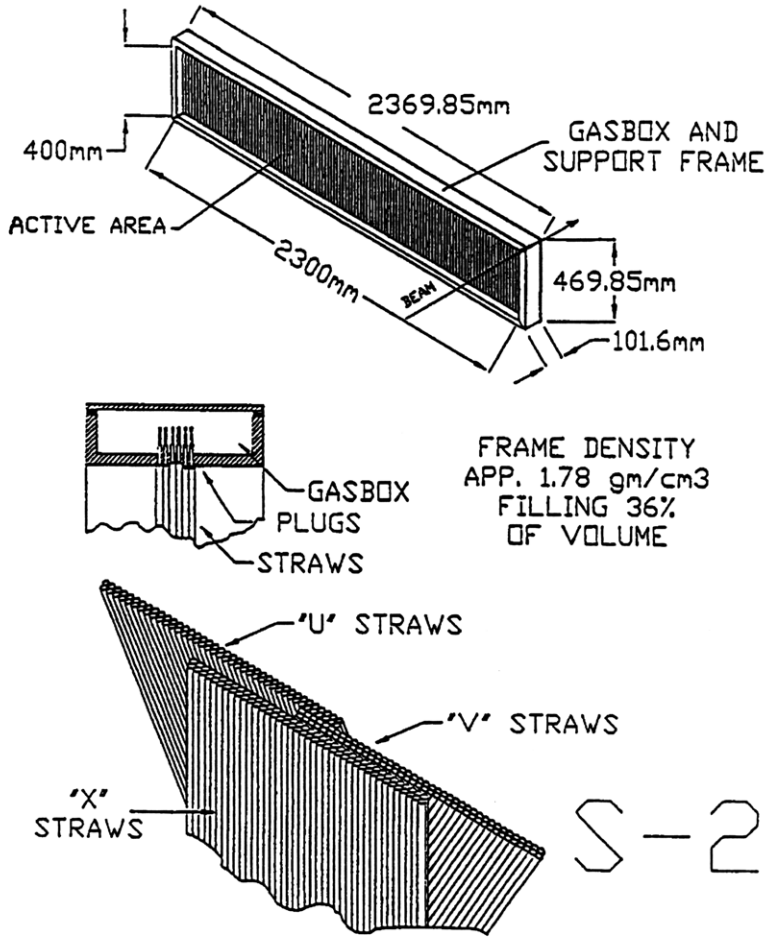

Figure 2-16: Construction schematics of the S2 straw tracking chamber.

The straw outputs are simply hit-or-miss electrical signals. These are amplified and read out with a Lecroy PCOS IV CAMAC system for data acquisition.

S1

The spectrometer includes a third station of straw planes, S1. This station is located between the two dipole magnets M1 and M2 inside the vacuum chamber. S1 was intended to be used for rejection of tracks which did not originate from the target. However, S1 was susceptible to sparking and significant noise. It therefore did not

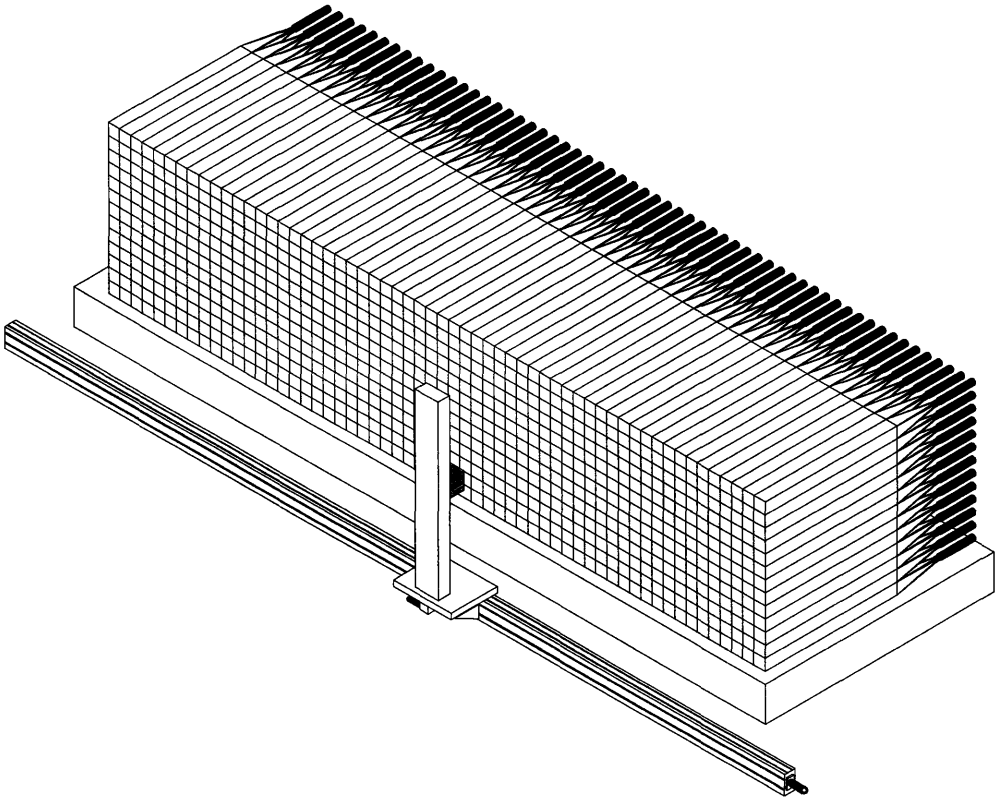

Figure 2-17: Perspective view of the E864 calorimeter and ^{60}Co calibration source mobile platform. Towers are stacked in an array of 58 columns and 13 rows with no gaps between them. Each tower is read out with a single PMT at the back.

provide meaningful information for track rejection and was not used for E864 data analyses. Unfortunately, S1 was left in place during the 1996-1997 run and the materials of the frame and housing of S1 did contribute to the scattering background of the experiment.

2.5 Calorimeter

Particles which traverse the spectrometer are eventually stopped in the calorimeter. The E864 calorimeter is a spaghetti design [23], which uses scintillating optical fibers embedded longitudinally in a high Z absorber material. Hadrons which stop in the

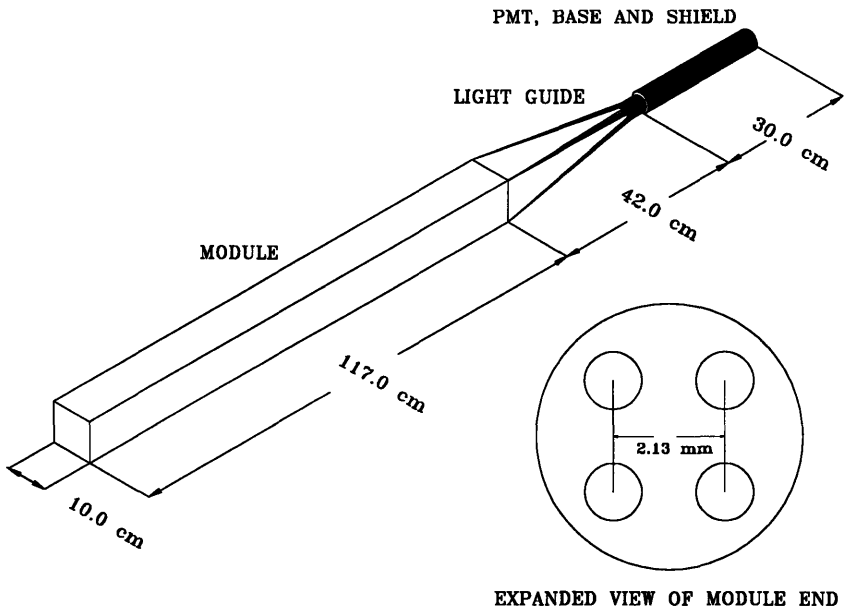

Figure 2-18: An individual calorimeter tower module with light guide and PMT attached to the back.

absorber deposit energy into a shower of charged particles. As these particles pass through the scintillating fibers, light is produced which may then travel down the fiber to a PMT. The collected light is in turn a good measure of the energy in the shower.

The E864 calorimeter uses Pb as the high Z absorber[6], and BCF-12 for the scintillator. The average tower density is 9.6 g/cm^2, resulting in a nuclear interaction length of 19.7 cm, and an effective radiation length of 0.78 cm [24].

The calorimeter is segmented into 754 towers, each of which is 10 cm $\times$ 10 cm $\times$ 117 cm. They are arranged in a 58 $\times$ 13 array as shown in Figure 2-17. Individual tower modules are constructed as shown in Figures 2-18 and 2-19. Each tower has a 47 $\times$ 47 array of evenly spaced fibers, each of radius 0.055 cm. The front faces of the towers is covered with a black, light-absorbing eopxy to prevent reflections in the fibers. Light that travels to the back end of the fibers is collected in tapered

[6]The absorber of the E864 calorimeter is actually 99% Pb and 1% antimony, which hardens the Pb to a desirable mechanical strength, but has negligible effect on the absorption.

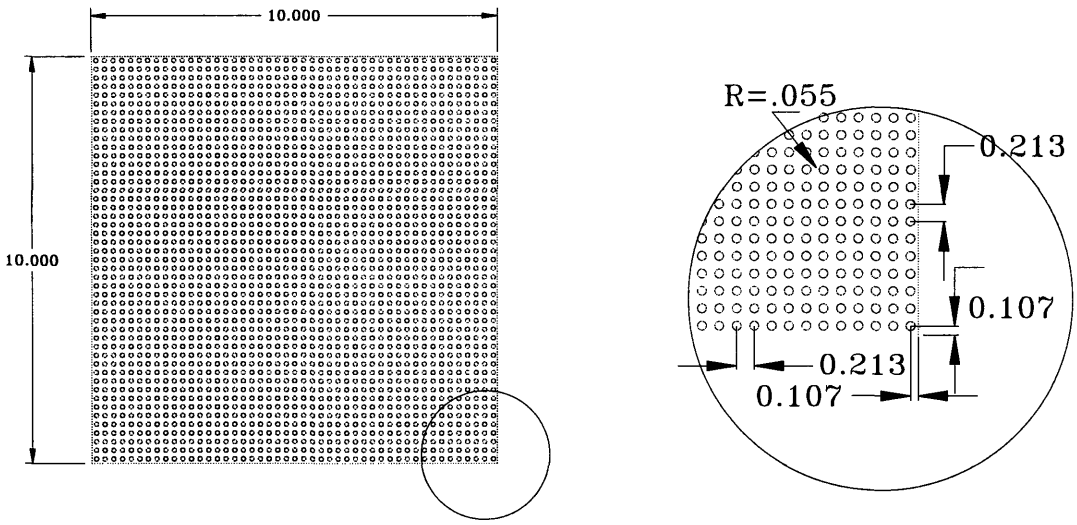

Figure 2-19: Cross sectional view of an individual calorimeter tower module. An array of 47 × 47 scintillating fibers is embedded in a 10 cm × 10 cm Pb matrix with a spacing of 0.213 cm between fiber centers. The insert shows the position and dimension of the fibers. All dimensions are in cm.

lightguides which are optically epoxied to the backs of the towers. Philips XP2262B PMTs are mechanically held against the lightguides for readout. The PMT bases (Nanometrics N407) have the same Cockroft-Walton style configuration as for the hodoscopes (see Section 2.3).

A ^{60}Co calibration system has been designed which rests on a mobile platform that can be positioned in front of any of the 754 towers. This allows frequent gain matching of the towers which is important for calibrating the energy response of the calorimeter towers. Such calibrations will be discussed later in Section 3.4.5.

Hadronic showers tend to spread out over several towers in the calorimeter. Figure 2-20 shows the shower profile as a function of distance from the shower center. Therefore, to find the energy contained in a single shower, the output of several towers must be summed to reconstruct the energy. A typical hadronic shower will contain only the kinetic energy of the incident hadron. However, incident antimatter will

annihilate inside the calorimeter, adding an additional amount of energy equivalent to twice its mass to the shower. Thus, for particles striking the calorimeter, a mass (M) can be determined.

$$M = \frac{E_{\text{calorimeter}}}{\gamma \pm 1} \tag{2.7}$$

The +/- sign is for antimatter/matter respectively. γ can be determined from the time of flight to the calorimeter, or from tracking in the hodoscopes in the case of charged particles. The energy resolution for hadronic showers is found to be $\delta E/E \approx 40\%/\sqrt{E}$, and the time resolution is $\sigma_t \approx 400$ ps.

2.6 Late Energy Trigger (LET)

In order to obtain the sensitivities needed to see rare particle production E864 requires a very selective trigger. The Interaction Trigger (INT0, INT1, or INT2 as described in Section 2.2.5) provides a good Level-1 trigger for selecting events in which there was some type of collision in the target. However, a Level-2 trigger is necessary to weed out uninteresting interactions. For this purpose, a Late Energy Trigger system [25] has been implemented in E864.

The LET uses signals from the calorimeter as a basis for triggering on slow, yet energetic particles. The calorimeter signals are quickly digitized using fast logic during an event triggered on an interaction using the MULT counter. In the case of this particular analysis, INT2 triggers are used since strangelets are expected to be produced in central collisions where the baryon densities are high during the collisions, and outgoing particle multiplicities are expected to be large.

Recall from Equation 2.7 that a mass can be determined from the energy and speed (in the form of γ) of a particle which strikes the calorimeter. Because the ADC value for a given tower is proportional to the energy collected in that tower, and because the timing of the signal from a tower is related to the speed of the particle whose shower is observed by that tower, a trigger based on these ADC and timing

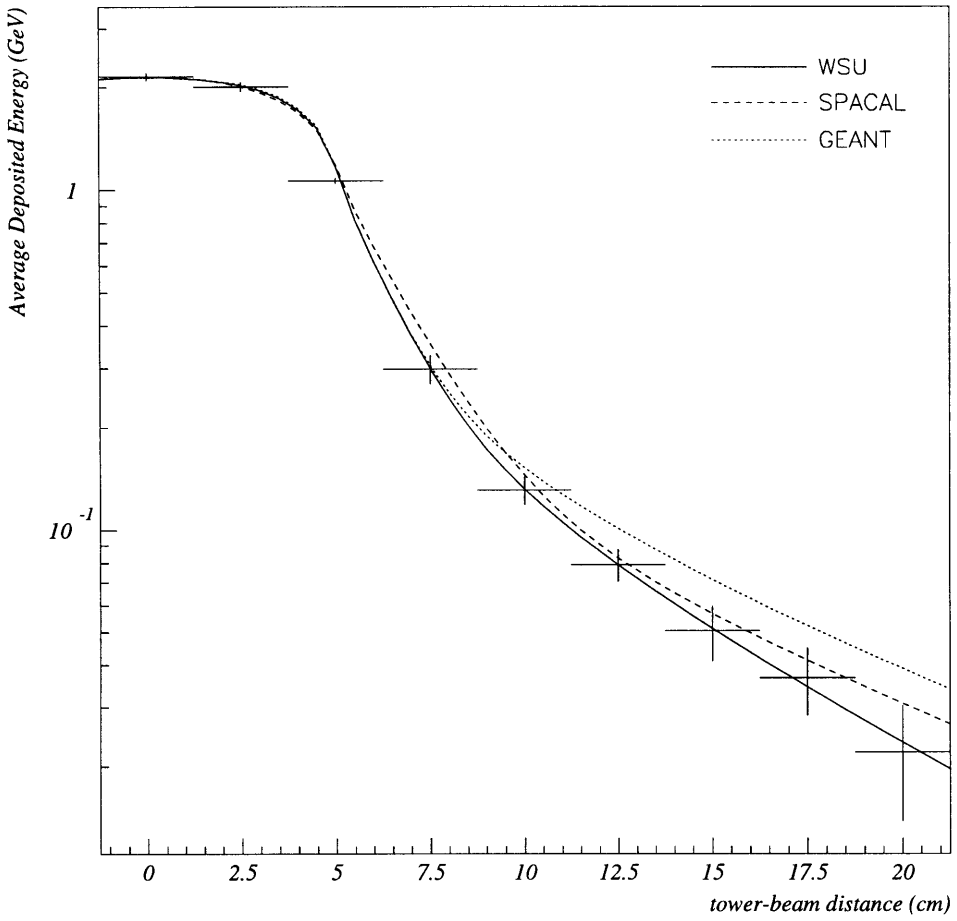

Figure 2-20: Profile of calorimeter showers using energy deposited as a function of distance from shower center as defined by the location of a test beam. SPACAL measurements and GEANT simulations are overlayed on data collected and fit by Wayne State University (WSU) which built the E864 calorimeter.

values can selectively choose events with high mass candidates. A diagram of how this is architectured in hardware is shown in Figure 2-21. Fast ADCs (FADCs) digitize the output of an analog signal integrator for the energy, and the output of a time to amplitude converter (TAC) from the discriminated pulse for the timing.

For each tower, the LET uses the ADC and timing values as coordinates in a Lookup Table (LUT). The LUT thus describes a phase space like that of Figure 2-22. In this diagram, one can see that a particular mass describes a curve in the energy and

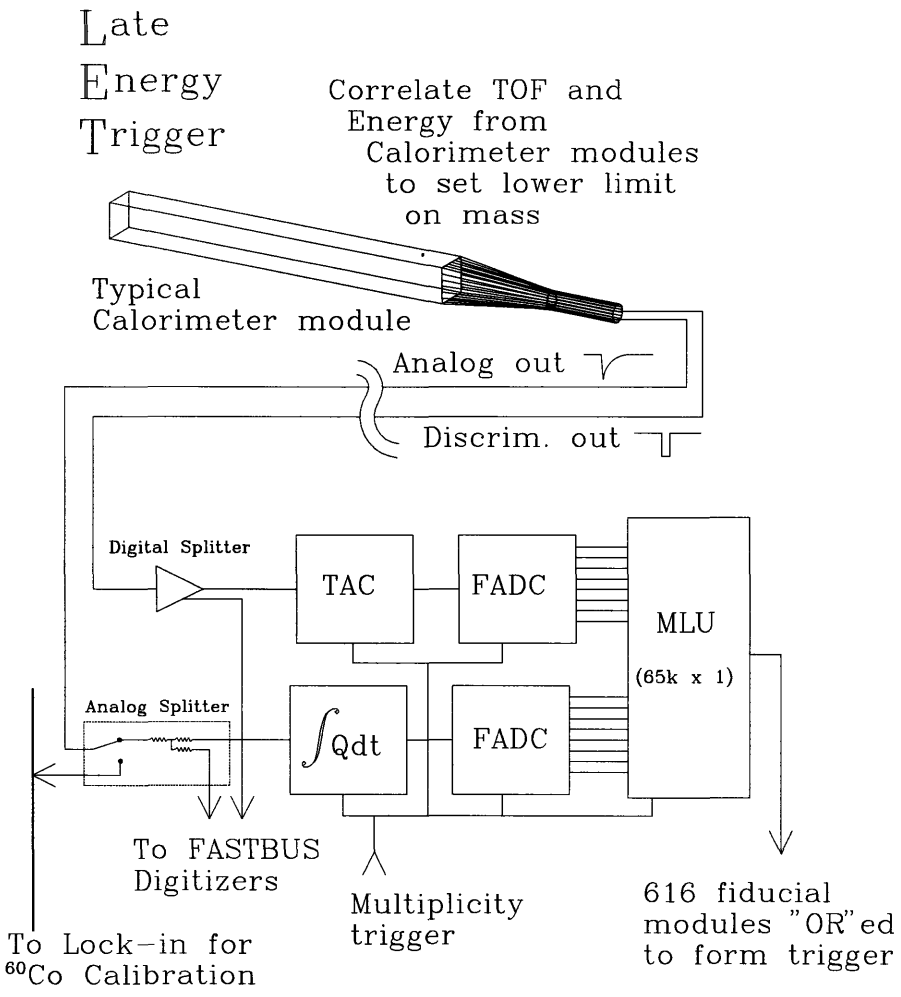

Figure 2-21: LET trigger hardware architecture.

time phase space.[7] In this example, protons and neutrons, which both have a mass approximately equal to A and therefore share very similar curves, and hypothetical mass 5A strangelets are shown. An example LET cut is also shown which selects the strangelets, but not the protons and neutrons. The LUT in this case would give a positive trigger response for hits above the cut, and a negative response for hits anywhere else. The LET cut can also help select slower particles which appear to be

[7]It should be noted that antimatter will have a different curve in this phase space than will ordinary matter with the same mass. Additional energy from the annihilation will shift the curve up along the energy coordinate for antimatter.

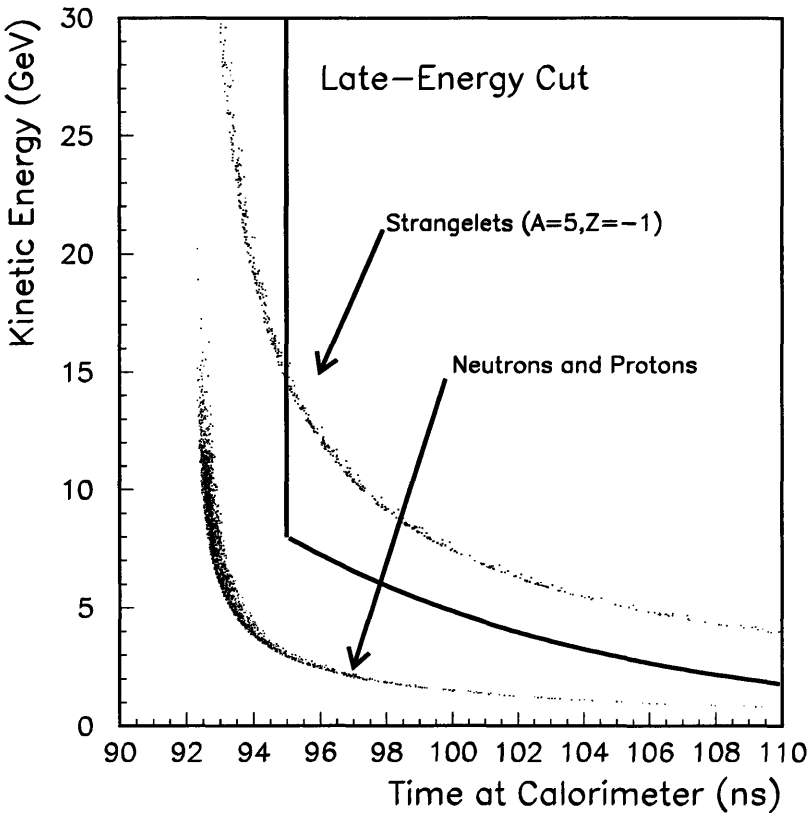

Figure 2-22: Spectrum of various particles in energy and time as seen by the LET using Monte Carlo data. An example LET curve is drawn which selects slow, high mass particles such as strangelets.

from midrapidity (as opposed to beam rapidity protons and beam fragments).

The selection of whether to trigger is made on an individual tower by tower basis, and the final trigger is a logical OR of the individual tower triggers.[8] If no towers trigger the LET, then the event is disregarded.

Figure 2-22 was created using Monte Carlo data. In reality, the finite resolutions of the calorimeter in both energy and time mean that the mass cut-off with the trigger

[8]Towers on the outer edges of the calorimeter are excluded from the LET because it is difficult to reconstruct the full energy of showers in which a significant portion of the energy may have exited through the side of the calorimeter. Thus, only 616 of the 754 calorimeter towers are in the fiducial region for the LET.

is not so sharp. Additional smearing comes from the fact that the LET samples individual towers, while particle showers are generally distributed over several towers. A hadron which creates a shower in the center of a tower will deposit more of its energy in a single tower than will a hadron which showers at the interface between two towers.

2.7 Data Acquisition (DA)

Once an event has been selected as interesting, it must be recorded for subsequent analysis. Figure 2-23 presents the layout of the E864 data acquisition system (DA) architecture. Hodoscope, beam counter, and calorimeter ADCs and TDCs are read from four FASTBUS crate controllers into separate VME memory buffers. Straw tube information is collected in CAMAC along with event descriptive information. The CAMAC data is multiplexed into a single VME memory buffer. One final memory buffer receives any information which is to be kept from the LET logic. Eight event builders gather the event pieces from each memory buffer and output the data to individually controlled Exabyte 8mm dual density tape drives. A portion of the recorded events are also distributed in an online system which allows continual monitoring of the detector performances.

This DA arrangement permits a mixture of trigger types (i.e. INT0, INT2, LET) to be recorded in the data stream with easily changed mixture ratios. In the 1996-1997 data set, approximately 91% of the recorded data was taken using the LET trigger, about 7% requiring only an INT2 trigger, $\sim$1% with INT0 triggers, and $\sim$1% other trigger types.

The E864 DA was designed to record 3.6 million events per hour. This estimate assumed an event size of 6000 bytes, and 4000 events recorded per AGS spill, where one spill arives every four seconds and lasts for one second. During the 1996-1997 run, the spill duration was extended to 1.5 seconds, and the event size was reduced to $<$5000 bytes. Peak DA rates reached $\sim$1.0 million events per hour, with duty cycles from down times reducing the run average to only $\sim$0.5 million events per hour.

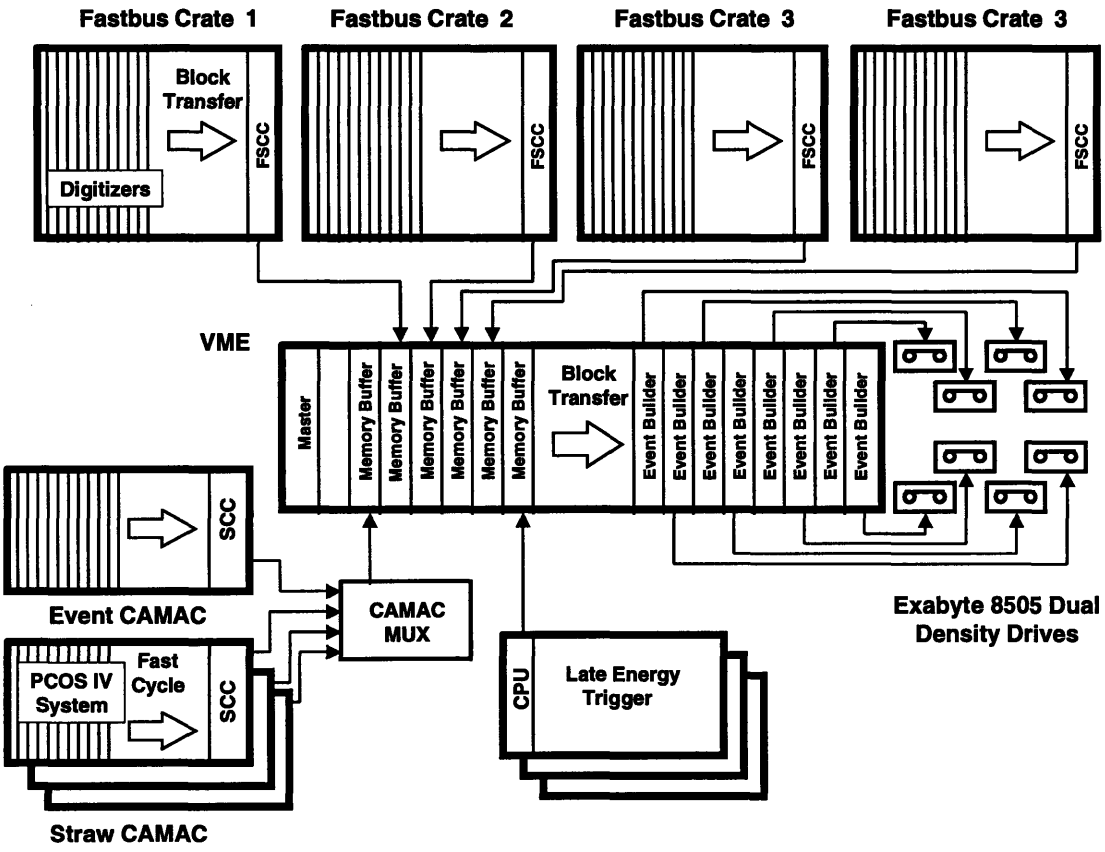

Figure 2-23: The E864 data acquisition system.

Chapter 3

Calibrations

Before analyzing the data set from the experiment, the data must be calibrated for accurate measurements using the spectrometer's detectors. This chapter will detail those calibrations.

3.1 Beam Counters

Beam counter calibrations are done necessarily before calibrating other detectors. This is because the beam trigger counter start times must be subtracted from all the other detectors to remove any fluctuations in TDC spectra which are due solely to the electronic gates set by the beam trigger counters. For the beam counters, pedestal, slew, and time offset corrections are necessary.

3.1.1 Pedestals

The ADC pedestals for the beam counters have significant fluctuations due to 60 Hz coupling through signal grounds from power sources for the experiment. Despite efforts to remove the coupling, some fluctuations remained. Fortunately, the periodicity of the fluctuations allowed a simple solution: a microsecond (μs) counter is included in the data stream, which is reset to zero every 1/60th of a second (about 16,667 μs). This counter serves as a clock, indicating the time point during a 60 Hz

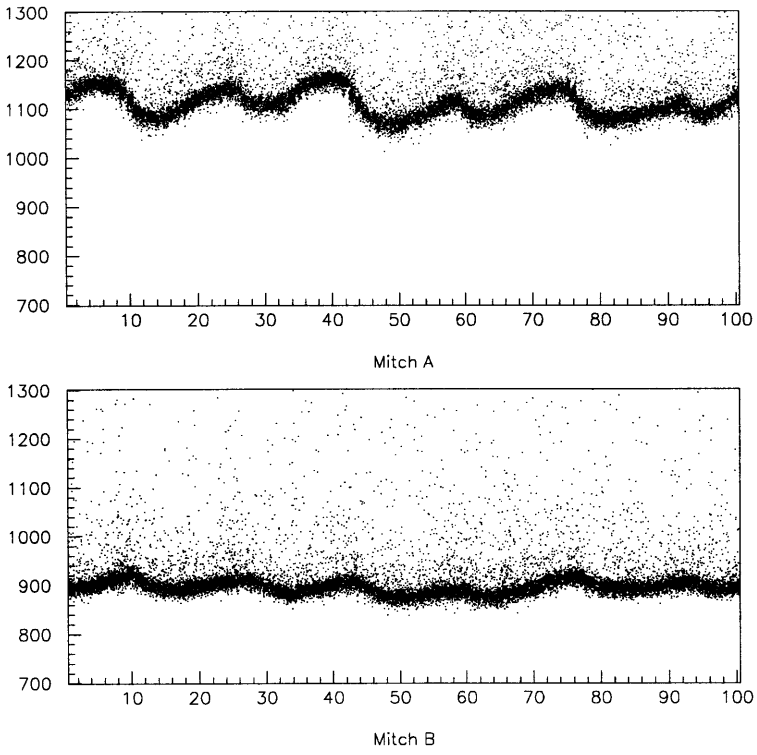

Figure 3-1: Beam counter ADC pedestals for Mitch A & Mitch B as a function of clock bins.

cycle at which the event was recorded.

Every pedestal event is then categorized by one of the 100 bins into which 60 Hz cycles are divided (each bin is 16.667 μs wide). As seen in Figure 3-1, this method of characterizing the coupling works quite well. For each of the 100 clock bins, a weighted average over 40 ADC bins centered on the bin with the most hits is calculated for the pedestal value. The large dots in Figure 3-1 show that reasonable pedestal values are found this way.

The 60 Hz correction and pedestal subtraction are performed for all beam counters and are determined for every run.

3.1.2 Slew Curve

As is well understood, a slewing effect is introduced into the discriminated time spectra of PMT pulses from the spread in pulse heights. This slewing effect can be corrected, and the standard formula used for this correction is

$$t_{true} = t_0 - (\beta + \frac{\alpha}{\sqrt{\mathcal{A}}}) \tag{3.1}$$

where $\mathcal{A}$ is the 60 Hz corrected and pedestal-subtracted ADC value. t_0 is the raw TDC value shifted by a constant such that its mean value is zero. α is defined as the slew curve parameter and is proportional to the amount of slewing present. β is a constant which is used to return the mean of the time distribution to zero after the slew correction.

The TDCs used in the 1996-1997 run of E864 have 25 picosecond bins, and the ADCs have 25 picocoulomb bins. The slew correction is performed before the conversions from TDC and ADC units to picoseconds and picocoulombs respectively, and the scale of the constants determined reflect that.

In determining the slew curve parameters, care must be taken to use a gate-independent technique. The time difference $(t_B - t_A)$ for the two PMTs of a beam counter should have a random, Gaussian distribution about zero with a sigma equal to the error on the measurement, and should be gate independent since the gate time is subtracted out. Assuming the parameterization of Equation 3.1, we find the following:

$$\begin{aligned} t_B - t_A &= \left[t_{B0} - (\beta_B + \frac{\alpha_B}{\sqrt{\mathcal{A}_B}})\right] - \left[t_{A0} - (\beta_A + \frac{\alpha_A}{\sqrt{\mathcal{A}_A}})\right] \\ &\approx 0 \end{aligned}$$

$$\begin{aligned} t_{B0} - t_{A0} &= (\beta_B + \frac{\alpha_B}{\sqrt{\mathcal{A}_B}}) - (\beta_A + \frac{\alpha_A}{\sqrt{\mathcal{A}_A}}) \\ &= \beta_0 - \frac{\alpha_A}{\sqrt{\mathcal{A}_A}} + \frac{\alpha_B}{\sqrt{\mathcal{A}_B}} \end{aligned} \tag{3.2}$$

The shape of the distribution for $(t_{B0} - t_{A0})$ should be a Gaussian about the curve described by the right side of Equation 3.2.

For each event i collected, we have

$$\begin{aligned} b_i &\equiv t_{B0} - t_{A0} \\ f(\mathcal{A}_{Ai}, \mathcal{A}_{Bi}, \beta_0, \alpha_A, \alpha_B) &\equiv \beta_0 - \frac{\alpha_A}{\sqrt{\mathcal{A}_{Ai}}} + \frac{\alpha_B}{\sqrt{\mathcal{A}_{Bi}}} \\ \mathcal{F} &\equiv \sum_i \frac{[b_i - f(\mathcal{A}_{Ai}, \mathcal{A}_{Bi}, \beta_0, \alpha_A, \alpha_B)]^2}{\sigma_i^2} \end{aligned}$$

$\mathcal{F}$ represents the variance assuming a Gaussian distribution of b_i about the curve f. The minimization of $\mathcal{F}$ will then determine the slew curve parameters. This is done by setting the partial derivatives of $\mathcal{F}$ with respect to each of the desired variables equal to zero. Since σ_i, the error of the measurement for each event i, should be the same for all events, it can be set equal to σ_0.

$$\begin{aligned} \frac{\partial \mathcal{F}}{\partial \beta_0} &= 0 = \sum_i -2\frac{[b_i - f]}{\sigma_0^2} \\ \frac{\partial \mathcal{F}}{\partial \alpha_A} &= 0 = \sum_i 2\frac{[b_i - f]}{\sigma_0^2 \sqrt{\mathcal{A}_{Ai}}} \\ \frac{\partial \mathcal{F}}{\partial \alpha_B} &= 0 = \sum_i -2\frac{[b_i - f]}{\sigma_0^2 \sqrt{\mathcal{A}_{Bi}}} \end{aligned}$$

The factors of $\frac{2}{\sigma_0^2}$ cancel out and these three equations expand to give the following:

$$\begin{aligned} 0 &= \left(\sum_i b_i\right) - \beta_0 \left(\sum_i 1\right) + \alpha_A \left(\sum_i \frac{1}{\sqrt{\mathcal{A}_{Ai}}}\right) - \alpha_B \left(\sum_i \frac{1}{\sqrt{\mathcal{A}_{Bi}}}\right) \\ 0 &= \left(\sum_i \frac{b_i}{\sqrt{\mathcal{A}_{Ai}}}\right) - \beta_0 \left(\sum_i \frac{1}{\sqrt{\mathcal{A}_{Ai}}}\right) + \alpha_A \left(\sum_i \frac{1}{\mathcal{A}_{Ai}}\right) - \alpha_B \left(\sum_i \frac{1}{\sqrt{\mathcal{A}_{Ai}\mathcal{A}_{Bi}}}\right) \\ 0 &= \left(\sum_i \frac{b_i}{\sqrt{\mathcal{A}_{Bi}}}\right) - \beta_0 \left(\sum_i \frac{1}{\sqrt{\mathcal{A}_{Bi}}}\right) + \alpha_A \left(\sum_i \frac{1}{\sqrt{\mathcal{A}_{Ai}\mathcal{A}_{Bi}}}\right) - \alpha_B \left(\sum_i \frac{1}{\mathcal{A}_{Bi}}\right) \end{aligned}$$

This gives a solvable linear system of equations.

$$\sum_i \begin{pmatrix} 1 & -\frac{1}{\sqrt{A_{Ai}}} & \frac{1}{\sqrt{A_{Bi}}} \\ \frac{1}{\sqrt{A_{Ai}}} & -\frac{1}{A_{Ai}} & \frac{1}{\sqrt{A_A A_B}} \\ \frac{1}{\sqrt{A_{Bi}}} & -\frac{1}{\sqrt{A_{Ai}A_{Bi}}} & \frac{1}{A_{Bi}} \end{pmatrix} \begin{pmatrix} \beta_0 \\ \alpha_A \\ \alpha_B \end{pmatrix} = \sum_i \begin{pmatrix} b_i \\ \frac{b_i}{\sqrt{A_{Ai}}} \\ \frac{b_i}{\sqrt{A_{Bi}}} \end{pmatrix} \tag{3.3}$$

Rather than inverting the matrix on the left side of Equation 3.3, it is simpler, and less prone to roundoff errors in computation, to use Gaussian elimination with scaled partial pivoting to solve for the desired variables. Implementing this on a computer is straightforward.

Once the values for α_A and α_B are determined, the time distributions for each PMT after slew correcting can be compared to the distributions before slew correcting to determine the β_A and β_B necessary to keep the mean the same. As a check, β_0 should equal the difference $(\beta_B - \beta_A)$.

To test the technique, 50,000 events from runs 1327 and 1334 from the 1996-1997 data of E864 were analyzed in this manner. Cuts were imposed to insure valid TDC and ADC values in both Mitch and MIC using only LET triggers. The slew curve parameters for run 1334 had been previously approximated. For comparison, all three sets of values for the slew curve parameters of both Mitch and MIC are shown in Table 3.1.

Detector	Run 1327		Run 1334		Approx. 1334	
	α	β	α	β	α	β
Mitch A	2705	-116.9	2649	-115.9	2361	-103.7
Mitch B	1467	-76.1	1475	-76.0	1368	-70.2
MIC A	315	-23.4	275	-20.7	283	-21.3
MIC B	232	-18.0	243	-19.2	237	-20.4

Table 3.1: Mitch and MIC slew curve parameters.

The previous approximation helps to confirm that this technique provides reasonable results. Since this technique includes no estimates, searches, or fits and requires only statistical counting, it is a reliable method for the determination of the slew

curve parameters.

Of the other beam counters, MAC is the only one which is slew-corrected. MAC's slew is easily determined by subtracting the Mitch mean time as a way of removing the gate. Precision timing is not important from the other beam counters.

The slew corrections for Mitch and MIC are determined for every few days worth of running. One set of slew correction parameters is valid for MAC for the entire run.

3.1.3 Time Offsets

Once the ADC values have been pedestal subtracted, they can be used in the slew correction of the TDC values. The slew-corrected TDC values are then centered about some value corresponding to how late the TDC input comes relative to its gate. This time offset is determined for every run for all beam counters by finding a weighted mean in the 5 channels around the peak TDC channel. These offsets are then subtracted to yield a distribution of times centered around zero TDC units. Finally, these offset-subtracted times are multiplied by 25 ps/TDC unit to obtain a true time.

3.2 Hodoscopes

Pedestal and slew time offset calibrations need to be made once per run for the hodoscopes, whereas only one set of tzeros, y offsets, gains, and slew curves is needed for the magnetic field setting. Calibrating the once-per-field-setting constants requires using tracks. But performing tracking requires calibrated hodoscopes. The dilemma is skirted by using the 1995 versions of these constants as a first guess. The validity of this method is justified by the fact that most tracks can be found using the old constants. The original first guesses of the constants were estimated using Monte Carlo data.

3.2.1 Pedestals

Hodoscope ADC pedestals are determined once each run. Both PMTs for each slat are measured independently and are compared to other runs close in time during the experiment to be sure nothing changed significantly. Little or no 60Hz dependence is found in the hodoscope pedestals, so a single value for the pedestal is calculated for each PMT.

The pedestal is measured using pedestal events by simply histogramming the ADCs for each PMT for at least several thousand events. A mean and RMS (σ_{RMS}) for the entire histogram are calculated, and then recalculated using only that portion of the histogram which is between $\pm 4\sigma_{RMS}$ of the mean. The new mean is taken as the pedestal.

3.2.2 Slew Time Offsets

Run-to-run variations in the timing of the hodoscopes are taken into account with the slew time offsets. Such variations may be due to any of a variety of reasons as stated with the beam counters. A measure of these variations is a fit to the peak in the slew-corrected[1] time spectrum of all particles striking the hodoscope during LET events. LET events are chosen because they represent a large portion of the data set, and a common set of events must be used for all timing calibrations of the hodoscopes. This measure will eventually be subtracted from the slew-corrected TDC values to bring this peak near zero.

A histogram is made for each PMT of all slew-corrected TDC values where a TDC measurement was made (the TDC did not time out) as seen in Figure 3-2. The histogram is then fit within a region of the peak with a Gaussian. The location of the Gaussian's peak is then used as a first guess at the slew time offset.

A second pass is then made subtracting off these slew time offsets to fill two new histograms for each hodoscope slat: mean times between the top and bottom PMTs, and time differences between the top and bottom PMTs (divided by two). These

[1]Slew correction will be addressed later in Section 3.2.6.

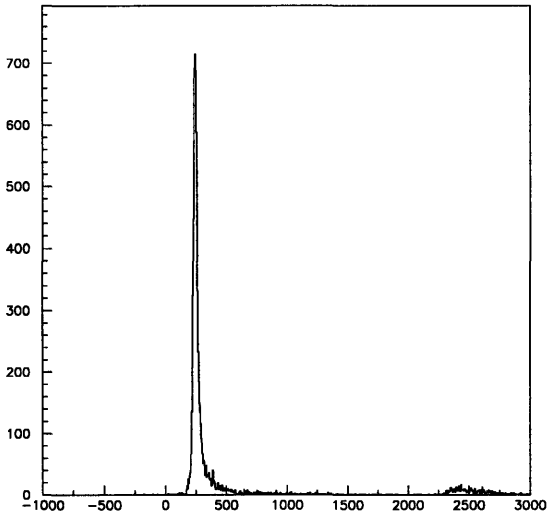

Figure 3-2: Slew corrected TDC spectrum for hits in one PMT of a hodoscope slat.

histograms are filled only for hodoscope hits where both PMTs yielded valid ADC and TDC information, and where the absolute value of the logarithm of the ratio of the pedestal subtracted top and bottom ADCs is less than 0.1. This last requirement restricts the hits used to those where the the passing particle came very close to the vertical center of the slat.

With the second pass histograms, the slew time offsets can be readjusted. Both the time difference and the time mean distributions are fit with a Gaussian to find a peak value. The adjustment for one PMT's slew time offset is then the difference of the two new values, while the adjustment for the other PMT on the same slat is the sum of the two new values.

3.2.3 Tzeros

Tzeros are added to the slew-corrected, slew time offset-corrected times from each PMT to yield a true time. The average of the true times for the top and bottom PMTs of a given slat then indicate the time at which a particle passed through the slat. Since run-to-run variations are compensated in the slew time offsets, only one

set of hodoscope tzeros needs to be calculated for this field setting of the experiment.

Tracks are required to calibrate the tzeros. But since tzeros are needed to find tracks in the first place, the tzeros from the 1995 run are used as initial guesses. That they may be incorrect for the data at hand is not important, as long as they are close enough to being correct that tracks can be found using loose cuts on the determination of a track. As stated previously, the very first tzeros for the experiment were estimated using Monte Carlo data.

With determined tracks, cuts can be placed on the tracks to insure that they are pions, kaons, or protons. Several species must be used as no single species has geometrical acceptance over the entirity of the hodoscopes at the -0.75T field setting of the experiment. Using the known mass of the particles, the velocities can be determined fairly accurately using the momentum of the track, in turn derived from the rigidity of the track (as measured by its path) divided by the charge. The charge determination requires the gains calibration as well, but using the gains from the 1995 run is sufficient for the tzero calibration because they have not changed significantly, a point justified only by doing the charge calibration as well to see that the gains have not changed much.

The pathlength to the hodoscope slat divided by the velocity then provides a time at the hodoscope slat. The difference between the times as calculated from the track and the time as calculated using only the hodoscope information (with slew correction, slew time offsets, and old tzeros added) is a measure of how much the old tzeros must be adjusted for the new data. These differences are histogrammed for each slat as shown in Figure 3-3, and the location of the peak of a Gaussian fit is used to adjust the old tzeros.

3.2.4 Y Offsets

The difference in true times for the top and bottom PMTs of a given slat relate to the y position for a particle which passed through the slat. The y position is simply some y offset plus the product of the time difference (divided by 2) with the speed of light

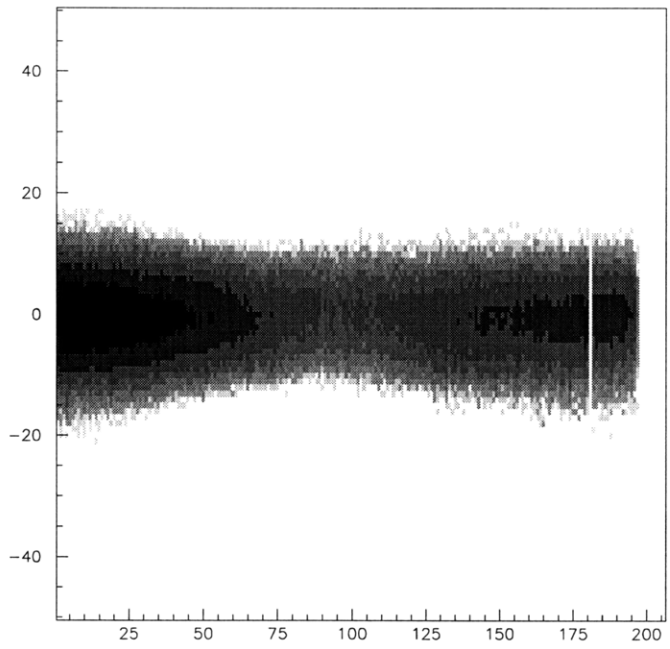

Figure 3-3: Distribution of differences between times as calculated from tracking and times as calculated using only the hodoscope information for H3. Protons dominate the spectrum at low slat number (negative x direction), and negative kaons and pions fill out the histogram for higher slats. Some missing hodoscope channels can be seen.

in the scintillator.[2] This calculation can be compared for hits from tracks in a slat to the y position of the path that tracking has determined at that slat. The differences from this comparison are histogrammed, and fit with a Gaussian. The location of the Gaussian peak provides the adjustment which must be made to the old y offsets.

3.2.5 Gains

The gain of a PMT must be calibrated to correspond with the charge of the particles which hit the slat. Fortunately, the resolution of the ADC spectrum from the PMTs is good enough that the charge separation is sufficient to find the gain. The distribution of the pedestal-subtracted ADC spectrum, as seen in Figure 3-4, is fit with a Gaussian

[2]Calibration of the speed of light in the scintillators will be addressed in Section 3.2.7.

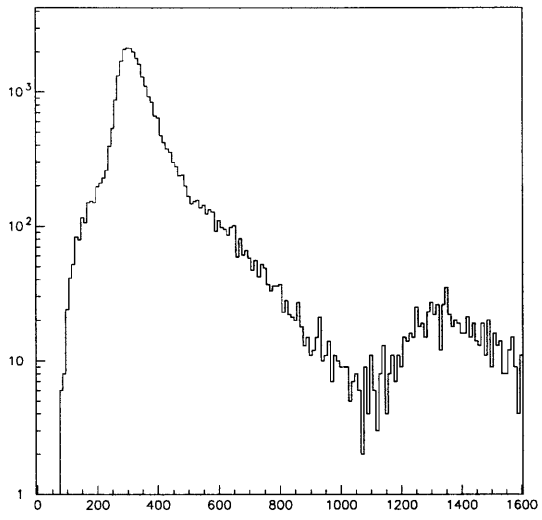

Figure 3-4: Pedestal-subtracted ADCs for tracks in a hodoscope slat.

about the peak associated with charge equal to one for each PMT. Figure 3-4 shows no pedestal ADCs because ADC values near a nominal pedestal are suppressed in the data acquisition for non-pedestal events to reduce the event data size.

3.2.6 Slew Curves

Because all the hodoscope slats and lightguides are identical within each of the three hodoscope planes, one slew curve is used for each plane. For initial track finding, the slew curves from last year are adequate. With tracks, the times given by the hodoscopes can be compared to the times as given by the projection of a fit to the other time and pathlength points along the associated tracks. This time difference can then be plotted versus the ADC values of the top and bottom PMTs to see if any slewing still exists.

The old slew curve parameters yield sufficiently ADC-independent time differences for the 1996-1997 data set. These parameters are shown in Table 3.2 and are used in

the following formula for the slew:

$$\text{Slew} = \frac{\text{P1}}{\sqrt{\mathcal{A}}} + e^{\text{P2}+(\text{P3}\times\mathcal{A})} \tag{3.4}$$

where $\mathcal{A}$ is the pedestal-subtracted ADC value for a PMT.

Plane	P1	P2	P3
H1	611.958	6.12674	-2.4×10^5
H2	825.160	5.41690	-4.9×10^5
H3	1094.232	4.41321	-1.0×10^4

Table 3.2: Hodoscope slew curve parameters.

3.2.7 Effective Speed of Light

It is necessary to know the effective speed of light in the hodoscopes in order to relate time differences between the top and bottom PMTs with y positions. It should be noted that the effective speed of light in the hodoscopes (v_{light}) is less than the true speed of light in the scintillator because much of the light does not travel directly to the PMTs, but reflects off the walls of the slats several times on a zig-zag trajectory.

To find this, one can compare y positions calculated from fit tracks with the y positions for hodoscope hits. If no systematic shift is found as a function of y position, then the speed of light is correct. Tracks are found using the previous year's numbers for the speed of light in each of the three hodoscope planes. All slats within a plane are approximated to have the same light speeds.

The effective speed of light was found to have changed slightly from the previous year. This decrease in the effective speed can be attributed to mechanical stresses causing minute defects in the hodoscope scintillators. Once the effective speeds were corrected, the comparison plots for the three planes all looked similar to the one shown in Figure 3-5, with the spectrum lying along a 45° line through zero. The effective speed of light for the three hodoscopes is shown in Table 3.3.

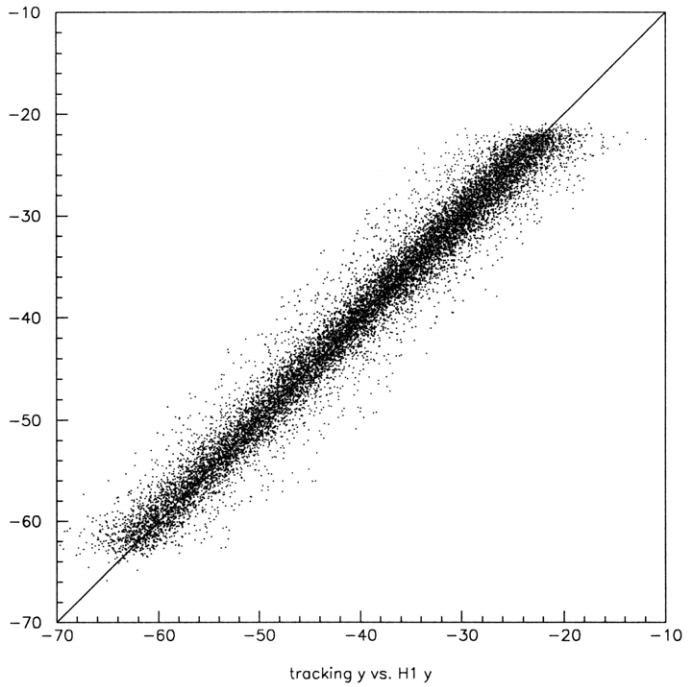

Figure 3-5: Comparison of y positions from the fit track with those from the hodoscope for tracks through H1.

3.2.8 Resolutions

The time resolution (σ_t) and y position resolution (σ_y) of the hodoscopes can be determined by comparing the quantities given by an individual hodoscope with the projection of tracks at that hodoscope. Because the track projections can be made with and without using the hodoscope under examination in the track fit, two distributions can be found for these differences. Using the widths of the distributions including the hodoscope (σ_{in}) and excluding the hodoscope (σ_{ex}), one can calculate a more accurate σ using the formula[3]

$$\sigma = \sqrt{\sigma_{ex}^2 - \sigma_{old}^2 \left(\frac{\sigma_{ex}}{\sigma_{in}} - 1 \right)} \tag{3.5}$$

where σ_{old} is the resolution which was used when making the inclusive track fits.

[3]See Appendix A for the derivation of Equation 3.5.

Because the y position is determined from the time difference, one might naively think that the following relationships should hold:

$$\sigma_y = \sigma_t \cdot v_{light} \tag{3.6}$$

However, this equation relies on the assumption that the mean time and its resolution are independent of y position of the track. Whether or not this assumption is close to the truth, it is more accurate to calculate σ_t and σ_y independently using Equation 3.5.

Using the 1995 values for the resolutions as starting points, new values were found when the calculations converged after only a few iterations on about 1.5 million events. These new resolutions are shown in Table 3.3. One set of resolutions is found for each plane and is used for the entire 1996-1997 data set.

Plane	v_{light}/c	σ_y (cm)	σ_t (ps)
H1	0.4678	1.45	138
H2	0.4987	1.70	130
H3	0.4993	1.95	160

Table 3.3: Hodoscope resolutions and effective light speeds.

3.2.9 Efficiencies

The hodoscopes do not provide complete information for every track. In some cases, a particle may go between slats (space is provided for the foil wrappings), or not traverse the entire depth of a slat. The latter has a significant probability at high magnetic field settings where particle trajectories may be bent significantly away from normal to the plane of the hodoscopes, causing particles to pass through the corner of one slat and even cut diagonally across two slats. These effects can cause small pulses from the PMTs which may be indistinguishable from background by the ADCs and TDC discriminators, resulting in some inefficiency for finding track-associated hits in the hodoscopes.

Hodoscope efficiencies may be determined by excluding planes from the track-finding process. To help insure that the tracks found are still real, the requirements that the track has hits in all six straws planes, and has good χ^2 values can be imposed. These requirements should have no impact on efficiencies calculated for real tracks because the probability of a real track firing all six straw planes and having a good fit in the other detectors should be uncorrelated with the efficiency of the unincluded hodoscope plane.

These tracks found without the use of the particular hodoscope plane being examined can be projected to the hodoscope plane to see if any corresponding slats are hit. The percentage of tracks that have hits in the plane then yields the efficiency of that plane.

To determine if a hit was indeed found in the plane which corresponded to the track, each track is projected to the plane of the hodoscope, and the position of the projection is used to determine a slat. Since there is some error in the projection, the slat and its two neighbors are considered for the hit. If more than one of these three slats is hit, the slat closest to the track in x is selected. If indeed a hit slat is found, a requirement is then made that both of the slats PMTs give valid ADC and TDC information.

Since it is possible that the hit found in the hodoscope plane may truly be associated with a track other than the one in question, due to track overlap within the three slats, there is some error in this efficiency calculation. This contribution is considered to be negligible for this analysis.

Because the efficiency of a plane actually includes some slat-to-slat variance, and the track occupancies vary across the plane, the efficiency of the plane as a whole should be calculated independently for each field setting. For this analysis, efficiencies have been found as a function of position at the -0.75T field setting, and a statistically weighted mean has been found for the entire plane.

Figure 3-6 shows the efficiencies across the planes and the weighted fits. Bins in which there are bad slats or particularly low statistics are left out of the fits. In particular, the gaps in the H2 and H3 data are a direct result of the separation of

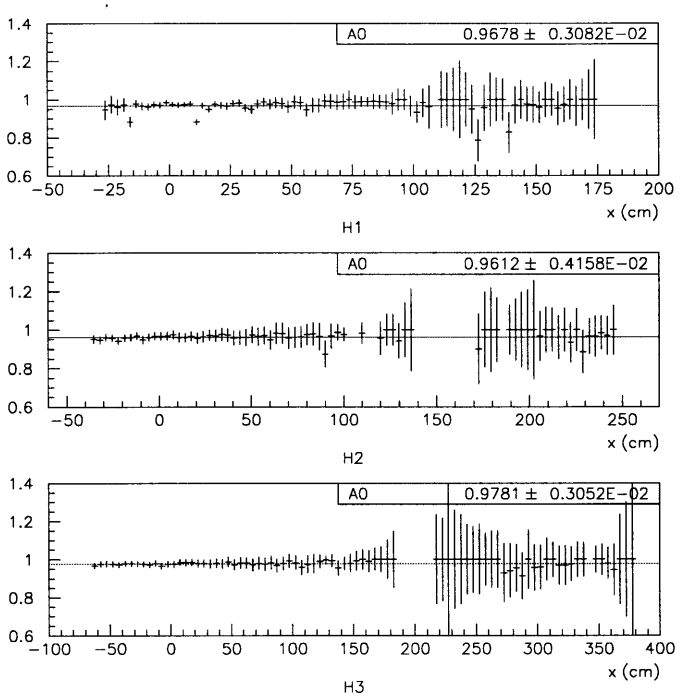

Figure 3-6: Efficiencies of the hodoscope planes H1, H2, and H3 as a function of position. Some modestly inefficient slats can be seen in H1.

positively charged and negatively charged particles in the spectrometer. Negatively charged antiprotons constitute the large x data, whereas positive light nuclei populate low and negative x regions. Because there are many more positive particles than negative, the statistical errors are much smaller at low and negative x. The resulting efficiencies are 96.8%, 96.1%, and 97.8% for H1, H2, and H3 respectively.

3.3 Straws

The only calibration necessary to find tracks with the straws is positional alignment. This is because the straws provide no information other than a hit or miss at specific positions for charged particles traversing the spectrometer.

3.3.1 Alignment

The straws provide track coordinates with significantly better accuracy than the hodoscopes; therefore, accurate straw positioning is important. Care is taken to correctly survey the straw chamber positions before the exeperiment run. Once data has been taken, checks can be made to see if the straw positions used are indeed accurate.

For the location of straws along the x axis, the calculated x position of tracks at the S2X and S3X planes can be compared to the positions of the associated hit tubes. The difference of these positions is histogrammed as seen in Figure 3-7 to get an idea of how well they agree. The positions of S2X and S3X appear very well described by the survey as both histograms are centered quite close to zero.

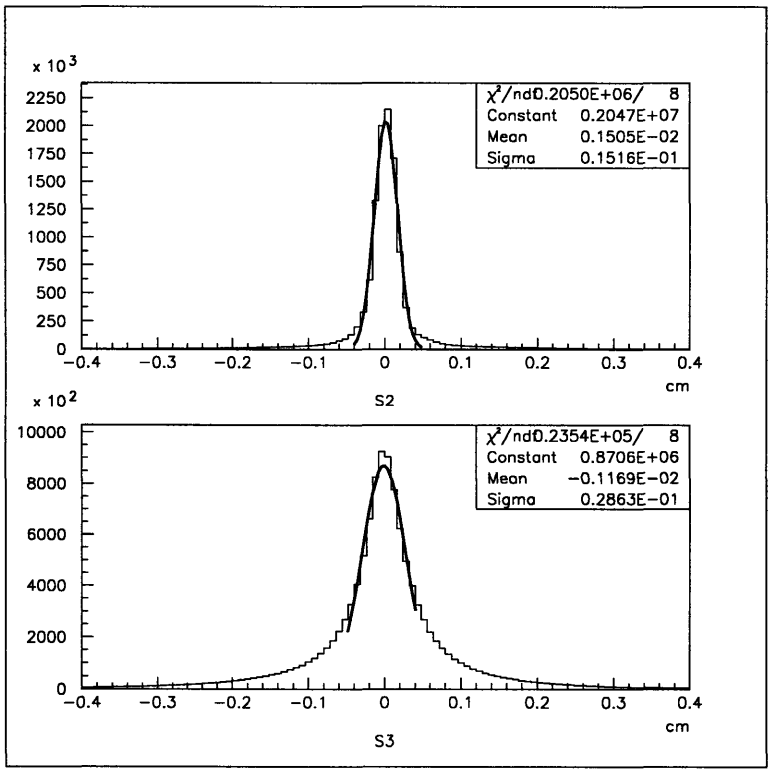

Figure 3-7: Difference between x positions of tracks and associated straw hits in S2X and S3X.

Since the y positions of tracks from the straw chamber measurements are used in calibrating the y positions of the hodoscope measurements, the technique used

for the check on x axis positioning is not viable for the y axis positioning. For this check, the target can be employed. Tracks are extrapolated back to the target in the y-pathlength coordinate system using the location of hits from S2 and S3 in the U and V planes, and their y intercept is histogrammed. Since the y positions are determined using the U and V planes together, a point half way between the two plans is assumed to have that y position.

Figure 3-8 shows the y intercepts as a function of where the tracks hit S3X. Low x is dominated by positive tracks, and high x by negative tracks. A linear fit has been made to the y intercept peaks as a function of x. On the left edge of the plot, the y intercepts are peaked at about 0.04 cm, and at about -0.32 cm on the right edge.

The main point of this histogram is that the y intercepts are quite well centered about zero. The small differences that exist will have insignificant impact on measurements of the momentum vector, but will contribute to the χ^2 calculations.

It should be made clear that this is not a direct measure of the tilt in S2 or S3 individually. But it is clear that tracks are reconstructed with y coordinates which have a small dependence on which side of the detector they traverse. This may be due to a tilt in either S2, S3, or both, or slight vertical bending in the fringe fields of the magnets. The errors are not significant enough to merit determination of their exact cause.

3.3.2 Resolutions

The spatial resolution of straw hits is purely geometric. But because clusters of hit tubes are used for hit positions, the error on the position is dependent upon the number of straws hit. The uncertainties of the x position measurements are square, so the error on the measurements are the widths of the uncertainties divided by $\sqrt{12}$. Because the straws are arranged in two staggered planes, the general formula for the errors of measurement from the X planes, with the exception of a cluster size of 2, is

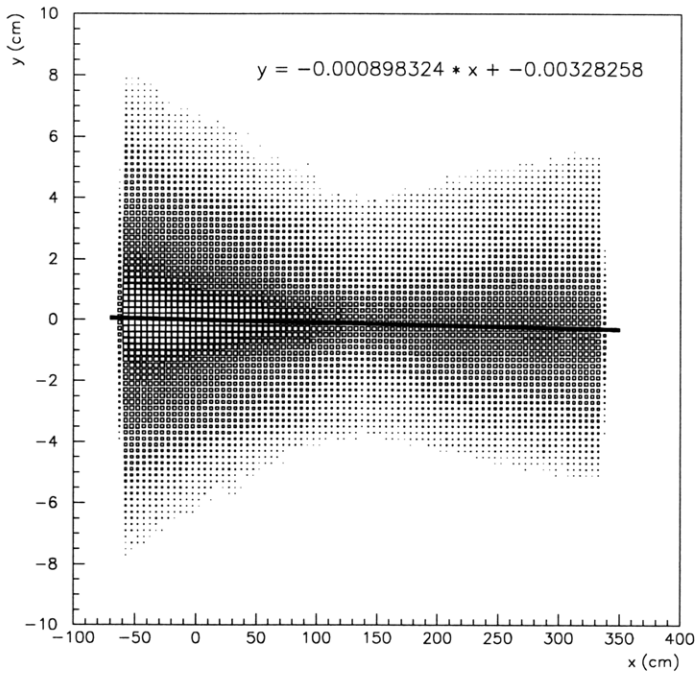

Figure 3-8: Y intercepts in the y-pathlength coordinate system using y positions determined from the U and V planes of S2 and S3.

the following:

$$\sigma = (n+1)\frac{r}{\sqrt{12}} = (n+1)0.0577\text{cm} \tag{3.7}$$

where n is the cluster size, and r is the radius of a straw (0.2 cm). With a cluster size of 2, the track is assumed to pass through the region of overlap between the two straws, which is only a single straw radius wide. So for $n = 2$, the formula becomes

$$\sigma = \frac{r}{\sqrt{12}} = 0.0577\text{cm} \tag{3.8}$$

Vertical measurements require hits in both a U and a V plane at either S2 or S3. The resolution of this measurement is rather complicated. For each plane, a track found with the hodoscopes and X straw planes is projected to the plane. The cluster nearest to the projection point is assigned to the track, and the y position of the

middle of the cluster's tubes at the x coordinate of the projected point is assigned to the track. The error associated with this assignment is quite complex. Clearly, the error along the axis perpendicular to the tubes' long axis (call it the p axis) follows the same formula as described above for the X planes. If the x coordinate is known without error, then indeed this would translate into an error along the y axis which is simply the error along the p axis divided by $\sin\theta$ (θ is the angle of the straws from vertical).

However, there is some error in the determination of the x coordinate. This error must be convoluted with the square error to get the true error. Since this is a difficult calculation, and since the error in the x coordinate is actually much smaller than the error in y, the x coordinate is assumed to be exact for the calculation of the y resolution.

Thus, the formula used for the errors on y positions as found by either a single U or V plane is

$$\sigma = (n+1)\frac{r}{\sqrt{12}\sin\theta} \approx (n+1)0.17\text{cm} \tag{3.9}$$

for $n \neq 2$, and

$$\sigma = \frac{r}{\sqrt{12}\sin\theta} \approx 0.17\text{cm} \tag{3.10}$$

for $n = 2$.

With the track points determined for the U and V planes, a new point half way between the two is used for the y and z positions when fitting the track in the y-z and y-pathlength planes. For these fits, the error on the y position is then the RMS of the U and V errors,

$$\sigma_{S2} = \sqrt{\sigma_{S2U}^2 + \sigma_{S2V}^2} \tag{3.11}$$

$$\sigma_{S3} = \sqrt{\sigma_{S3U}^2 + \sigma_{S3V}^2}\ . \tag{3.12}$$

3.3.3 Efficiencies

Efficiencies can be calculated using tracks. Because tracking may be performed using only some of the straw planes with reasonable efficiency, the efficiency for a given plane can be approximated by counting the number of tracks found with hits in the plane, and dividing by the total number of tracks found which pass through the active portion of the plane. The efficiencies for the six straw planes from two different runs are shown in Table 3.4.

Plane	Run 1190 (%)	Run 1350 (%)
S2V	96.05	96.22
S2X	96.98	96.99
S2U	96.71	96.78
S3V	95.84	96.32
S3X	98.05	98.14
S3V	96.97	97.05

Table 3.4: Straw plane efficiencies for two separate runs. Efficiencies are fairly consistent throughout the entire data set.

Since tracking is performed requiring only four of the six straw planes, the combined efficiency of the straws together is actually quite good. This can be calculated as follows. By taking the probablility for a hit in each straw plane, one can calculate the total probability that an event had any particular arrangement of straw plane hits and straw plane misses. Summing the probabilities for all cases where at least four planes are hit yields the probability that a track will be found.

After working out the combinatorics, the final efficiency of recording a hit in at least four of the straw planes comes out to be 99.95%. This is much better than the ~83% efficiency of requiring all six straw planes. This is also significantly better than other efficiencies in the tracking. Certainly, once the other tracking efficiencies are included, any difference between the calculated straw efficiency and 100% efficiency is negligible. For this analysis, the straw planes are considered to be 100% efficient for tracking.

3.4 Calorimeter

The calorimeter provides energy, time, and position information. Since it provides a redundant measurement of these for tracks, calibrated tracks can be used in the calorimeter calibration process.

3.4.1 Pedestals

Calorimeter pedestals are measured for every run and are measured individually for each tower. No 60Hz correction is necessary. Using pedestal events, a peak ADC value is found, and a three channel interpolation is performed around it to find the pedestal.

3.4.2 Slew Time Offsets

Just as with the hodoscopes, slew time offsets are required with the calorimeter for each run to accomodate any changes in the delay of signals going from the calorimeter towers to their TDCs. For this calibration, all calorimeter signals from a few hundred thousand LET triggered events are used. A peak in the slew curve-corrected TDC spectrum[4] is found and a five channel interpolation about the peak iss performed. This TDC value is then considered the slew time offset for that run.

3.4.3 Tzeros

The tzeros for the calorimeter are found using tracks. It is a simple calculation based on finding the difference between the times that the calorimeter towers give for tracks, and the time projection of the track to the calorimeter face. To start, tzeros from the previous year can be used in calculating the calorimeter tower times. The differences are then histogrammed for all 754 towers and fit with a Gaussian around the peak to determine how far off the old tzeros are. The new tzeros are then the old tzeros corrected for these differences. One set of tzeros is sufficient for the field setting.

[4]Slew curve corrections are discussed in Section 3.4.4.

3.4.4 Slew Curve

For the slew curve, tracks are again useful. One slew curve is used for all calorimeter towers, and is used for the whole data set. Like the tzeros, the differences in times projected from tracking and times measured by the calorimeter towers can be found, but without correcting for slew curves in the calorimeter. These differences can then be plotted as function of pedestal-subtracted ADC values in the calorimeter to find the slew curve. This is more accurate than simply plotting calorimeter times versus ADC values because there is a correlation between the energy of particles and their times at the calorimeter.

The calorimeter times of course require tzeros and slew time offsets. Unfortunately, the calibrations of the slew time offsets and the tzeros actually require slew curve correction to the calorimeter times. This leads to an iterative solution whereby slew time offsets are first found using the slew curve from the 1995 analysis. These then allow a determination of the tzeros, and a recalculation of the slew curves. The new slew curves then go back into the slew time offset calibration and the process is repeated. After many iterations, all three calibrations appear to converge on reasonable values. The slew curve found is then used for the determination of slew time offsets in all runs.

The calorimeter slew curve parameterization is similar to that for the hodoscopes.

$$\text{Slew} \;=\; \text{P1} + \frac{\text{P2}}{\sqrt{\mathcal{A}}} + e^{\text{P3}+(\text{P4}\times\mathcal{A})} \tag{3.13}$$

Again, $\mathcal{A}$ are the pedestal-subtracted ADCs. To find the parameters of the slew curve, each ADC bin (with a width of ten ADC channels) in the two-dimensional time difference histogram is fit with a five bin (each time bin is 200 ps wide) weighted mean around the peak time difference to find the characteristic time difference for that ADC bin. These characteristic time differences are then fit as a function of the pedestal-subtracted ADC using Equation 3.13 as shown in Figure 3-9. The final parameter values found are shown in Table 3.5.

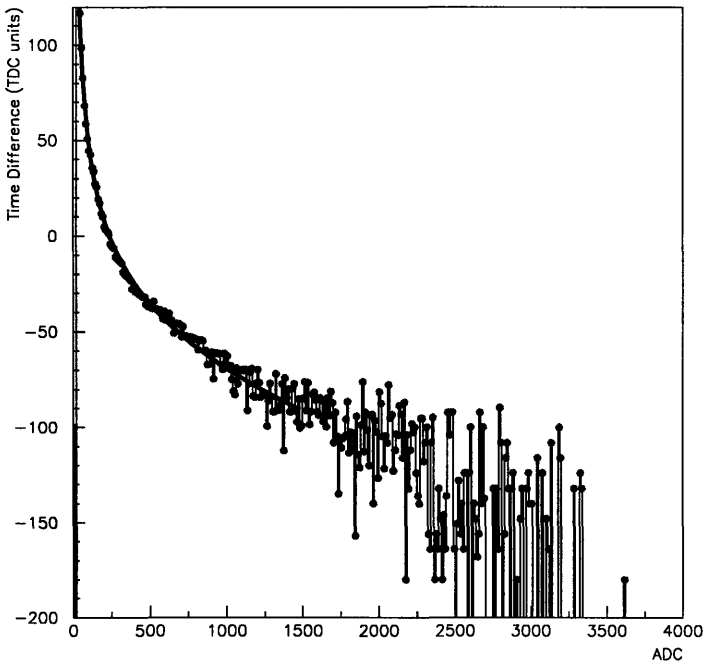

Figure 3-9: Slew curve fit for the calorimeter. Characteristic time differences are fit as a function of pedestal-subtracted ADC.

3.4.5 Gains

The primary technique for gain matching the calorimeter towers is through the use of a ^{60}Co gamma ray source. This source is mounted on a mobile platform which can place the source immediately in front of the face of each individual tower. The source is collimated to shine on only one tower at a time.

Before the experiment, the source was shone on each calorimeter tower for a few seconds, a process taking approximately two hours. An ADC spectrum was taken for each tower during its exposure, yielding an average gain for each tower. The voltages on the PMTs were then adjusted to match the gains for all 754 calorimeter towers. The process was then repeated every few days during the run without changing the voltages. Instead, The average gains were saved as constants to be divided out during analysis to provide gain-matched ADC values for all calorimeter towers.

The next step is to convert the ADC values into energy information. The conver-

Parameter	Value
P1	-241.4664
P2	1265.8262
P3	4.606082
P4	-0.41313E-03

Table 3.5: Calorimeter slew curve parameters.

sion factor is determined by the voltages applied to the calorimeter PMTs and by the arbitrary unit to which the tower ADCs are gain-matched. To find the conversion, identified particle tracks are examined in the calorimeter.

Several constraints are placed on the tracks used in this particular analysis. First, the tracks must be from well-identified particles in order to determine the kinetic energy. Because strangelets are expected to deposit significant energy in the calorimeter, high energy tracks are needed for calibration. Protons alone are not easily identified in the data set at high energies, so deuterons, tritons, and helium isotopes are also included. These particles are expected to deposit only their kinetic energy in the calorimeter. In contrast, antiprotons would also have contributions from their annihilation. And to prevent bias in the calorimeter response from LET triggering, only tracks from non-LET events are used.

The calorimeter energy response is found by summing the energies in a 3×3 array about the peak energy tower associated with a track. While the showers from particles striking the calorimeter can span more then these nine towers, this method provides adequate coverage without integrating too much low-level noise and background. This technique does exclude using tracks which strike the outermost towers of the calorimeter, but provides more coverage than larger size arrays would allow.

The calorimeter response can be histogrammed as a function of track kinetic energies. Figure 3-10 shows the response for tracks with kinetic energies between 5.0 and 6.0 GeV after the appropriate conversion factor has been found. A high side Landau tail to the energy response can be seen in the figure.

The calorimeter energy response is found using tracks with kinetic energies as high

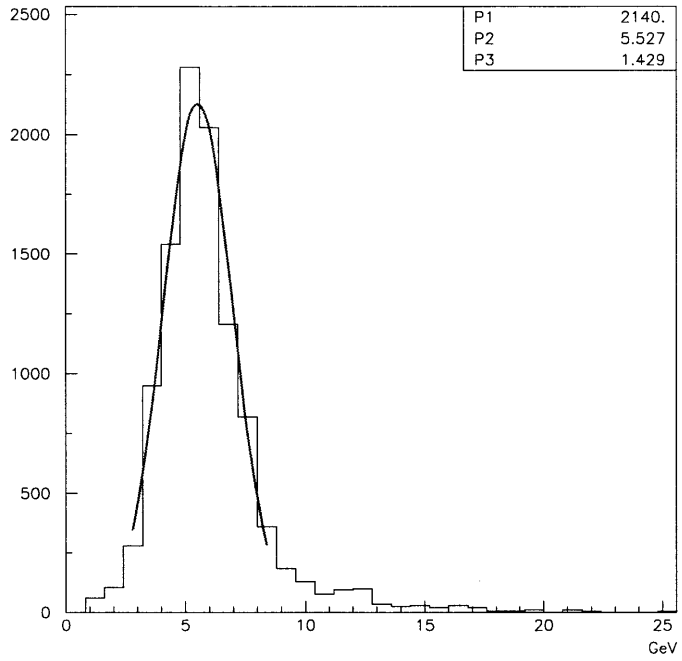

Figure 3-10: Summed calorimeter energy response for arrays of 3 × 3 towers for tracks with kinetic energies between 5.0 and 6.0 GeV.

as 17 GeV. The peaks of the responses are then plotted against tracking kinetic energy to find the conversion factor which makes the slope of a straight line fit through zero to be as close to 1.0 as possible. Figure 3-11 shows this plot once the appropriate conversion factor of 8.61 MeV/ADC channel has been found.

3.4.6 Energy Resolution

Figure 3-10 also shows the energy resolution of the calorimeter for tracks with kinetic energies between 5.0 and 6.0 GeV to be 1.429 GeV. Dividing by the mean kinetic energy of 5.5 GeV yields a percentage resolution of 26.0%. As with the gains, the percentage resolution can be plotted as a function track kinetic energy. Figure 3-12

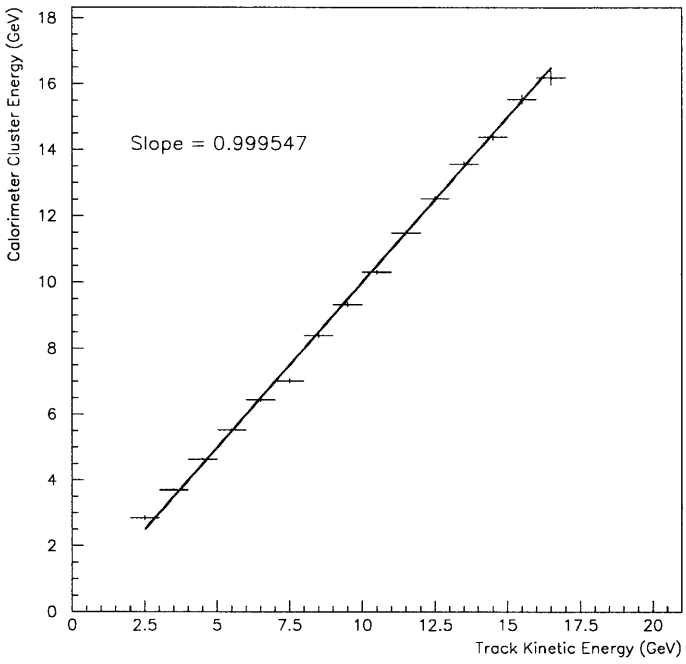

Figure 3-11: Peak calorimeter shower energy responses for different track kinetic energies.

show this plot and a fit to the percentage energy resolution as a function of energy:

$$\sigma(E)/E \;=\; 8.3\% + \frac{38.4\%}{\sqrt{E(\mathrm{GeV})}} \tag{3.14}$$

3.4.7 Annihilation Energy Response

While ordinary hadronic matter such as light nuclei generally deposit only their kinetic energy into the calorimeter showers, the same is not true for antimatter. Antiprotons and antideuterons will annihilate with protons and neutrons in the dense matter of the calorimeter. Not all of the energy from the annihilation is expected to be captured in the shower. The parameter α in Equation 3.15 represents the fraction of

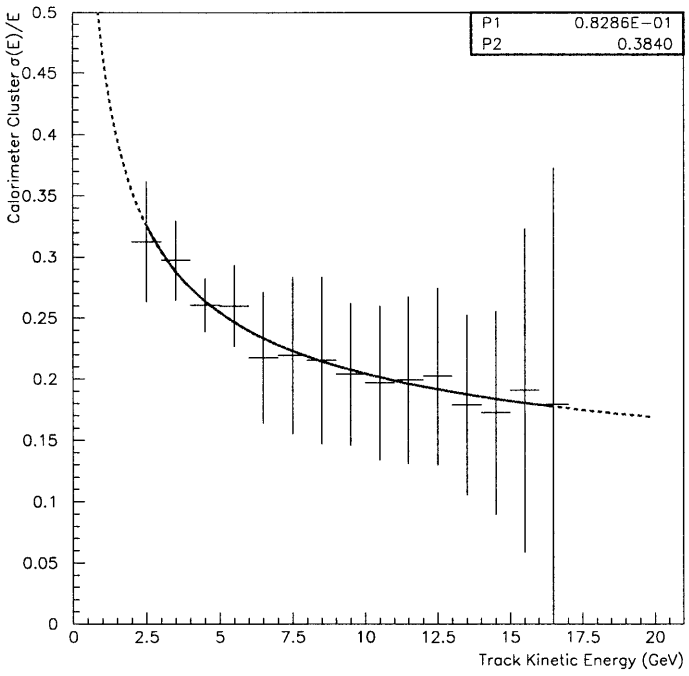

Figure 3-12: Resolutions for calorimeter cluster energy responses for different track kinetic energies.

the annihilation energy seen by the calorimeter.

$$E_{\text{seen}} = \alpha E_{\text{annihilation}} + E_{\text{kinetic}} \tag{3.15}$$

To study this, the calorimeter response to identified antiprotons can be examined. Tracking provides the kinetic energy of these antiprotons, so the excess energy above this seen by the calorimeter is attributable to the annihilation. Antiprotons from non-LET events are required to prevent bias in the energy distribution seen by the calorimeter. For each such antiproton, a value for α can be histogrammed from

$$\alpha = \frac{E_{\text{calo}} - E_{\text{kinetic}}}{E_{\text{annihilation}}} \tag{3.16}$$

with E_{kinetic} found from tracking, and $E_{\text{annihilation}}$ assumed to be twice the antiproton mass (the antiproton is assumed to annihilate with a proton).

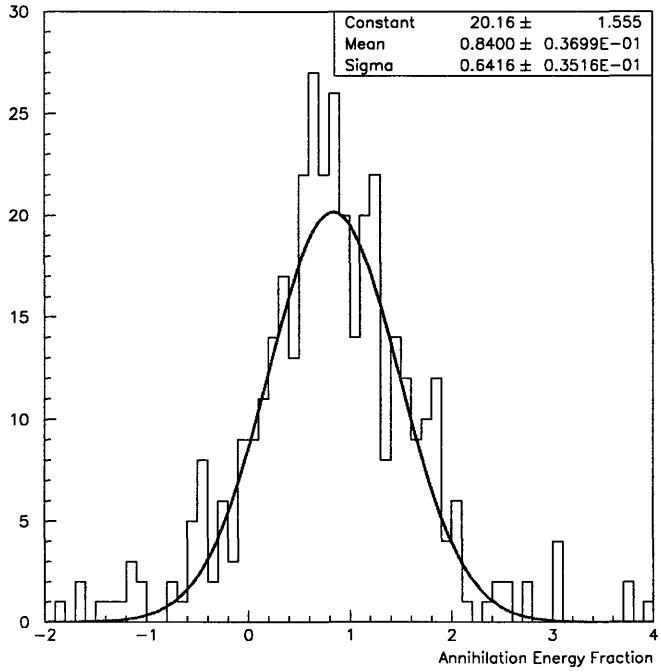

Figure 3-13: The fraction of annihilation energy seen by the calorimeter for antimatter found using Equation 3.16 on selected antiprotons.

Figure 3-13 shows the histogram of measured values for α from the selected antiprotons. The spread in the distribution is dominated by the energy resolutlion of the calorimeter. The mean of the distribution provides a value for the fraction of annihilation energy seen by the calorimeter of $(84.0 \pm 3.7)\%$.

3.4.8 Time Resolution

Time resolution for the calorimeter can be determined with tracks again. By finding the time projection of the tracks at the face of the calorimeter, the difference between the tracks and the time of the associated cluster as found by the peak tower can be histogrammed. This is shown in Figure 3-14 with a fit yielding 314 ps for the time resolution. Again, non-LET events are necessary to prevent biases caused by the LET in the calorimeter response.

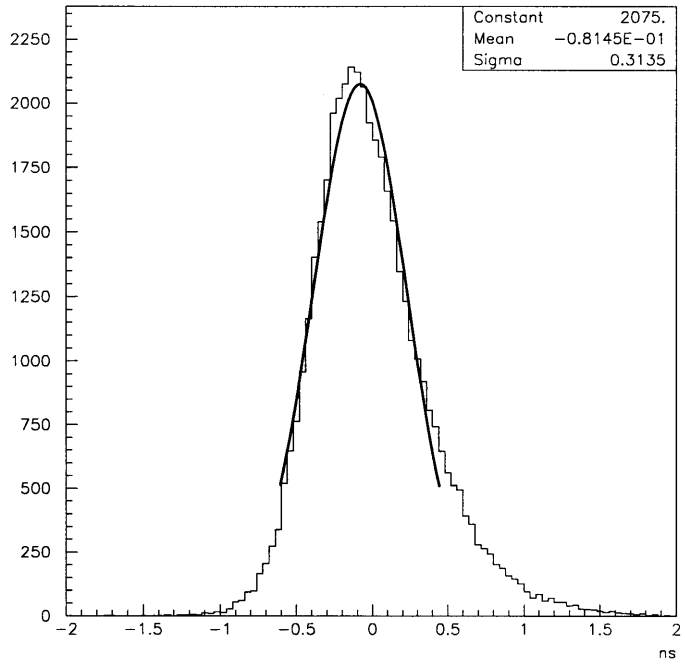

Figure 3-14: Differences between track-projected times at the calorimeter face and the time of the peak tower of the cluster associated with the track.

3.4.9 Alignment

The alignment of the calorimeter can also be checked with track projections. If the positions of the track and cluster were compared at the front face of the calorimeter, they would not agree. This is because the shower actually takes place at some depth inside the calorimeter, and because the tracks generally enter the calorimeter at some angle. It is impossible to know at what depth the track created a shower. Instead, the tracks are projected into the calorimeter to the average shower depth (along the vector of the track) of 19.7 cm [24]. The calorimeter cluster positions are found using a weighted average of the peak tower with either its horizontal or vertical neighbors as follows:

$$x_{calo} = \frac{\sum_{i=1,3} E_i \times x_i}{\sum_{i=1,3} E_i} \tag{3.17}$$

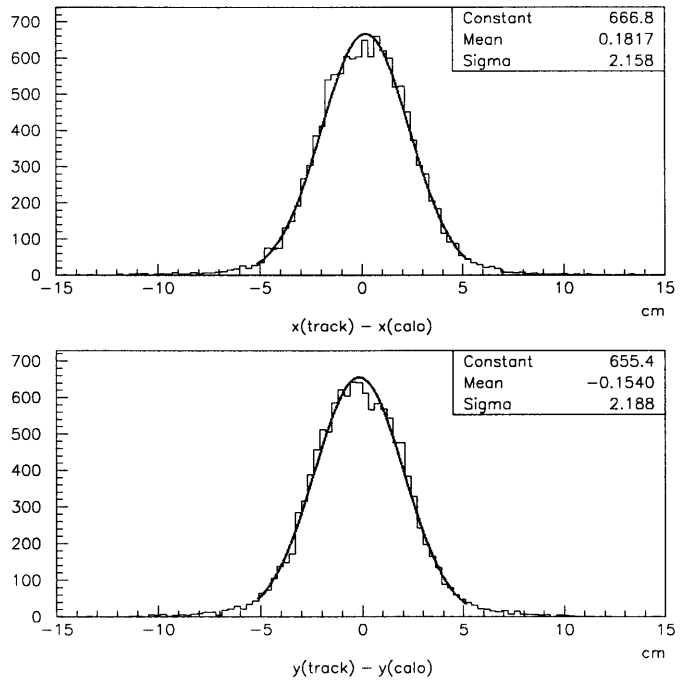

Figure 3-15: Differences between track-projected positions at the average calorimeter shower depth and the positions of the clusters associated with the tracks.

$$y_{calo} = \frac{\sum_{j=1,3} E_j \times y_i}{\sum_{j=1,3} E_j} \tag{3.18}$$

This equation is calculated using for tower positions the centroid of their front face. Because the calorimeter is rotated slightly in the x-z plane, care must be taken to project this position to the depth at which the showers occur. This depth varies on a track-to-track basis depending on the angle of the track since the shower is assumed to be located 19.7 cm along the direction of the track beyond the face of the calorimeter.

Figure 3-15 shows the difference in position between the track projections and the clusters found to be associated with the tracks. The alignment resolution appears to be in the range of 2.0-2.5 cm. The calorimeter is sufficiently aligned with the tracks in both x and y.

Chapter 4

Data and LET Summary

4.1 Data Set

During the 1996-1997 run of E864, which spanned the months of December 1996 and January 1997, approximately 287 million triggers were written to tape at the -0.75T field setting. This includes 15 million calibration triggers taken mostly before physics running. The first 47.5 million of the remaining physics run triggers exhibit unusual behavior in the Mitch beam trigger counter and will require additional study before analysis. Of the remaining 225 million triggers, about 16 million were lost due to Exabyte tapes errors and 9 million were not obtained in time for this analysis. The remaining data set includes 180 million LET triggered events, 12.9 million INT2s, and 2.8 million pedestal triggers.

For analysis, it was decided to use the Abacus computer facility at the Laboratory for Nuclear Science at MIT. This facility has a large Digital Linear Tape (DLT) robot which allows quick, convenient access to large data sets. This meant that the data set needed to be copied to DLT - a time-consuming exercise, but one that at least resulted in a backup of the entire data set. The DLT format stores approximately 20 GB of compressed data, versus $\sim$5 GB on the Exabyte tapes used by the E864 DA. The entire $\sim$2 TB of available data from physics runs was collected from over 225 Exabyte 8mm dual density tapes to just over 40 DLT tapes.

4.2 Data Summary Tapes (DST)

4.2.1 Pass I

In order to improve the speed of data analysis, a first pass was made on the calibrated physics data to produce a Data Summary Tape (DST). A method to produce the DST was chosen which retained every event in the data set, but kept only certain information from each event. The E864 analysis code framework is set up to accommodate various DST formats, and time was spent creating a format which stored the desired information, yet reduced the data size significantly. The resulting format compressed the data set by a factor of ~20 in size, and increased analysis throughput rates by a factor of >100 on the Abacus facility.

4.2.2 Pass II

A second pass on the data set was performed to select interesting events. Interesting events were defined as those which had at least one track satisfying one of the criteria in Table 4.1. No other requirements were placed on the tracks. Pass II was performed on the DST output from Pass I, and produced a reduced data set of 9.7 million events. This data set is small enough (4.6 GB) to keep on disk and can be run through in ~30 minutes.

	Requirements			Interesting
Criterion	Charge	Speed	Mass (GeV/c^2)	Physics
A	$Z \leq -2$	$\beta < 0.985$	all	Strangelets
B	$Z = -1$	$\beta < 0.985$	$M > 0.6$	$\bar{p}$, $\bar{d}$, Strangelets
C	$Z = +1$	$\beta < 0.985$	$M > 2.7$	Strangelets, (some tritons)
D	$Z = +2$	$\beta < 0.985$	$M > 2.4$	^{3}He, ^{4}He, ^{6}He, Strangelets
E	$Z \geq +3$	$\beta < 0.985$	all	^{6}Li, Strangelets

Table 4.1: Pass II event selection criteria. An event must have at least one track which satisfies one of the above criteria to be kept.

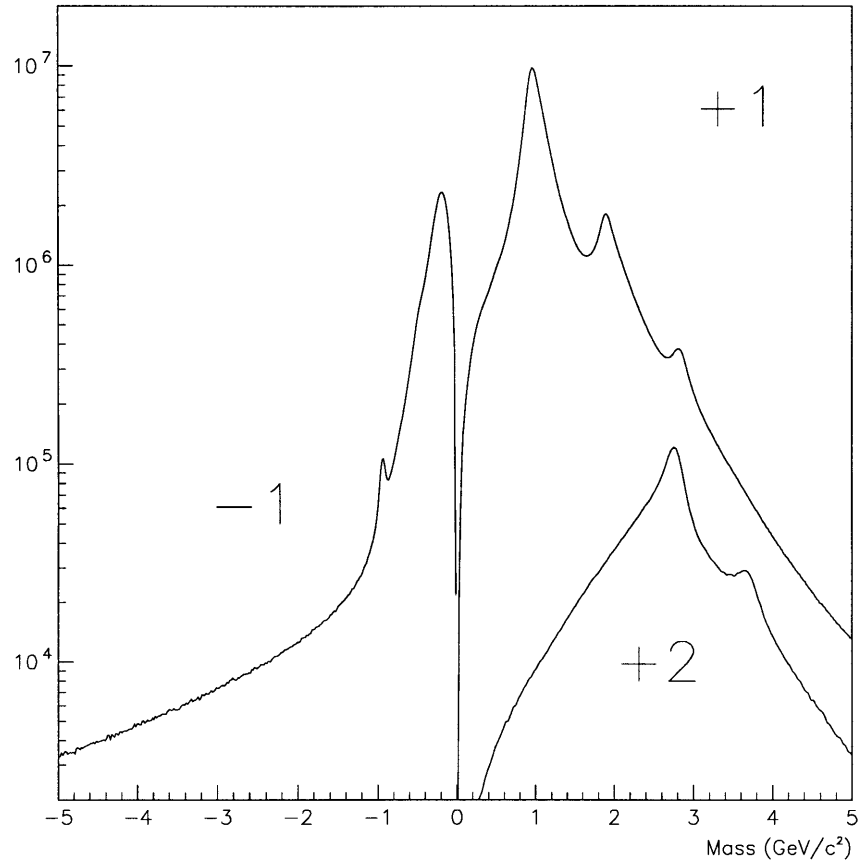

Figure 4-1: Reconstructed mass spectrum of charge -1, +1, and +2 particles in the analyzed data set. Negatively charged particles are given a negative mass. See text for discussion.

4.3 Particle Yields

Figure 4-1 provides a spectrum of reconstructed masses for particles of charge -1, +1, and +2 in the analyzed data set. Peaks are evident for antiprotons, negative pions/kaons, protons, deuterons, tritons, ^{3}He, and ^{4}He. Errors in the mass measurement come primarily from two source: errors in the reconstructed rigidity of the tracks, and errors in the calculated speed (β) of the tracks.

The first of these two error sources is the cause of significant background in Figure 4-1. Scattered particles (predominantly protons) have their rigidities recon-

structed improperly, thereby obtaining incorrect masses. The scattering is believed to occur mostly in the material of S1 and in the vacuum window immediately after M2. This background for E864 has been studied in greater detail elsewhere [26].

Smearing of the mass peak resolution arises from the second error source: β determination. The error in β is directly related to the time resolutions of the hodoscopes. However, the error in the calculated mass (δM) due to the error in β ($\delta\beta$) is as follows:

$$(\delta M)^2_{\text{fixed } P} = \left(\frac{2|\vec{P}|}{\beta^2\sqrt{1-\beta^2}} \right)^2 (\delta\beta)^2 \tag{4.1}$$

As β approaches the speed of light ($\beta \rightarrow 1$), δM blows up. This error also leads to an inability to reconstruct masses for near-speed-of-light particles whose β has been determined as greater than 1.0 because of fluctuations in the hodoscope time measurements. However, the resolution of the reconstructed mass improves for low β to the point where other error sources dominate.

Rough particle yields have been integrated from the Pass I DST. The results are shown in Table 4.2. Very loose cuts have been used on all χ^2 values, and some β cuts have been applied to reduce background and focus on the midrapidity region.

Particle Type	Yield	β Cut	Mass (GeV/c^2)	ΔM/M
Antiprotons	2.4×10^5	0.985	0.937	4.2%
Kaon$^-$	2.6×10^4	0.985	0.510	7.2%
Protons	4.8×10^7	0.985	0.971	8.0%
Deuterons	9.0×10^6	0.985	1.909	5.7%
Tritons	1.7×10^6	0.985	2.833	3.4%
^{3}He	6.0×10^5	0.985	2.756	5.0%
^{4}He	1.0×10^5	0.985	3.675	3.5%
^{6}He	60	0.971	5.545	2.7%
^{6}Li	100	0.971	5.681	3.8%

Table 4.2: Particle yields from Pass I.

4.4 LET performance

4.4.1 Rejection Factor

During each run, a PC was used to record spill totals for many quantities. These include such counts as the number of each trigger type taken to tape, the number of beams seen by each beam counter detector, and the number of triggers sampled by the LET. These scaler quantities were kept for every run and allow one to determine a rejection factor for the LET on a run-to-run basis, and on a global basis. The rejection factor represents the average number of sampled triggers in which the LET accepts only one. The number is thus calculated by dividing the total number of LET-sampled triggers in a run by the total number of LET-accepted triggers. Tables 4.3 and 4.4 enumerate these quantities for the runs analyzed in this thesis. Unfortunately, the scaler computer malfunctioned during portions of some runs, resulting in lack of spill information for large, contiguous segments of those runs.[1] Totals for the scaler quantities are shown at the bottom of Table 4.4. A global LET rejection factor is also shown as calculated from dividing all LET-sampled INT2 triggers by the toal number of LET triggers accepted and is found to be 76.7629.

Some run-to-run variation in the LET rejection factor is due to a correlation between the rejection factor and the beam rate. Using the counts in Mitch A per spill as a measure of the beam rate, Figure 4-2 demonstrates this correlation. As the beam rate increases, there is a greater chance that a second interaction (which has a small, but finite chance of passing the double beam veto logic) will occur in the target. The fast particles from these interactions will be energetic, yet have a late time relative to the timing gates set by the first interaction. The result is that more events appear to have a late, energetic candidate, increasing the percentage of events which satisfy the LET trigger. For the most part, the average beam rate for the experiment was held fairly constant over the duration of the experiment, and this effect plays only a minor roll in the run-to-run fluctuations of the rejection factor.

[1]The analyzed runs in which scaler information is missing are: 1191, 1197, 1320, 1325, 1330, 1335, 1337, and 1341.

Run #	Spills	LET Triggers	Sampled INT2s	Rejection
1190	807	866858	71333281	82.28947
1194	1868	2354693	155798574	66.16513
1195	5007	5028465	370977095	73.77541
1196	7991	7723852	579204649	74.98910
1199	1110	821670	66509072	80.94378
1200	4709	3829900	313566139	81.87319
1201	4610	4891316	408631159	83.54218
1202	1864	1740027	155602233	89.42519
1204	1239	925947	98490049	106.3668
1205	3889	4366182	363848336	83.33329
1217	1497	1512984	125315860	82.82695
1218	7713	7599938	653001334	85.92193
1219	892	936822	82746935	88.32728
1220	9340	7100978	671536966	94.56964
1221	9325	9477380	607853206	64.13726
1222	1852	2183538	129838529	59.46246
1223	2564	2071072	121846124	58.83240
1225	3118	4004982	210456270	52.54862
1226	5811	5801745	481680922	83.02346
1318	4931	5231061	412286543	78.81509
1319	4185	4215920	331934650	78.73362
1321	9915	8260940	799565233	96.78865
1323	4534	4364015	343985617	78.82320
1324	4455	5483259	381051999	69.49371
1326	7671	8503867	682440873	80.25066
1327	7320	8654861	617423976	71.33841
1328	7334	8684306	605042397	69.67078
1329	2931	3101277	236172244	76.15322
1331	5119	5048139	422138801	83.62266
1332	4764	4520380	435478014	96.33659
1333	4526	4875654	366668883	75.20404
1334	1355	1765045	117357695	66.48991

Table 4.3: Scaler data for LET rejection. Only runs with complete scaler information are included. Additionally, not all events included in the scalers were retrievable from the Exabyte tapes.

Run #	Spills	LET Triggers	Sampled INT2s	Rejection
1336	722	835386	65693796	78.63885
1338	5283	6352487	479442802	75.47324
1340	2980	2280919	173121457	75.89987
1342	8600	8384890	649704019	77.48509
1343	1406	1173767	108439858	92.38618
1344	3894	3207760	285685596	89.06078
1345	5319	4607143	404982288	87.90313
1347	6842	6410515	526150513	82.07617
1350	882	800733	72690476	90.77992
Totals	213711	213829808	16414181376	76.7629

Table 4.4: Scaler data for LET rejection (continued).

A second source of variance in the rejection was an unfortunate temperature-related time shift in the electronic gates for the experiment. The shift was found to be induced in pre-trigger electronics which take the signals from the beam trigger counters and creates a global gate for the experiment, not in the beam counters themselves. During analysis, the timing of the gates is inconsequential (so long as the ADCs and TDCs are active and armed over the appropriate periods to acquire the signals) as all times are found relative to the beam trigger counters, thereby subtracting the gate times. However, the gate timing is very important during LET running for the online measurement of the time-of-flight of particles striking the calorimeter. If the gate comes early, then all particles appear to be arriving at the calorimeter later than they should be. This is equivalent to shifting the LET curve earlier in time and accepting more fast, energetic particles in the trigger, degrading the rejection factor.

Efforts were made during the run to modify the LET curves (in time only) to account for the gate shifts, but it was not possible to provide continuous correction. During the 1998 runs of the experiment, additional electronics were installed to monitor and adjust the gate timing on the fly.

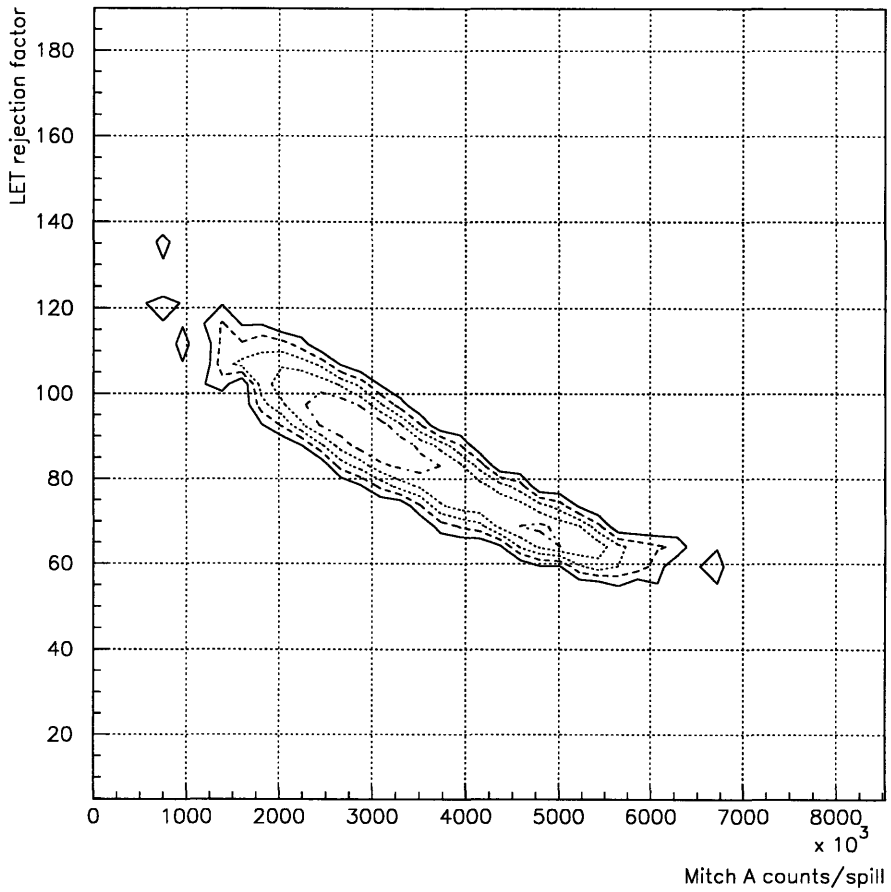

Figure 4-2: Contour plot of the LET rejection factor as a function of the counts in Mitch A on a spill-to-spill basis. A correlation between the rate in Mitch A and the LET rejection is evident.

4.4.2 LET Curves

LET curves define the energy cut-off as a function of time for hits in the calorimeter as described in Section 2.6. Calorimeter towers which register an energy above the curve for a given time are accepted for the trigger. The energy and time resolutions of the calorimeter smear the ideal curves shown in Figure 2-22 significantly. Additionally, since the LET can only gauge the energy of the shower from the response of individual towers, it is typically unable to "see" the total energy of the shower. In Figure 4-3 the energy and time resolutions of the tower with the peak energy in the calorimeter

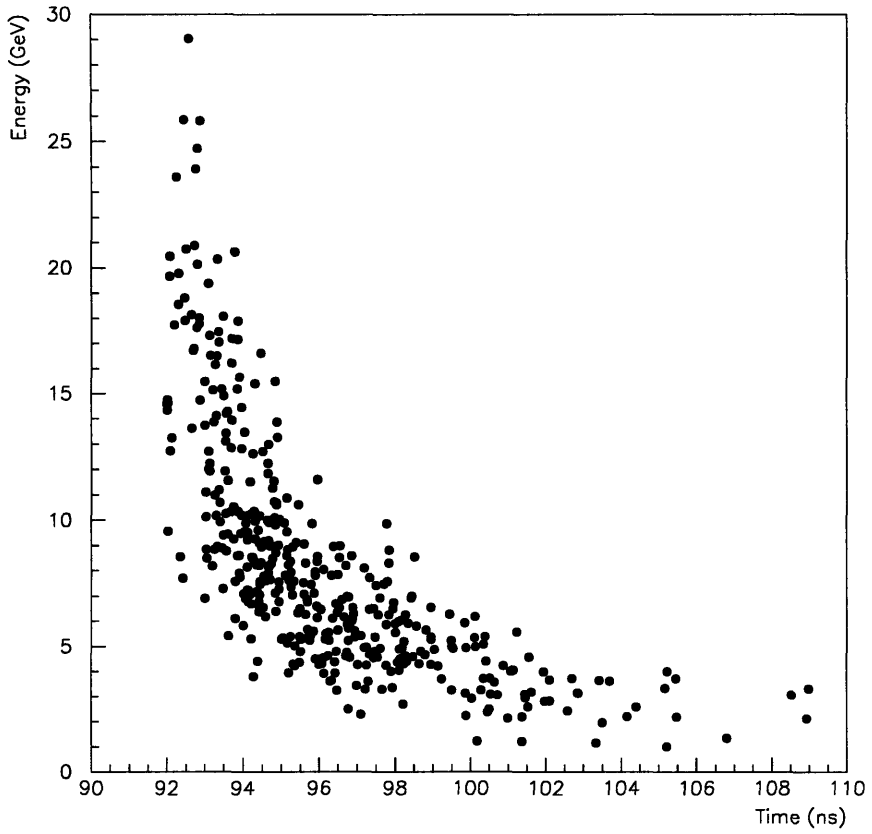

Figure 4-3: Monte Carlo simulated response of the peak tower from calorimeter showers for a mass 5A, charge -1 strangelet.

shower have been simulated for the response to mass 5A, charge -1 strangelets. If the LET curve is set up to reject a significant portion of the uninteresting events, then it cannot be set low enough to be 100% efficient for such strangelets. However such simulations allow an LET curve to be chosen which retains some desired efficiency for strangelets, antideuterons, or any other desired particle species, without placing the curve too low.

Strangelets are not expected to populate the calorimeter in the same manner as antideuterons or antiprotons. Uninteresting particles also tend to populate the calorimeter differently. The LET architecture features the ability to set LET curves individually for the fiducial calorimeter towers in order to compensate for varying

gains. This feature has the added advantage of permitting the LET curve to be optimized for different particle species and different backgrounds in different regions of the calorimeter.

For this experiment, the calorimeter is divided into four regions: one for strangelets near the neutral line where background is significant; one for strangelets near the neutral line where background is lower; one for strangelets and antideuterons away from the neutral line; and one for antiprotons which bend sharply to the outer edge of the calorimeter. In each region, the following method is used to determine the applied curve:

- Minimum and maximum time-of-flights are chosen beyond which nothing is accepted in the trigger. This is essentially a midrapidity cut.
- A particle species $\mathcal{S}$ is chosen for which to optimize the curve.
- An efficiency η is chosen for the acceptance of species $\mathcal{S}$.
- A Monte Carlo is performed simulating the response of the calorimeter to the selected particle species, providing an energy distribution as a function of time for the peak tower of the calorimeter shower.
- For each bin in time (0.25 ns wide - this is the resolution of the LET time digitization), an energy is found as a cut-off such that a fraction η of the particles of species $\mathcal{S}$ are above the cut-off.
- A minimum energy cut-off is applied regardless of the efficiency to keep the curve above background noise.

Table 4.5 describes the regions chosen and the parameters selected for setting the LET curve. The four calorimeter regions can be seen geometrically in Figure 4-4. Tables 4.6 and 4.7 list the values determined for the energy cut-offs as a function of time bin for each of the four curves to achieve the desired efficiencies.

Real data can be examined to see how accurately the intended LET curve worked in the trigger. By examining the energy and time response of calorimeter towers

Region	Columns	Rows	TOF_{min} (ns)	TOF_{max} (ns)	Species (Efficiency)	E_{min} (GeV)
A	2-25	7-12	95.0	119.5	Strangelet (60%)	2.50
B	2-25	2-6	94.5	119.5	Strangelet (80%)	1.75
C	26-42	2-12	94.5	119.5	Antideuteron (80%)	1.75
D	43-57	2-12	95.0	119.5	Antiproton (60%)	1.50

Table 4.5: Parameters for LET curves in different regions of the calorimeter. The outer rows and columns of the calorimeter are not in the LET trigger. For the strangelet, a neural, mass 5A simulation is used.

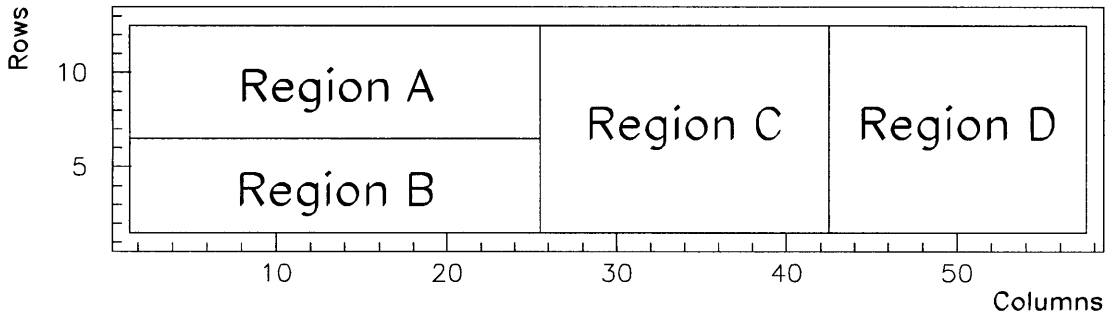

Figure 4-4: Geometric layout of the four LET regions selected in the calorimeter.

which fired the LET, a cut-off energy can be determined for each LET time bin from the rising edge of the energy profile. An example of this is shown in Figure 4-5. The entire LET curves in all four regions can be reconstructed this way and are presented in Figure 4-6. The Pass II DST data set is used for this study.

Tables 4.6 and 4.7 also show the values for the LET curves obtained from the real data. It is apparent that there is a time shift from the intended curve to the measured curve. This is believed to be due primarily to the gate-shifting effect described earlier. Despite the corrections which were made to the LET curve during the run to compensate for the shifts, there remains an effective overall shift of ~0.5 ns earlier in time. This shift will improve the efficiencies of the LET curves at high rapidities where the intended curves had no acceptance, but will not significantly change the efficiencies at midrapidity. Regardless, the measured LET curve should be used in any calculations of the LET trigger efficiency for any particular species.

Time bin (ns)	Set Energy Cut-off (measured) (GeV)			
	Region A	Region B	Region C	Region D
93.875	- (-)	- (-)	- (-)	- (-)
94.125	- (-)	- (7.83)	- (3.70)	- (-)
94.375	- (-)	- (7.70)	- (3.70)	- (-)
94.625	- (7.07)	8.00 (7.45)	4.00 (3.58)	- (2.58)
94.875	- (6.70)	7.60 (6.08)	3.75 (3.58)	- (2.48)
95.125	10.00 (6.46)	6.28 (5.95)	3.67 (3.46)	2.65 (2.47)
95.375	8.00 (6.45)	5.99 (5.70)	3.57 (3.45)	2.60 (2.46)
95.625	6.74 (6.32)	5.71 (5.45)	3.49 (3.33)	2.55 (2.45)
95.875	6.46 (6.07)	5.45 (5.20)	3.42 (3.22)	2.50 (2.34)
96.125	6.20 (5.82)	5.20 (4.95)	3.34 (3.21)	2.45 (2.34)
96.375	5.95 (5.57)	4.97 (4.82)	3.25 (3.08)	2.40 (2.22)
96.625	5.72 (5.45)	4.76 (4.57)	3.17 (2.96)	2.35 (2.21)
96.875	5.50 (5.20)	4.56 (4.33)	3.08 (2.84)	2.30 (2.10)
97.125	5.29 (4.96)	4.38 (4.20)	2.99 (2.71)	2.25 (2.09)
97.375	5.10 (4.95)	4.20 (4.07)	2.90 (2.71)	2.20 (2.09)
97.625	4.92 (4.71)	4.00 (3.82)	2.81 (2.58)	2.15 (1.97)
97.875	4.76 (4.57)	3.80 (3.58)	2.72 (2.47)	2.10 (1.96)
98.125	4.61 (4.45)	3.60 (3.46)	2.64 (2.46)	2.05 (1.84)
98.375	4.47 (4.32)	3.50 (3.45)	2.57 (2.34)	2.00 (1.84)
98.625	4.35 (4.20)	3.40 (3.33)	2.50 (2.34)	1.95 (1.83)
98.875	4.24 (4.08)	3.30 (3.21)	2.45 (2.33)	1.90 (1.72)
99.125	4.15 (3.96)	3.20 (3.08)	2.40 (2.23)	1.85 (1.71)
99.375	4.06 (3.95)	3.10 (2.96)	2.38 (2.23)	1.80 (1.59)
99.625	3.97 (3.84)	3.00 (2.96)	2.36 (2.23)	1.75 (1.59)
99.875	3.89 (3.82)	2.90 (2.83)	2.34 (2.22)	1.70 (1.58)
100.125	3.80 (3.70)	2.80 (2.71)	2.32 (2.22)	1.65 (1.47)
100.375	3.72 (3.59)	2.70 (2.59)	2.30 (2.21)	1.60 (1.47)
100.625	3.64 (3.58)	2.60 (2.47)	2.28 (2.21)	1.55 (1.46)

Table 4.6: LET curve values in Regions A, B, C, and D. The intended (set) curve values are shown along with the values measured from real data. An overall shift of $\sim$0.5 ns is apparent between the two. The LET does not fire for calorimeter times beyond those given in Tables 4.6 and 4.7.

Time bin (ns)	Set Energy Cut-off (measured) (GeV)			
	Region A	Region B	Region C	Region D
100.875	3.56 (3.46)	2.50 (2.46)	2.26 (2.10)	1.50 (1.46)
101.125	3.49 (3.45)	2.45 (2.45)	2.24 (2.10)	1.50 (1.46)
101.375	3.41 (3.33)	2.42 (2.34)	2.22 (2.09)	1.50 (1.46)
101.625	3.34 (3.21)	2.38 (2.34)	2.20 (2.09)	1.50 (1.46)
101.875	3.27 (3.20)	2.35 (2.23)	2.18 (2.09)	1.50 (1.46)
102.125	3.20 (3.09)	2.31 (2.22)	2.16 (2.08)	1.50 (1.46)
102.375	3.14 (3.08)	2.28 (2.22)	2.14 (1.97)	1.50 (1.46)
102.625	3.07 (2.96)	2.24 (2.21)	2.12 (1.97)	1.50 (1.46)
102.875	3.01 (2.96)	2.21 (2.21)	2.10 (1.97)	1.50 (1.46)
103.125	2.95 (2.84)	2.17 (2.09)	2.08 (1.96)	1.50 (1.46)
103.375	2.90 (2.70)	2.14 (2.09)	2.06 (1.96)	1.50 (1.46)
103.625	2.80 (2.70)	2.10 (2.08)	2.04 (1.96)	1.50 (1.46)
103.875	2.70 (2.58)	2.07 (1.97)	2.02 (1.85)	1.50 (1.46)
104.125	2.60 (2.47)	2.03 (1.97)	2.00 (1.85)	1.50 (1.46)
104.375	2.55 (2.46)	2.00 (1.96)	1.98 (1.85)	1.50 (1.46)
104.625	2.50 (2.46)	1.96 (1.85)	1.96 (1.84)	1.50 (1.46)
104.875	2.50 (2.46)	1.93 (1.84)	1.94 (1.83)	1.50 (1.46)
105.125	2.50 (2.46)	1.89 (1.84)	1.92 (1.83)	1.50 (1.46)
105.375	2.50 (2.46)	1.89 (1.72)	1.90 (1.73)	1.50 (1.46)
105.625	2.50 (2.46)	1.82 (1.72)	1.88 (1.73)	1.50 (1.46)
105.875	2.50 (2.46)	1.79 (1.72)	1.86 (1.73)	1.50 (1.46)
106.125	2.50 (2.46)	1.75 (1.72)	1.84 (1.73)	1.50 (1.46)
106.375	2.50 (2.46)	1.75 (1.72)	1.82 (1.72)	1.50 (1.46)
106.625	2.50 (2.46)	1.75 (1.72)	1.80 (1.71)	1.50 (1.46)
106.875	2.50 (2.46)	1.75 (1.72)	1.78 (1.71)	1.50 (1.46)
107.125	2.50 (2.46)	1.75 (1.71)	1.76 (1.71)	1.50 (1.46)
107.375	2.50 (2.46)	1.75 (1.71)	1.75 (1.71)	1.50 (1.46)
...	...	...	...	...
119.125	2.50 (2.46)	1.75 (1.71)	1.75 (1.71)	1.50 (1.46)
119.375	2.50 (2.46)	1.75 (1.71)	1.75 (1.71)	1.50 (1.46)
119.625	- (-)	- (-)	- (-)	- (-)

Table 4.7: LET curve values (continued).

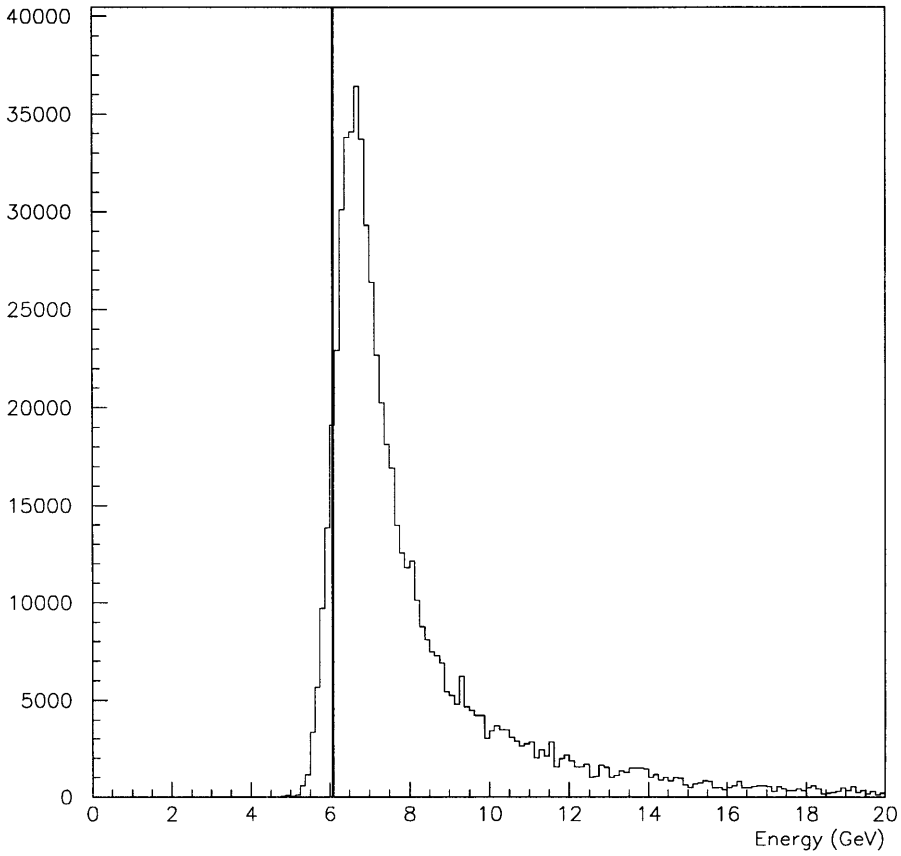

Figure 4-5: The energy deposited in the calorimeter towers in Region A in a time slice between 95.75 ns and 96.00 ns for LET-fired towers. An LET energy cut-off is determined from the rising edge.

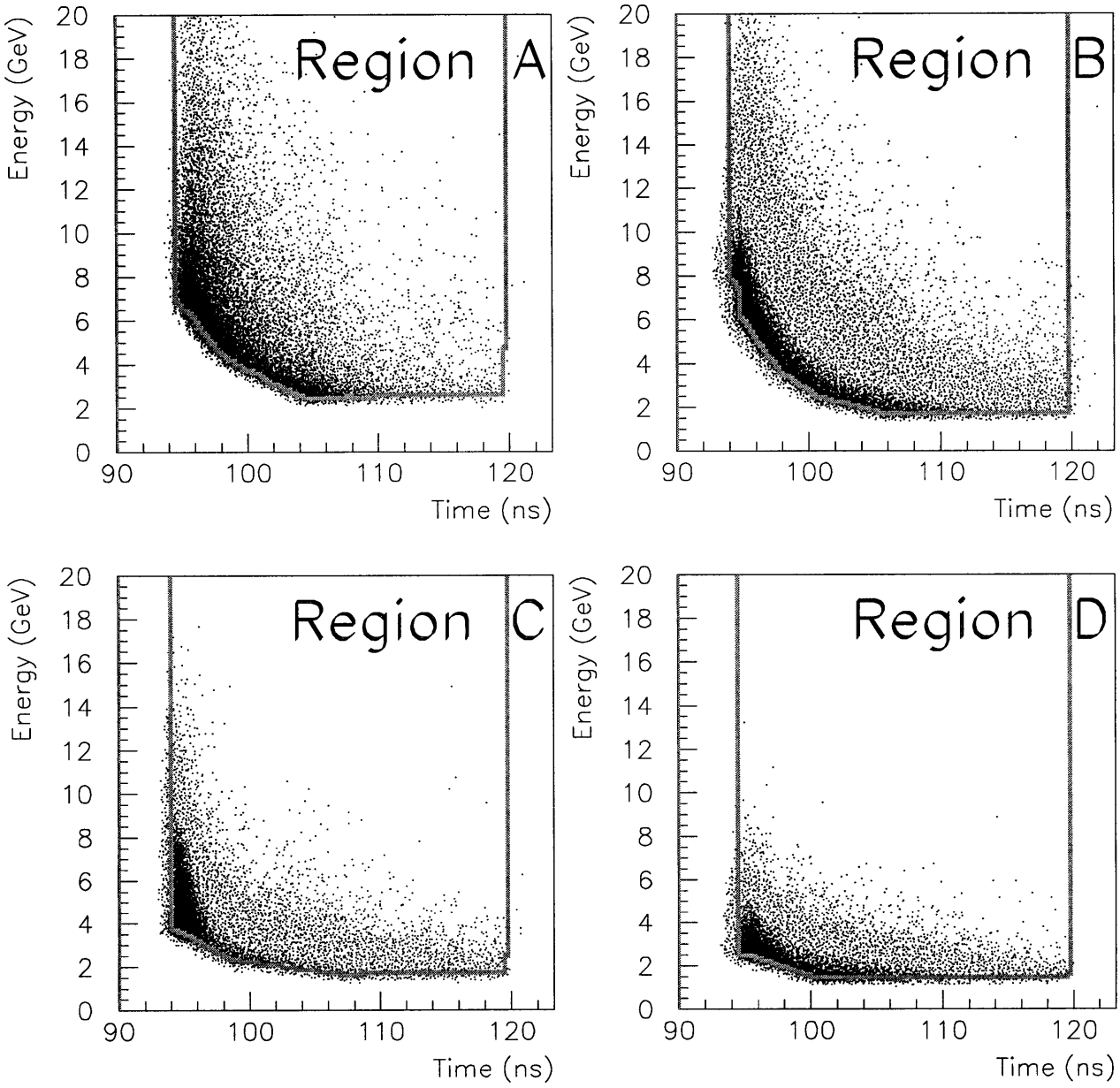

Figure 4-6: The effective LET curves shown overlapping the real data from which they were reconstructed.

Chapter 5

Analysis

The primary focus of this thesis is a search for something that has never been seen. But before looking for exotic or rare particle species in the data set, it is worthwhile to look at something previously measured to gain confidence in the data set and analysis methods. Antiprotons provide an opportunity for just such a measurement as the geometrical acceptance and LET trigger efficiency for these is expected to be relatively good compared with other species known to be produced in these collisions. The invariant multiplicity of antiprotons in similar heavy ion collisions at this energy have been studied extensively [21, 27, 28]. We will therefore first measure the invariant multiplicity of antiprotons in 10% central Au + Pt collisions at 11.6 GeV/c per nucleon.

After measuring the antiprotons, the search for negatively charged strangelets will be conducted and detailed. The analysis will include searches for charge Z = -1 and charge Z = -2 strangelets in the data set. Two strangelet production models will be used to set upper limits on the production of various strangelet masses for each charge based on the results of the searches.

5.1 Antiproton Invariant Multiplicities

The invariant multiplicity of antiprotons in heavy ion collisions can be found as a function of rapidity, $y = \tanh^{-1}(\beta_z)$, and transverse momentum, $p_t = \sqrt{p_x^2 + p_y^2}$, via

the following formulae:

$$\text{Invariant Multiplicity} = E\frac{d^3N}{dp^3} \tag{5.1}$$

$$= \frac{1}{2\pi p_t}\left(\frac{d^2N}{dy\ dp_t}\right) \tag{5.2}$$

$$= \frac{1}{2\pi \bar{p}_t}\left(\frac{N_{\text{observed}}}{\Delta y\ \Delta p_t}\right)\left(\frac{1}{\epsilon}\right) \tag{5.3}$$

In Equation 5.3, Δy and Δp_t are the width of the rapidity and p_t bins respectively, and $\bar{p}_t$ is the mean p_t for each bin. For this analysis, bins of width $\Delta y = 0.2$ and $\Delta p_t = 0.025$ GeV/c will be used. N_{observed} is the multiplicity of antiprotons in each particular y and p_t bin seen in the data set for production in 10% central Au+Pt collisions. N_{observed} is essentially the number of antiprotons seen per bin, per event. Finally, ϵ is the efficiency for seeing the antiprotons. This global efficiency includes several different efficiencies:

$$\epsilon = \epsilon_{\text{accept}} \cdot \epsilon_{\text{detect}} \cdot \epsilon_{\text{overlap}} \cdot \epsilon_{\chi^2} \tag{5.4}$$

These efficiencies are discussed below.

5.1.1 ϵ_{accept}: Geometrical Acceptance Efficiency

The acceptance for antiprotons in the experiment can be found by using Monte Carlo simulations. Antiprotons from the target can be simulated and run through the apparatus using GEANT. To be accepted, an antiproton must be capable of producing a reconstructible track in the straw and hodoscope planes.

First, we must define what is an acceptable track for reconstruction. This means defining fiducial cuts on tracks to ensure that they pass through the active regions of the detectors. Rather than placing cuts on the physical position of tracks as they pass the plane of each detector, it is simpler to look at the straight lines defined by the tracks after the spectrometer magnets to see if they are reasonable for having originated at the target, traversed the apertures of the magnets, and passed through

the active portions of all detectors.

Such requirements are especially important when considering backgrounds in real data from the experiment. Particles which are the result of some type of scattering from a source other than the target (collimators, beam pipes, vacuum chamber walls and windows, the S1 apparatus) are uninteresting for this analysis. Many of these tracks will be rejected by the χ^2 cuts, which involve cuts on the quality of the linear fits of the tracks including and excluding the target. But such cuts are not 100% efficient for the scattering background, and any tool which rejects these particles is beneficial.

Straight lines can be fit to the projections of particle tracks in the x-z and y-z planes using the points of the hits in the downstream detectors:

$$x = B_{xz} + S_{xz}z \tag{5.5}$$

$$y = B_{yz} + S_{yz}z \tag{5.6}$$

These slopes and intercepts are then used in the following cuts.

Cut on S_{xz} versus B_{xz}

In the x-z plane, the magnets bend charged particles such that the intercept of their downstream tracks (B_{xz} in Equation 5.5) is no longer at the target. However, the acceptance is rather well defined for slope as a function of intercept for these tracks. Figure 5-1 presents the distribution of slope versus intercept for the antiproton candidates and demonstrates that particles which have come through the spectrometer have limited slopes for acceptance.

For a given x intercept, scanning in slope is identical to scanning across the face of the calorimeter along the x direction. Figure 5-2 simulates such a scan in track slopes for a fixed x intercept through the spectrometer setup. The upper cut-off of the data in Figure 5-1 is essentially where the tracks reach the outermost edge of the calorimeter. Also, the last column of the calorimeter is not in the LET fiducial region. This explains the region with fewer hits at the top of Figure 5-1 before the cut-off. A

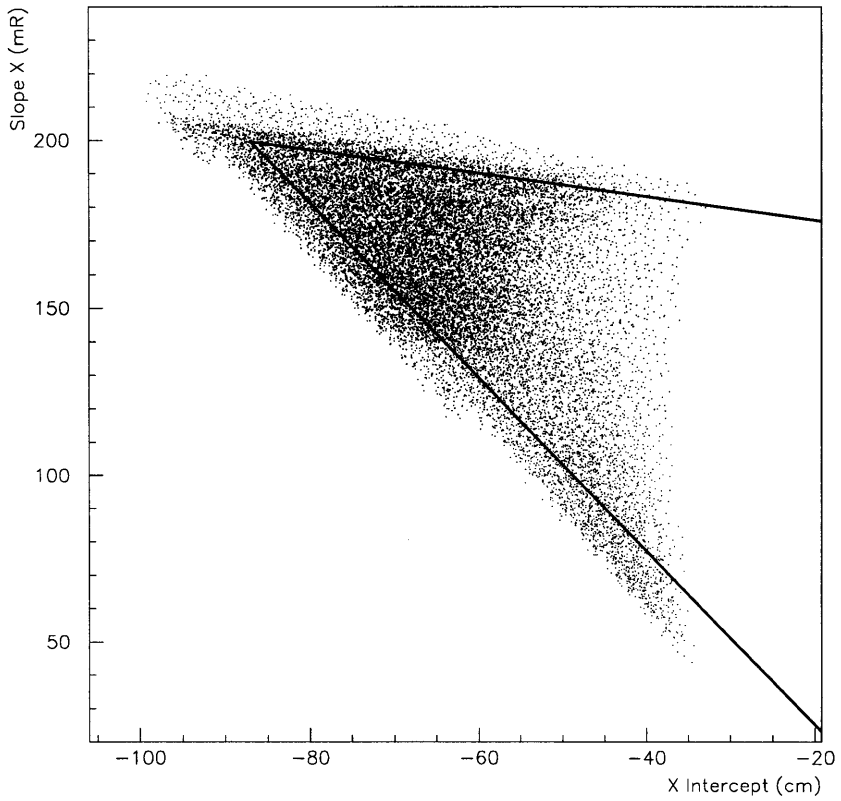

Figure 5-1: Distribution of track slopes versus intercepts in the x-z plane for antiproton candidates. The fiducial cuts are shown.

fiducial cut is thus chosen which exclude particles outside of the active LET region of the calorimeter.

The scan of slopes for a fixed intercept seen in Figure 5-2 also reveals a limit where track vectors point back into the side of the magnet, outside of the aperture. This is what leads to the drop-off on the bottom of Figure 5-1. The jagged profile of the data on this edge is due to the rigidity reconstruction program of the analysis code. The program uses a lookup table method, but extrapolates for tracks outside the table [29]. Since the table is well-defined up to the edge of the acceptance (neglecting multiple scattering), it is best to stay clear of this edge anyhow. Again, a cut is chosen which keeps particles away from this acceptance edge.

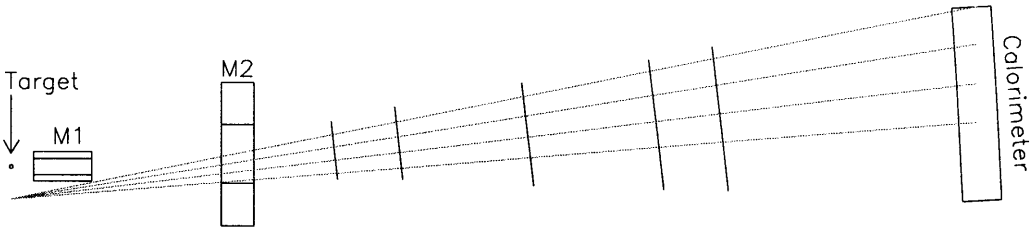

Figure 5-2: Simulated scan of track slopes in the x-z plane of the spectrometer. The slopes are limited by the edges of the calorimeter and the apertures of the magnets. In the case drawn, the intercept is at some negative x. True particles would come from the target and bend through the magnets to form these tracks.

Cut on S_{yz}

Because the magnets have very little effect on the track of the particle in the y-z plane, a simple cut on the slope S_{yz} from the fit of the downstream points using Equation 5.6 is sufficient. Figure 5-3 shows the distribution of slopes for the antiproton candidates in the data sample. The profile has several small valleys where tracks go near the cracks between calorimeter rows. For such tracks, the shower is more likely to be spread between two towers than concentrated in one. The LET is less likely to trigger on such showers, so they are suppressed in the predominantly LET-triggered data set.

The vertical experimental acceptance defined by the spectrometer magnets and plug (as shown in Figure 2-4) is between -17.5 mr and -51.3 mr. Cuts are subsequently placed at -19.0 mr and -49.0 mr to keep tracks which are not at the very edge of the acceptance. This cut also rejects tracks which pass into the upper-most and lower-most rows of the calorimeter. Particles of interest in this analysis will be required not only to enter the calorimeter, but also enter the fiducial region of the LET. Since the outer-most rows are not in the LET, the selected cuts help achieve this selection.

With the fiducial cuts in hand, the antiproton acceptances are determined through the Monte Carlo. The simulation involves most of the E864 apparatus and includes annihilation losses and multiple scattering. Antiprotons are required to pass the fidu-

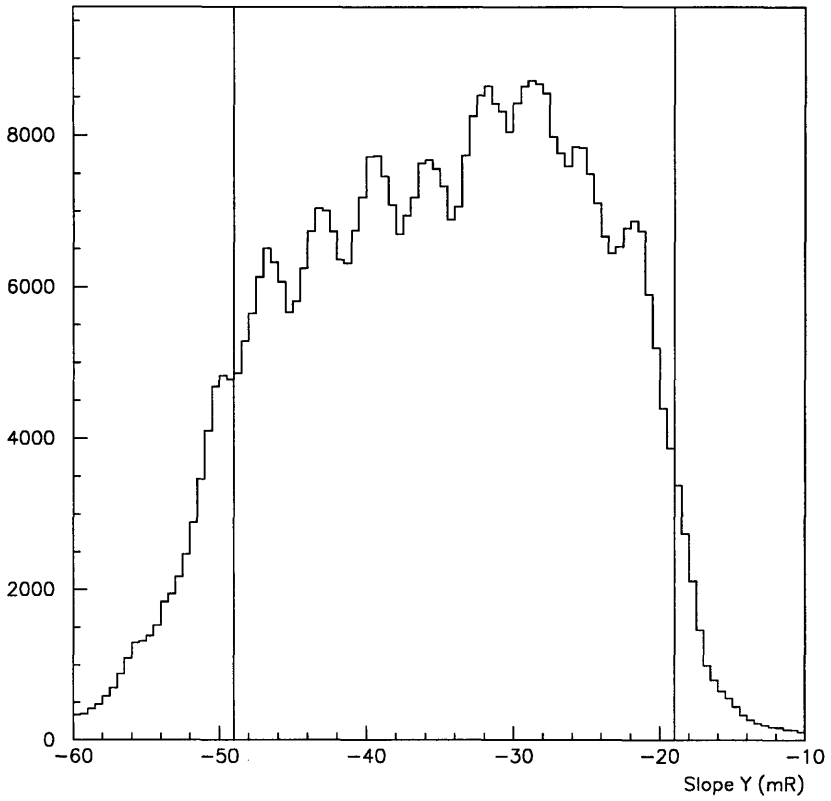

Figure 5-3: Distribution of track slopes in the y-z plane for antiproton candidates. The fiducial cuts at -19.0 and -49.0 are shown.

cial cuts and leave a hit in every detector in order to be considered for acceptance. The tracks of the antiprotons are then "faked" in the detectors of the apparatus to simulate true detector resolutions. These tracks are then run through the tracking pattern recognition to determine if they are accepted in the analysis. Detector efficiencies and tracking efficiencies are not simulated here as they will be addressed separately.

The simulated antiproton tracks are binned in y and p_t for produced and accepted tracks. Taking the ratio of the accepted tracks to the produced tracks in each bin provides the acceptance efficiency. The tracks, however, may not be reconstructed with the same y and p_t as they were produced because of multiple scattering and detector

resolutions. The error in binning due to the multiple scattering has been studied [27] and has been found to predominantly affect the p_t binning, not the y binning. Therefore, it is important that the simulated antiproton production distribution be realistic as a function of p_t.

The invariant multiplicities of antiprotons in similar collisions and over a similar range in y and p_t have been measured before and found to be relatively flat as a function of p_t. Therefore, a distribution which is constant as a function of both y and p_t has been used in the Monte Carlo simulation:

$$\frac{1}{2\pi p_t}\left(\frac{d^2N}{dy\,dp_t}\right) = \text{Constant} \tag{5.7}$$

Figure 5-4 presents the acceptance efficiencies found for each of the y and p_t bins generated. Only bins with reasonable acceptance are considered for analysis. Additionally, the levels of background are high in some bins with relatively good acceptance, preventing accurate counting of the antiproton yields. The originally intended LET curves improved the measured antiprotons for rapidities below 2.4. However, as discussed in Section 4.4.2, the effective LET curves used during the data taking came ~0.5 ns earlier than intended, improving the trigger rates for antiprotons with higher rapidities. This allows a reasonable measurement to be made in some of the bins with rapidities up to 2.6. The bins in which the invariant multiplicity will be measured are outlined.

5.1.2 ϵ_{detect}: Detector Efficiency

The detector efficiency is the probability that the apparatus sees a charged track. It is the product of the efficiency for each detector in the apparatus to register an appropriate hit for a track. The exception to this is the straw tube chambers, where only four of the six straw tube planes used in the analysis are required to have a corresponding hit for the track to be considered, as described in Section 3.3.3. The efficiencies for the individual hodoscope planes were discussed in Section 3.2.9. The

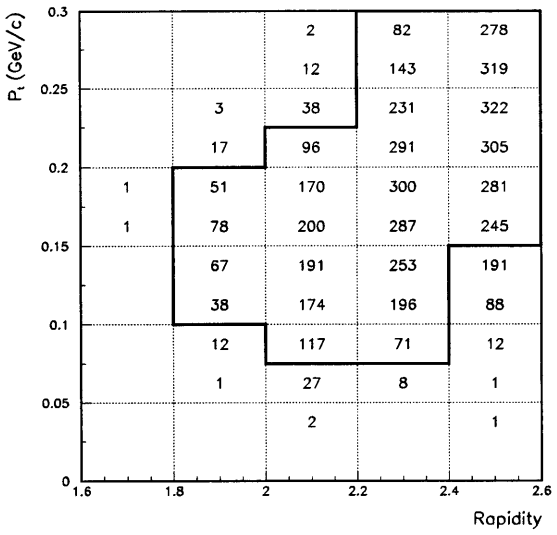

Figure 5-4: Acceptance efficiency for antiprotons. Efficiencies are in % × 10. Invariant multiplicities will be measured for the outlined region.

total detector efficiency is then

$$\begin{aligned} \epsilon_{\text{detect}} &= \epsilon_{\text{H1}} \cdot \epsilon_{\text{H2}} \cdot \epsilon_{\text{H3}} \cdot \epsilon_{\text{Straws}} \\ &= 96.8\% \cdot 96.1\% \cdot 97.8\% \cdot 100\% \\ &= 91.0\% \end{aligned} \tag{5.8}$$

5.1.3 $\epsilon_{\text{overlap}}$: Track Overlap Efficiency

The detectors in general have some occupancy during each event. This makes it possible for any interesting track to overlay an already occupied detector segment. This is not a problem in the straw chambers where clusters can be shared by different tracks in the tracking reconstruction. However, hodoscope slats which are struck by more than one particle may produce signals which render any or all of the tracks unidentifiable. If multiple tracks are indeed found to pass through a single hodoscope slat by the tracking pattern recognition routines, the chances that one of the two tracks is a ghost track is relatively high. In such cases, the track with a higher

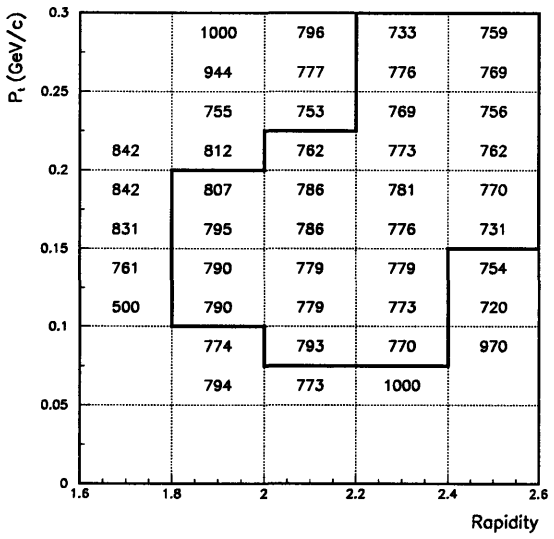

Figure 5-5: Track overlap efficiency for antiprotons. Efficiencies are in % $\times$ 10.

quality fit is kept and the other is discarded. If both should have identical fit quality, then both are discarded.

It is clear, however, that some tracks will be lost due to overlaps. To determine the efficiency for this, antiprotons can be simulated with the Monte Carlo, their responses in the detectors can be faked, and the final signals can be overlaid with those from real events. These replicated antiproton events are then passed through the standard track-finding procedures to determine whether the antiproton tracks can be found. The efficiency for finding these overlaid tracks is shown in Figure 5-5.

5.1.4 ϵ_{χ^2}: χ^2 Cut Efficiency

Once tracks have been found in events, the quality of the tracks is determined through χ^2 values from linear fits. Cuts on the quality of the tracks can then help remove background from the analysis.

χ^2_{xz}: x versus z

The portion of the track downstream of M2 should be very linear, with only the slight effects of multiple scattering preventing complete linearity. Equation 5.5 represents the linear equation used in fitting the downstream track points. With the calibrated resolutions of the detectors which have hits for the reconstructed tracks, a linear fit will return an intercept B_{xz}, a slope S_{xz}, and a χ^2 value χ^2_{xz}. H1, H2, and H3 provide x coordinates for all found tracks. In the case of the straw chambers, only four of the six straw planes are required for tracking. This means that an x coordinate may or may not be found from S2X and S3X. In the case where all straw planes record hits, there are five points fit, with two parameters in the fit, leaving three degrees of freedom.

The resultant χ^2/dof for antiprotons is shown in Figure 5-6A along with theoretical curves for χ^2 distributions with three degrees of freedomand Gaussian or square error distributions. A square error distribution is one in which the errors on the measurement are evenly distributed over a fixed, limited range of errors. No errors outside of this range occur. The measurements of the x coordinates of any single track are all taken from the physical positions of the detector elements hit, while the actual x positions of the track may be anywhere within the horizontal spans of the detector element. For the particular case of the hodoscopes, this limits the range of the position measurement error to the widths of the hit hodoscope slats. Therefore, the χ^2 distribution with square errors is expected to better fit the data.

The data follows the square error distribution very well. A cut of $\chi^2_{xz} < 3.1$ is chosen which should be 99% efficient according to the theoretical curve. The data agrees quite well with this, also resulting in 99% efficiency.

χ^2_{yz}: y versus z

The downstream portions of the tracks should also be linear in y versus z. The fit to y positions, using Equation 5.6, will return an intercept B_{yz}, a slope S_{yz}, and a χ^2_{yz}. Measurements of the y position come from all three hodoscopes, and the U and

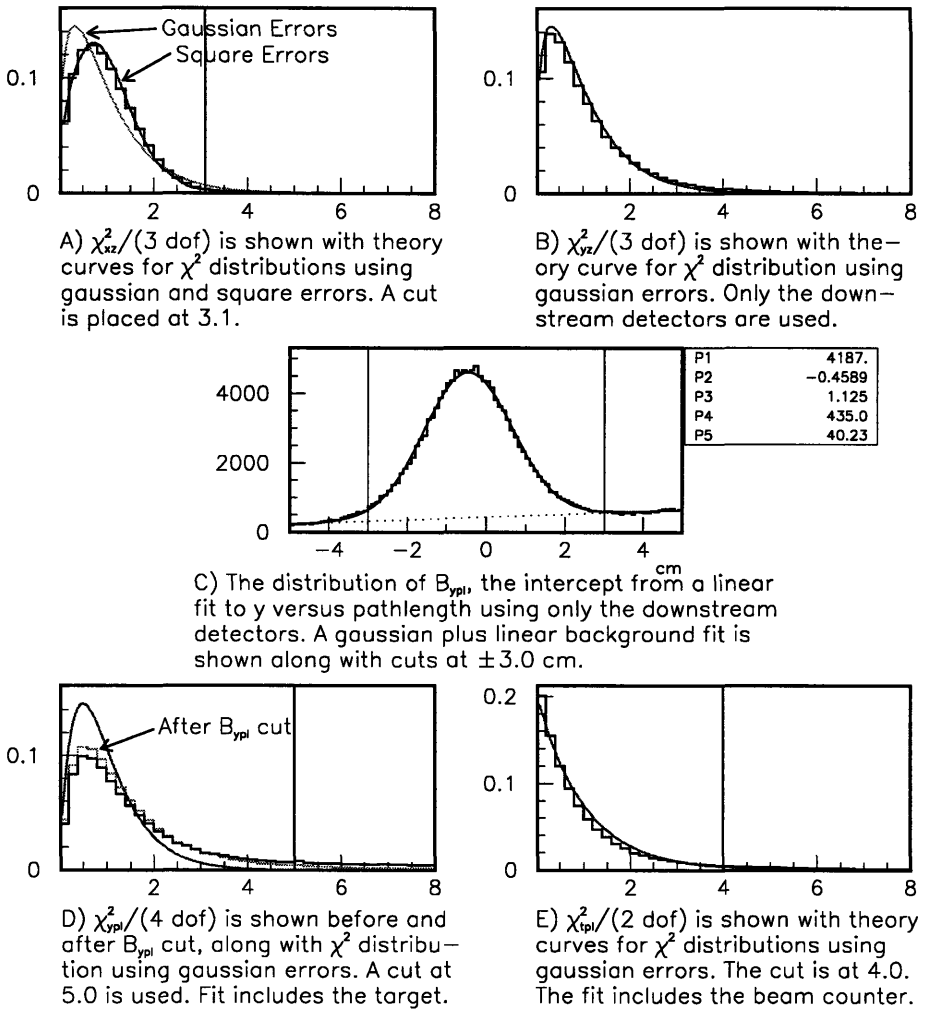

Figure 5-6: χ^2 distributions for antiprotons. Solid vertical lines show cut placement.

V straws planes at each station in combination. Again, because only four of the six straw planes are required for a track, neither or just one of the straw stations may provide a y measurement. When all six straw planes have a hit, five y measurements are made, and the linear fit has three degrees of freedom. Figure 5-6B shows the χ^2_{yz} distribution. The data and the theoretical distribution appear to agree very well here. This agreement provides confidence in the y position calibrations of the downstream detectors. No cuts are made on χ^2_{yz}.

Instead of using the z coordinates of hits, a more robust variable to use in the fitting is the pathlength $\mathcal{L}$ from the target. $\mathcal{L}$ is not simply the distance from the

target to any point in the spectrometer. It is dependent on the track in question, as it includes the distance covered along the arc through which the track passes in the magnetic fields. The strength of this variable lies in the fact that equal units of $\mathcal{L}$ should be covered in equal times for a particle of constant total momentum. The magnets of the spectrometer may change the p_x and p_z of the particle, but not the total momentum. The remaining cuts involve fits using $\mathcal{L}$.

B_{ypl}: Intercept in y versus Pathlength ($\mathcal{L}$)

The dipole magnets are not expected to change the p_y of the tracks. Therefore, a fit to y versus $\mathcal{L}$ for the hits in the downstream detectors should be linear, and should return an intercept B_{ypl} reasonably close to the target (located at the origin in the E864 coordinate system):[1]

$$y = B_{ypl} + S_{ypl}\mathcal{L} \tag{5.9}$$

The distribution of B_{ypl} from the antiprotons is shown in Figure 5-6C. The distribution seems to follow a Gaussian distribution of tracks from the target on top of a linear background. In fact, a significant source of background tracks was found to be well-identified by large B_{ypl} values. The decision was made to cut at $|B_{ypl}| < 3.0$ cm, as shown, to select tracks coming from the target.

This cut alone is 75% efficient on the antiproton candidates. However, because many of these candidates are still background, and because the antiproton counting procedure will attempt to remove this background, the efficiency for antiprotons should be determined from that portion of the distribution believed to be antiprotons. For this purpose, the Gaussian part of the fit to B_{ypl} is considered to be real antiprotons from the target. The width of this Gaussian comes in part from the beam spot size at the target, but mostly from the error on the projection of the track fit all the way back to the target. For the Gaussian in the fit to B_{ypl}, the selected cuts are

[1] Fringe fields from the magnets may cause some slight vertical bending. These fringe fields are not well-detailed in the field maps used for rigidity reconstruction. This may cause some slight displacement of the fit intercepts from the origin.

90% efficient.

It should be noted that the B_{ypl} used for this cut involves fitting Equation 5.9 to the points for the track from the downstream detectors only. An additional degree of freedom can be obtained in the fit to y versus $\mathcal{L}$ by including the target point at the origin. However, the primary purpose of the B_{ypl} cut is to remove tracks which may look fine downstream, but clearly do not come from the target. Including the target introduces a point with relatively small error and large moment in the fit, insuring that the fit looks good near the target, making the desired cut less feasible.

χ^2_{ypl}: y versus Pathlength

A cut on the linearity of the track in y versus $\mathcal{L}$ is still necessary to make sure that the track looks good through all of the detectors, not just the target. For this fit, the target is included and is given coordinates at the origin. The approximate beam spot size on the target serves as the error on the measurement of the the y position at the target. Equation 5.9 is used again for this fit, but with the additional target point. The resulting distribution of χ^2_{ypl} is shown in Figure 5-6D for antiprotons. The data appears to peak in accordance with the theoretical curve given four degrees of freedom, but the high side tail of the distribution is significantly more populated in the data. Because the χ^2_{ypl} is affected by the cut on B_{ypl}, the data distribution is shown both before and after the cut. The distribution seems to improve slightly with the B_{ypl} cut, but not completely. Any vertical bending which occurs in the magnetic field would contribute to this disagreement, along with any vertical off-centering of the beam at the target. A shift in the survey of the position of the target relative to the downstream detectors would also manifest itself in this χ^2.

A cut on $\chi^2_{ypl} < 5.0$ is selected to be more conservative here. Such a cut is 99% efficient in theory, but only 79% efficient when used on the antiproton candidates from the data. However, as this cut is not independent of the cut on B_{ypl}, the efficiency should be found after the B_{ypl} cut has been made. This leads to an efficiency of 93% for the χ^2_{ypl} cut from the data.

χ^2_{tpl}: Time (t) versus Pathlength

The hypothesis of constant total momentum is tested by a fit to the time-of-flight versus $\mathcal{L}$. "Equal units of $\mathcal{L}$ traveled in equal units of time" defines a linear relationship as follows:

$$t = B_{tpl} + S_{tpl}\mathcal{L} \tag{5.10}$$

In fact, S_{tpl} in this equation is the inverse of the velocity of the track, and the fit value is used as such in the analysis ($S_{tpl} = 1/v = 1/\beta c$).

Because the total momentum is expected to remain constant, the only deviations from linearity should be very slight contributions from multiple scattering. Time points are measured at the beam counter (which represents the time at the target) and each of the three hodoscope planes. Two degrees of freedom remain for the fit to Equation 5.10.

The distributions of the errors in time are assumed to be all Gaussian. This assumption appears to be validated by the data, shown in Figure 5-6E, as the theoretical χ^2 distribution for two degrees of freedom using Gaussian errors looks similar to the data set. However, a $\chi^2_{tpl} < 4.0$ cut, as chosen, is expected to be 98% efficient. The data shows a 90% efficiency for such a cut. The differences between the data and theory are in the tail of the distribution at high χ^2 values. The disagreement is believed to be due primarily to background tracks among the antiproton candidates. Since most of this background will be removed by the fitting procedure which will be used to count antiprotons, the actual efficiency for antiprotons should be closer to the theoretical number.

Total χ^2 Efficiency

The χ^2_{xz} and χ^2_{tpl} cuts are assumed to be independent of each other and of the B_{ypl} and χ^2_{ypl} cuts. The correlation between the latter is taken into account in the efficiency of

the χ^2_{ypl} cut. Thus, the combined efficiency of the χ^2 cuts is:

$$\begin{aligned} \epsilon_{\chi^2} &= \epsilon_{\chi^2_{xz}} \cdot \epsilon_{B_{ypl}} \cdot \epsilon_{\chi^2_{ypl}} \cdot \epsilon_{\chi^2_{tpl}} \\ &= 99\% \cdot 90\% \cdot 93\% \cdot 98\% \\ &= 81\% \end{aligned} \tag{5.11}$$

5.1.5 N_{observed}: Observed Multiplicity

To reiterate, N_{observed} is simply the number of antiprotons seen per y and p_t bin per event in the data set. The invariant multiplicity of antiprotons takes N_{observed} and corrects for efficiencies, binning, and invariance.

Antiprotons in the data set fall into one of three categories:

1. Antiprotons in INT2 events.
2. Antiprotons in LET events which fired the LET.
3. Antiprotons in LET events which did not fire the LET.

To decide if an antiproton candidate fired the LET, the track is projected to the calorimeter. With each LET event is stored the calorimeter towers which fired the LET. The 3 × 3 array of towers around the one to which the track points are then scanned for LET hits. If a hit is found, the track is assumed to have fired the LET.

The antiproton candidates in each of the three categories are divided into the selected y and p_t bins. The number of antiprotons in each bin is then counted through a fitting procedure. The fit function is a Gaussian plus a linear background around the region of the antiproton peak in mass. Some fitting examples are shown for a couple different y and p_t bins for each of the three categories in Figure 5-7. The Gaussian and linear portions of the fits are integrated separately within a $\pm 3\sigma$ region about the peak (where σ is the width of the Gaussian peak) to determine the number of antiprotons found, and the background underneath. The total numbers of antiprotons found this way for each of the three categories are shown in Figures 5-8, 5-9, and 5-10.

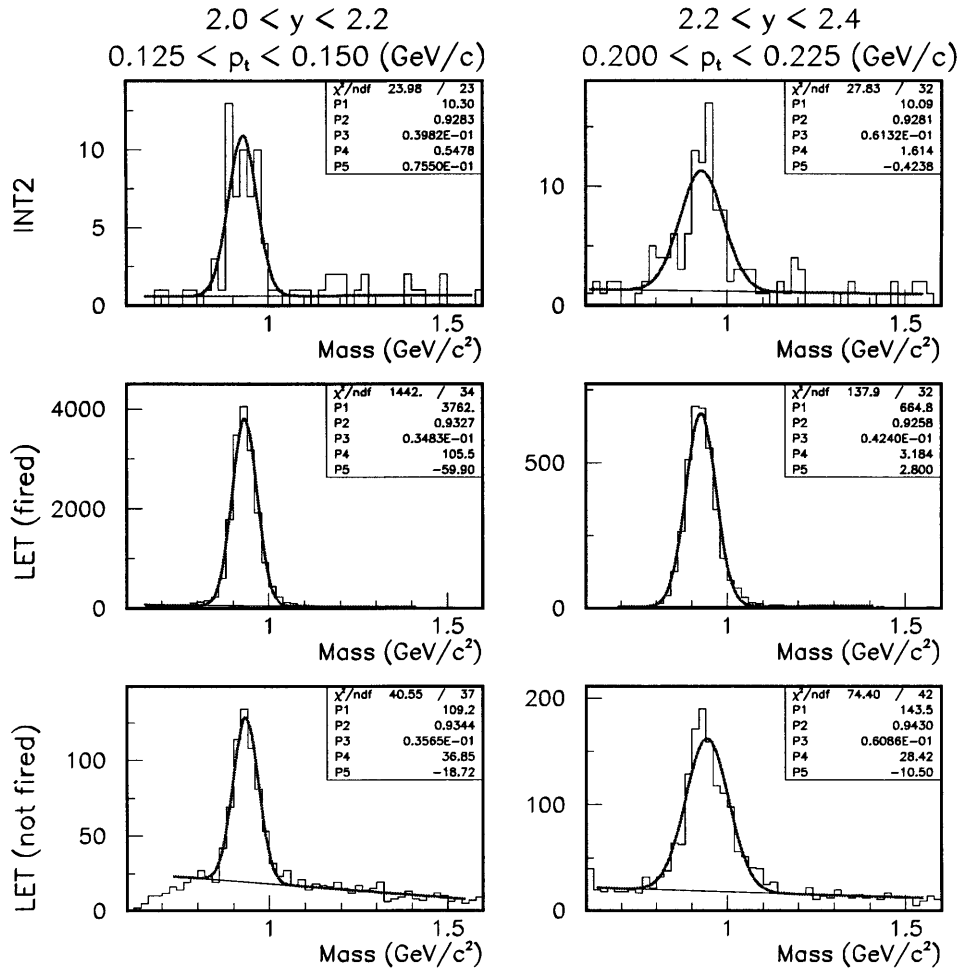

Figure 5-7: Examples of the mass distributions of antiproton candidates in two different y and p_t bins. The same bins are shown for each of the three categories of antiprotons in the data set. Also shown are the fits used to determine the number of antiprotons and background in each bin.

Given the data set from Pass II and this counting procedure, there are two ways to find the observed multiplicity N_{observed}. One method involves using the stored INT2 events in the data set. The other method involves the LET events, which offers improved statistics, but adds some complexity from biases introduced with the LET trigger.

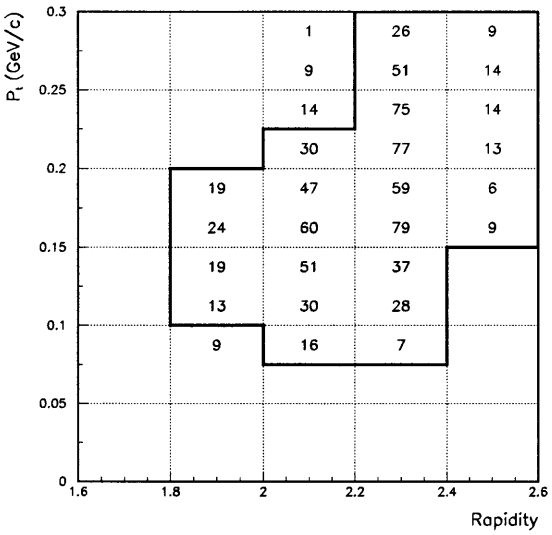

Figure 5-8: Antiprotons in INT2 events from the data set counted as a function of y and p_t.

N_{observed} for INT2 Events

The observed multiplicity can be obtained simply by looking at INT2 events. With the antiproton counts from Figure 5-8, one can find find the observed multiplicity in each y and p_t bin as follows:

$$N_{\text{observed}} = \frac{N_{\bar{p}}}{N_{\text{sampled events}}} \tag{5.12}$$

$N_{\bar{p}}$ is the number of antiprotons found in each bin, and $N_{\text{sampled events}}$ is the total number of INT2-triggered events (10% central Au+Pt interactions) in the data sample. For this analysis, there are 12.9 million INT2 events. The totals for N_{observed} per million INT2 events are shown in Figure 5-11 using statistical errors only.

N_{observed} for LET Events

The other method for determining the observed multiplicity is through the LET-triggered events. In this case, the LET trigger efficiency and rejection factor must be

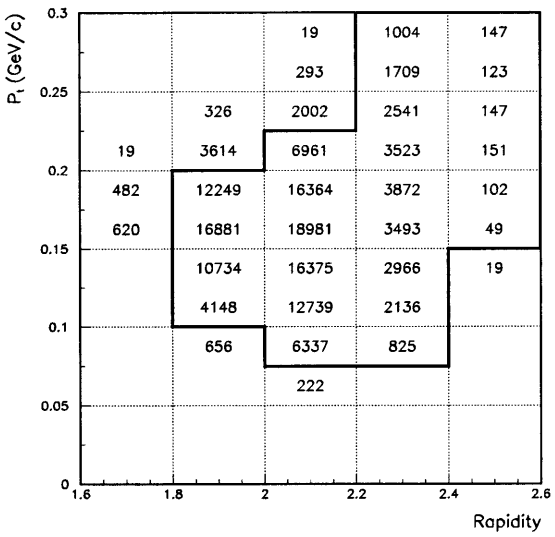

Figure 5-9: Antiprotons which fired the LET in LET-triggered events from the data set counted as a function of y and p_t.

considered:

$$N_{\text{observed}} = \frac{N_{\text{LET }\bar{\text{p}}}}{N_{\text{sampled events}}} \left(\frac{1}{\epsilon_{\text{trigger}}} \right) \tag{5.13}$$

Here, $N_{\text{LET }\bar{\text{p}}}$ is the number of antiprotons which fired the LET in LET-triggered events, and $N_{\text{sampled events}}$ is the total number of events that the LET sampled for the data set:

$$\begin{aligned} N_{\text{sampled events}} &= (\text{Rejection Factor}) \cdot (N_{\text{LET events}}) \\ &= (76.7629) \cdot (1.80 \times 10^8) \\ &= 1.38 \times 10^{10} \end{aligned} \tag{5.14}$$

At this point, there are two unknowns: N_{observed} and $\epsilon_{\text{trigger}}$. However, the number of antiprotons which did not fire the LET in LET-triggered events ($N_{\text{non-LET }\bar{\text{p}}}$) is also related to the observed multiplicity through the inefficiency of the LET trigger

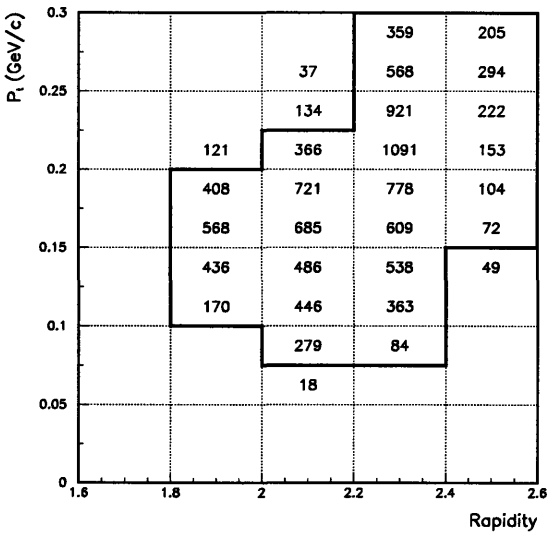

Figure 5-10: Antiprotons which did not fire the LET in LET-triggered events from the data set counted as a function of y and p_t.

$(1 - \epsilon_{\text{trigger}})$:

$$N_{\text{observed}} = \frac{N_{\text{non-LET } \bar{\text{p}}}}{N_{\text{LET events}}} \left(\frac{1}{1 - \epsilon_{\text{trigger}}} \right) \tag{5.15}$$

With two equations and two unknowns, one can solve for either unknown. Here, we focus on N_{observed}.

$$N_{\text{observed}} = \left(\frac{N_{\text{non-LET } \bar{\text{p}}}}{N_{\text{LET events}}} + \frac{N_{\text{LET } \bar{\text{p}}}}{N_{\text{sampled events}}} \right) \tag{5.16}$$

$$= \frac{1}{1.80 \times 10^8} \left(N_{\text{non-LET } \bar{\text{p}}} + \frac{N_{\text{LET } \bar{\text{p}}}}{76.7629} \right) \tag{5.17}$$

Once again, the antiprotons are counted in each y and p_t bin and N_{observed} is calculated. The values found this way are shown per million LET-sampled INT2 events in Figure 5-12. Note that the statistical errors are multiplied by 10 to make them visible.

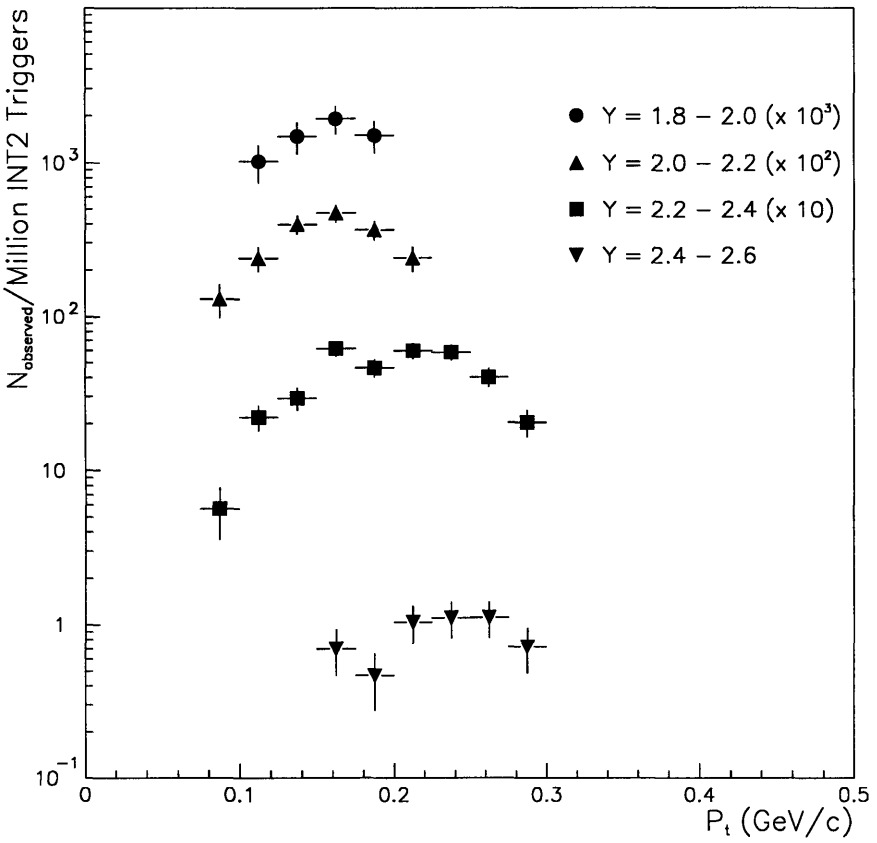

Figure 5-11: Observed multiplicity of antiprotons per million INT2-triggered events as a function of y and p_t. Only statistical errors are shown.

$\epsilon_{\text{trigger}}$: LET Trigger Efficiency for Antiprotons

Equations 5.13 and 5.15 can also be solved for the efficiency of the LET trigger:

$$\epsilon_{\text{trigger}} = \frac{1}{1 + \left(\frac{76.7629 \cdot N_{\text{non-LET } \bar{p}}}{N_{\text{LET } \bar{p}}}\right)} \tag{5.18}$$

Again, the values from Figures 5-9, and 5-10 can be used for the antiproton counts. Plugging these into Equation 5.18 results in the efficiencies found in Figure 5-13.

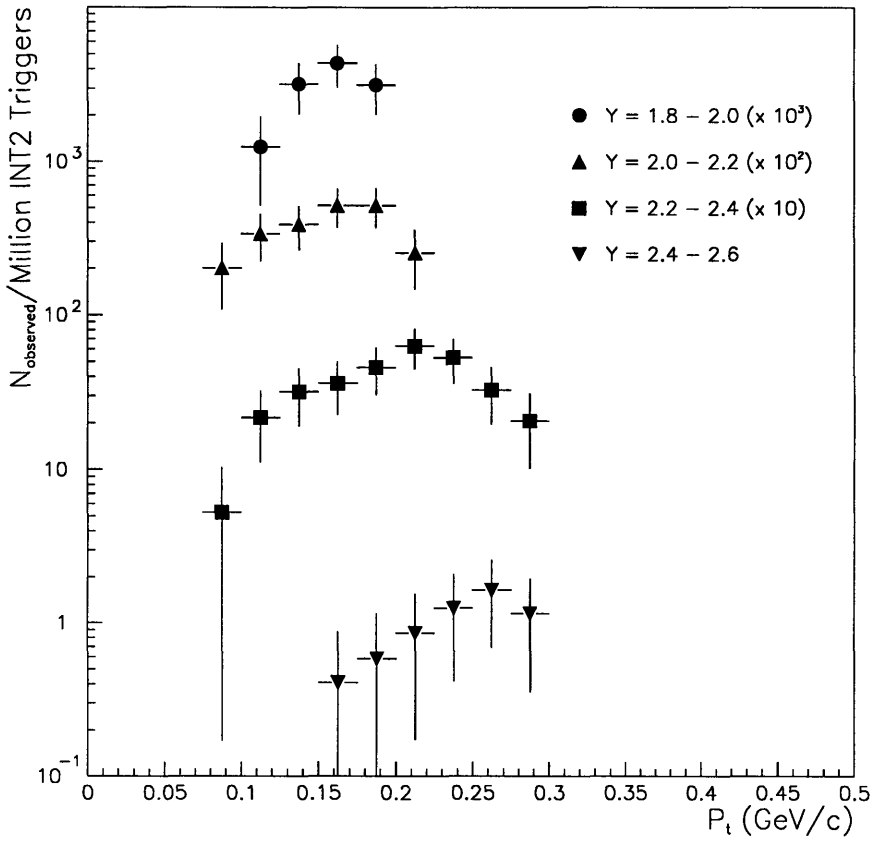

Figure 5-12: Observed multiplicity of antiprotons per million LET-sampled INT2 events as a function of y and p_t. Statistical errors are $\times 10$ to make them visible.

5.1.6 Final Invariant Multiplicities

We now have all the quantities necessary to calculate the invariant multiplicities using Equation 5.3. Because the statistics are much better for the LET-triggered events, the values for N_{observed} found in Figure 5-12 are used in the calculations.

Systematic Errors

Before going further, it is worthwhile to discuss the systematic errors of the analysis. The most dominant source of possible systematic error arises from the fitting procedure used to count antiprotons in each y and p_t bin. The fits were performed

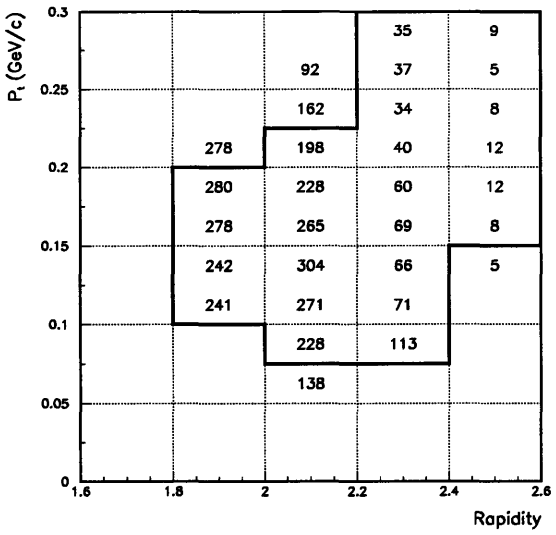

Figure 5-13: Efficiency of LET trigger for firing on antiprotons as a function of y and p_t. Efficiencies are in % $\times$ 10.

repeatedly using different ranges and different initial values for the fit parameters. The final numbers from the fits varied by no more than 10% in any of the bins of all three categories of antiprotons. A systematic error of $\pm 10\%$ is thus applied for the fitting procedure.

Next, the assumption was made that the χ^2 cuts were independent. There is reason to believe that scattered background tracks will have some correlations in χ^2, particularly between χ^2_{ypl} and χ^2_{tpl}. It is also quite possible that there is some y and p_t dependence in these efficiencies. The χ^2 efficiencies were examined for several limited ranges of y and p_t with variations of less than 5% in the determined efficiencies. This 5% is included as a systematic error from the χ^2 efficiencies.

One last source of reasonable systematic error is from the calculation of the overlap efficiencies. This efficiency is significantly influenced by the occupancies of the hodoscopes, and therefore the multiplicities of the events studied. By including an additional track in each event, the average multiplicity of each event is increased by one. Additionally, the global efficiency for finding antiprotons assumes that the χ^2 and overlap efficiencies are independent. Some of the tracks which have overlaps in

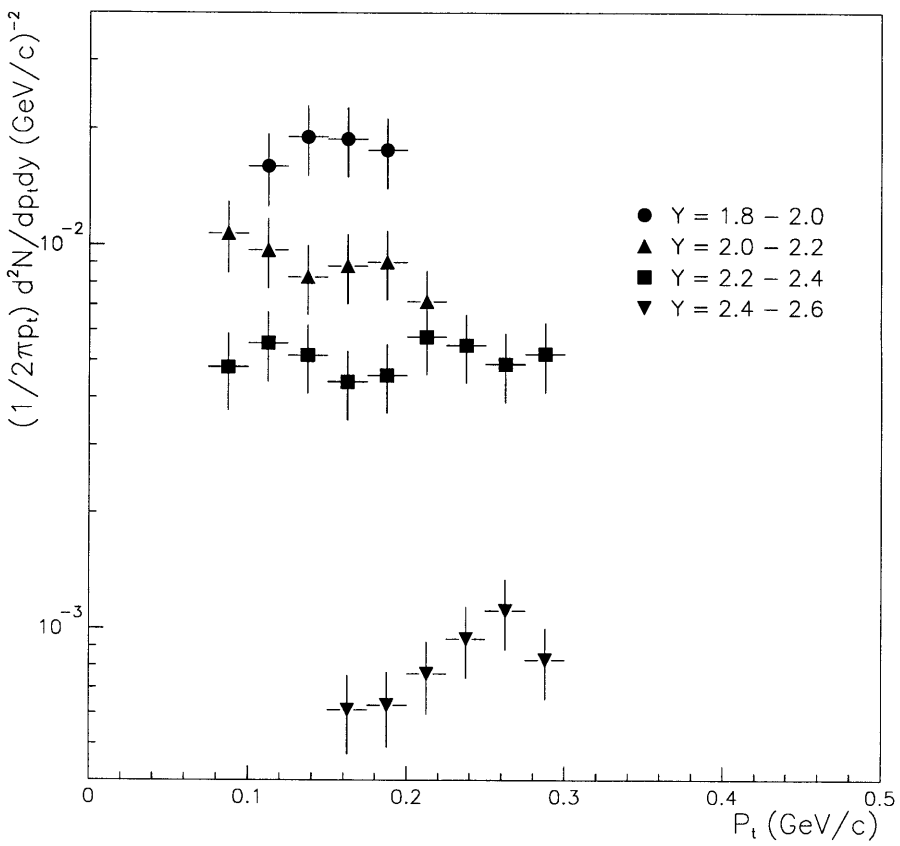

Figure 5-14: Invariant multiplicity of antiprotons in 10% central Au+Pt collisions at 11.6 A GeV/c using LET-triggered events. Errors are statistical and systematic added in quadrature.

the hodoscopes are still reconstructed, but the measurements of the time-of-flight and y position at the particular hodoscope may be off. This leads to a correlation with the χ^2 values of the tracking fits. These uncertainties lead us to estimate possible systematic errors of order 5%.

There are other possibilities for some systematic error contributions, such as the flat distribution for antiprotons assumed in the acceptance calculations, and possible biasing of antiproton multiplicities in the LET-triggered events. These uncertainties will not be considered here.

An overall systematic error of 20%, from adding the individual systematic errors

together (not in quadrature), is thus used on the antiproton invariant multiplicities. This error is combined with statistical errors from the measurements of N_{observed} and the acceptance and overlap efficiency calculations using limited Monte Carlo data sets. The final measured invariant multiplicities, with statistical and systematic errors added in quadrature are shown in Figure 5-14. The systematic errors are dominant.

5.2 Negative Strangelet Search

The foundation of E864 is its ability to search for massive, lightly charged strangelet candidates. In the data set analyzed in this thesis, the experiment has been optimized to search for candidates with a negative charge. This section will detail the search conducted for strangelets of charge Z = -1 and Z = -2. The analysis for charge -1 candidates will be described first.

5.2.1 Cuts

The primary signature for a strangelet is its high mass. This is the most obvious characteristic which distinguishes a strangelet candidate from known particles like antiprotons and negative kaons. Therefore, the focus of the search will be on the final mass spectrum of candidates. The experiment as designed affords two measurements of the mass of examined particles. Of the two, the track reconstruction process yields masses with better resolution, but is susceptible to a significant background from scattered hadrons. This makes the calorimeter a solid backup for checking that the mass from tracking is reasonable.

In order to use both systems for calculating the masses of particles, a series of requirements must be made to limit the backgrounds. These requirements can be divided into two categories:

1. Cuts made on tracking information.

2. Cuts made on calorimeter information.

We begin with a list of cuts used to reduce background in the tracking masses:

- The tracks must pass the fiducial cuts outlined in Section 5.1.1. This ensures that the candidate pass within the active portion of all detectors of the spectrometer.

- The track must bend through the spectrometer as if negatively charged.

- All three hodoscopes must indicate that the charge magnitude of the track is less than a defined minimum for charge two. This insures that the magnitude of the charge is one.

- The rapidity of the track must be <2.4. This is essentially a midrapidity cut, as the eventual time-out of the detectors during a given event serves as a minimum rapidity cut.

- χ^2 cuts are used to improve the signal-to-noise of found tracks coming from the target. The same cuts defined in Section 5.1.4 for antiprotons are used here.

- Lastly, the mass from tracking must be >5.0 GeV/c^2 to be considered a strangelet candidate.

For the calorimeter cuts, limited calorimeter information is available in the Pass II DST. But it is important to use all the information available to remove suspicious candidates. After all, given the backgrounds in tracking masses, we would not trust a strangelet candidate from tracking unless its calorimeter mass was similar, and we would not trust the calorimeter mass unless the signal was clean.

For each interesting track (as defined in Section 4.2.2), a projection was made to the face of the calorimeter to determine a struck tower. Towers immediately neighboring this struck tower were then scanned for the one with the most energy to determine the central tower of the calorimeter shower. The energies and times were saved for the towers in a 5 $\times$ 5 array about this central tower. Some calorimeter information was also stored for the tracks not labeled as interesting, but that information is not useful here.

All candidate strangelets will fall into one of the categories for interesting tracks. The 5 $\times$ 5 arrays of energy and time information are therefore always available for

these candidates. Cuts are selected which can use this information to remove candidates whose showers are likely contaminated. The cuts chosen for the calorimeter which examine the 5 × 5 arrays for the particles of interest include:

- The central tower of the shower must be a peak tower. A peak tower is defined as one with greater than 0.5 GeV of energy, and more energy than any of its immediate neighbors within the 5 × 5 array.
- No other peak towers must exist in the 5 × 5 array.
- The calorimeter time for the peak tower must be within ±2.0 ns of the projected time for the track at the face of the calorimeter. This is a rather open cut considering the time resolution of the calorimeter is well under half a nanosecond, but we want to be conservative here.
- The eight towers neighboring the peak tower must have times within ±2.5 ns of the projected track time if they have greater than 0.5 GeV of energy. This cut is wider than for the central tower because there is expected to be some propagation time for the shower into the neighboring towers.
- The position of the cluster (defined in Section 3.4.9 must be within ±7 cm of the track projected position in x and y at the track projected depth of one nuclear interaction length.
- In all 5 × 5 calorimeter arrays stored for each event, every calorimeter tower with greater than 0.5 GeV must have a valid TDC time. Such towers without valid times are signatures of double-beam events where a second interaction at the target has deposited additional, but late energy into the calorimeter on top of the showers already present.

5.2.2 Data Results

Applying all these cuts leaves a sample of 26,959 candidate tracks. The assumption is made that strangelets will deposit only their kinetic energy in the calorimeter, as

would baryons. This leads to using the following formula for determining the mass with the calorimeter:

$$M_{\text{calorimeter}} = \frac{E_{\text{calorimeter}}}{\gamma - 1} \tag{5.19}$$

The value of $E_{\text{calorimeter}}$ is found by summing the energies in the 3 $\times$ 3 array about the central tower of the calorimeter shower. γ is found from tracking.

The resulting distribution of candidates is shown in Figure 5-15. No candidates have a calorimeter mass greater than 8 GeV/c^2. But the scattering background leaves a prolific distribution of tracking masses.

At tracking masses of 10 GeV/c^2 and above, there are no candidates with calorimeter masses anywhere near the tracking mass. But at masses below 10 GeV/c^2, an agreement range between the tracking and calorimeter masses must be implemented to select viable candidates. The requirement is made that the calorimeter energy match the tracking kinetic energy within -1σ and +3σ, where σ is the energy resolution of the calorimeter as defined by Equation 3.14. Because the error on the calculation of $M_{\text{calorimeter}}$ is dominated by the error on the energy measurement of the calorimeter, the fractional error of the calorimeter mass is essentially the same as for the energy: $\sigma(M)/M \approx \sigma(E)/E$. Thus, the energy agreement requirement approximately the same as a mass agreement requirement. For the window of agreement selected, this cut is 84% efficient.

However, the calorimeter energy response is only linear up to some saturation value. Additionally, when the calorimeter energy is digitized for each tower, their is a limited range above which the ADCs overflow. Any candidates whose expected energy deposition in the calorimeter is over 30 GeV should be examined more closely for such possible effects. However, there are no candidates in the data set which approach these limitations.

This final mass agreement cut leaves a single candidate, circled in Figure 5-15, with a tracking mass of 6.90 GeV/c^2, and a calorimeter mass of 6.34 GeV/c^2. Although nothing has been found in the data to rule out that this is in fact a strangelet, the

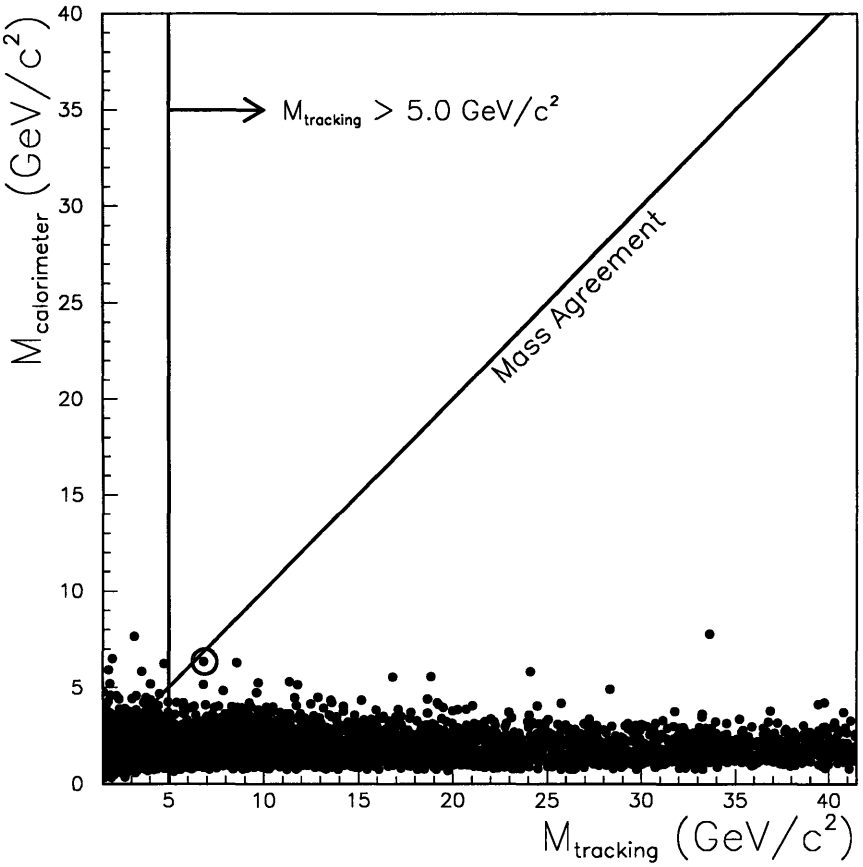

Figure 5-15: Charge -1 strangelet candidate distribution in calorimeter mass versus tracking mass. The cut at 5.0 GeV/c^2 for the minimum tracking mass is shown, as well as the line of mass agreement. The single candidate whose masses from tracking and calorimetry agree near 7 GeV/c^2 is circled.

possibility that this candidate is unreal is still quite high. There are several ways to create just such a fake strangelet candidate in the tracking, and many are listed here in no particular order:

1. An antineutron has undergone a charge exchange interaction into an antiproton in the S1 apparatus or the vacuum window.

2. A neutron has undergone a charge exchange interaction into a proton in the S1 apparatus of the vacuum window. In this case, the bending from M2 would slightly reduce the chances that such a conversion in S1 would be interpreted

as a negative track.

3. A proton or antiproton scatters very early, from the aperture wall of M1 or in S1 for example.

While all of the above are possible, the most likely explanation for this particular events appears to be that of an antineutron which has become an antiproton through charge exchange in S1 or the vacuum window. Essentially every high tracking mass, negatively charged candidate which is accepted in this analysis can be explained, on an individual basis, by the antineutron charge exchange reaction.

For the calorimeter response, the following are some of the possibilities which exist for faking a strangelet response:

1. An unusually high, but possible, fluctuation in the energy response occurs. This is more probable for an antiproton which fakes a strangelet because of the contribution from annihilation energy.

2. A slow neutron or antineutron enters the same tower as the tracked particle at a later time, depositing additional energy above that of the tracked particle.

3. A second interaction in the target has escaped detection with very little debris entering the spectrometer. However, at least one particle does enter the spectrometer and overlaps the interesting track from the first interaction at the calorimeter.

These scenarios are less probable than those which produce high mass candidates from the tracking. Additionally, it is not reasonable to expect masses greater than 10 GeV/c^2 from the calorimeter through these processes. Such reasons are why there are so many more candidates with high tracking masses than high calorimeter masses in Figure 5-15. However, the probability for each of these high calorimeter mass scenarios is nonzero for masses below 10 GeV/c^2.

Given the E864 apparatus, it appears virtually impossible to determine whether the single candidate found is indeed a strangelet. A peak of unexplained particles at a particular mass would be convincing, and such evidence was really for what the

E864 experiment was designed. Therefore, upper limits will be set assuming both the possibility that the particle is background that can be explained, and a candidate which cannot be explained.

5.2.3 Efficiencies

Before determining an upper limit, the efficiencies of the experiment for finding a strangelet candidate must be understood. The total efficiency is comprised of several different efficiencies, some of which are model dependent for the production of strangelets:

$$\epsilon = \epsilon_{\text{tracking}} \cdot \epsilon_{\text{calo}} \cdot \epsilon_{\text{trigger}} \tag{5.20}$$

$$\epsilon_{\text{tracking}} = \epsilon_{\text{accept}} \cdot \epsilon_{\text{detect}} \cdot \epsilon_{\text{overlap}} \cdot \epsilon_{\chi^2} \cdot \epsilon_{\text{charge}} \tag{5.21}$$

$$\epsilon_{\text{calo}} = \epsilon_{\text{calo cuts}} \cdot \epsilon_{\text{agree}} \tag{5.22}$$

Some of these are already known. First, the efficiency of the charge Z = 1 cut is $\epsilon_{\text{charge}} \approx 100\%$. Secondly, the efficiency ϵ_{detect} has been found in Section 5.1.2 to be 91%. Section 5.1.4 discussed the χ^2 cuts, which result in $\epsilon_{\chi^2} = 81\%$. The tracking and calorimeter mass agreement cuts (ϵ_{agree}) are 84% efficient for masses below 10 GeV/c^2, and 100% efficient above.

Production Model

All of the other efficiencies will have some dependence on the actual production distributions of the strangelets. Therefore, a production model must be assumed to study these efficiencies. The production model used here follows the form:

$$\frac{d^2N}{dy\,dp_t} \propto p_t e^{-\frac{2p_t}{<p_t>}} e^{-\frac{(y-y_{cm})^2}{2\sigma_y^2}} \tag{5.23}$$

This model separates the y and p_t components of the production. The mean transverse momentum has been chosen to be $< p_t >= 0.6\sqrt{A}$ GeV/c, where A is the mass of the strangelets in baryon number. Also, y_{cm} is midrapidity (1.6) and σ_y is the width

of the rapidity distribution. This production model and formula for $< p_t >$ has been widely used in strangelet searches and is justified elsewhere [26, 30, 27, 21, 31]. There is less certainty in the dependence of the rapidity distribution on the mass. Two previously applied models [21] will be repeated here:

Model I. $\sigma_y = 0.5$ (mass independent)

Model II. $\sigma_y = 0.5/\sqrt{A}$

Because we do not have a distribution of a candidates, calculations of each efficiency for the model as a whole, not as a function of y and p_t, are adequate. However, each of the remaining efficiencies does have some dependence on the distribution of produced strangelets, and therefore on the model applied. The efficiencies discussed below are shown in Table 5.1 for both models along with the total efficiency ϵ for observing strangelets calculated using Equations 5.20, 5.21, and 5.22, and the already discussed efficiencies. Efficiencies for the calorimeter cuts used in the charge -1 strangelet search have been determined elsewhere [21] and are also shown in Table 5.1.

Model	Strangelet Mass (GeV/c^2)	ϵ_{accept}	$\epsilon_{\text{overlap}}$	$\epsilon_{\text{calo cuts}}$	$\epsilon_{\text{trigger}}$	Total ϵ
I	5	7%	77%	52%	65%	1.1%
I	20	11%	70%	43%	83%	2.0%
I	100	11%	64%	40%	85%	1.8%
II	5	8%	79%	51%	82%	1.6%
II	20	13%	68%	37%	97%	2.3%
II	100	13%	64%	31%	99%	1.9%

Table 5.1: Various efficiencies for finding charge -1 strangelets with the E864 experiment. Strangelets of different masses produced with Models I and II are shown.

ϵ_{accept}: Acceptance Efficiency

The Monte Carlo is used to simulate the strangelets using the two production models. The acceptance is found in a similar manner to the antiprotons (see Section 5.1.1) with the ratio of total accepted strangelets to produced providing the efficiency. The

rapidity cut has also been included here, although its impact is small with the rapidity widths chosen in the two models. Table 5.1 lists the obtained values for the acceptance efficiency ϵ_{accept}.

$\epsilon_{\text{overlap}}$: Overlap Efficiency

The method for determining the overlap efficiency, $\epsilon_{\text{overlap}}$, discussed in Section 5.1.3, involves overlaying simulated strangelets with real data events. This is done for both models and shown in Table 5.1.

$\epsilon_{\text{trigger}}$: LET Trigger Efficiency

To find the LET trigger efficiency, the effective LET curves of the experiment must be applied to simulated strangelets. The effective LET curves for all four regions of the LET found in Section 4.4.2 are used here. Strangelets are produced in the Monte Carlo , and the responses of the individual detectors assuming realistic resolutions are simulated. This strangelet track is then overlaid with a real event to observe the calorimeter response. The peak tower of the calorimeter shower from the strangelet is then examined for time and energy responses. Times are used to locate an energy cut-off from the effective LET curve found for the particular region of the calorimeter in which the peak tower resides. If the energy response of the tower is above this cut-off energy, then the LET curve is considered efficient for this particular strangelet.

Because the LET curves are different for the four LET regions, each region has a different efficiency. For example, a mass 5 GeV/c^2 strangelet, using Model II, is found to have an efficiency of 52% in LET Region A, 73% in LET Region B, 92% in LET Region C, and 97% in LET Region D. But the total combined efficiency of the LET trigger $\epsilon_{\text{trigger}}$ is dependent on the distribution of the production into these different regions. The efficiency is therefore model dependent; and in the case mentioned here, using Model II, the combined efficiency of all four regions is 82%. All of the determined LET efficiencies found this way are shown in Table 5.1.

5.2.4 Final Upper Limits for Charge -1 Strangelets

With the efficiencies for observing strangelets calculated, the upper limits on the production of strangelets in 10% central Au + Pt collisions at 11.6 A GeV/c can be found with the following formula:

$$90\%\ \text{C.L.} = \frac{N_{\text{Poisson}}}{N_{\text{sampled events}}}\left(\frac{1}{\epsilon}\right) \tag{5.24}$$

$N_{\text{sampled events}}$ is the total number of 10% central interactions sampled by the LET trigger. $N_{\text{sampled events}}$ for the data set analyzed is 1.38×10^{10}. For most masses, there are no candidates. Even the single candidate found may be explainable as background. Poisson statistics indicate using $N_{\text{Poisson}} = 2.30$ in this case for the 90% confidence level on the upper limit. The final upper limits using $N_{\text{Poisson}} = 2.30$ for charge -1 strangelets are shown in Table 5.2.

Model	Strangelet Mass (GeV/c^2)	90% C.L. Upper Limit on Overall Multiplicity
I	5	1.5×10^{-8}
I	7	1.4×10^{-8}
I	20	8.3×10^{-9}
I	100	9.3×10^{-9}
II	5	1.0×10^{-8}
II	7	9.6×10^{-9}
II	20	7.3×10^{-9}
II	100	8.8×10^{-9}
I*	7	2.4×10^{-8}
II*	7	1.6×10^{-8}

Table 5.2: Final upper limits for charge -1 strangelets. The limits found for Models I and II assume no unexplained candidates. The limits found for Models I* and II* assume that the mass 7A candidate is unexplainable.

The candidate which we do have has a mass of approximately A = 7. The differences between mass 7A and the masses measured by the tracking and calorimeter are easily within their respective resolutions. The assumption that the candidate is indeed mass 7A has led to the inclusion of the upper limits for such a particle in

Table 5.2, where the upper limits have actually been interpolated between those for the mass 5A and mass 20A strangelets. If indeed the candidate is real, and not background as explained earlier, then $N_{\text{Poisson}} = 3.89$ should be used in the calculations of the 90% confidence level on the upper limits instead. The results of these upper limits for mass 7A, charge -1 strangelets in 10% central Au + Pt collisions at 11.6 A GeV/c are shown at the bottom of Table 5.2.

5.2.5 Search for Charge Z = -2 Strangelets

Similarly to the case for charge -1, Equation 5.24 will be used to determine the 90% confidence level on the upper limit for the production of charge Z = -2 strangelets. For this search, the same tracking cuts from the charge -1 search are implemented. Less background from scatters is expected in the spectrum of charge -2 than was seen in the charge -1 data, so we first look at the candidates we have after the tracking cuts without applying any of the calorimeter cuts.

The resulting candidate distribution from the search for charge -2 strangelets in calorimeter mass versus tracking mass is shown in Figure 5-16. There are no candidates with calorimeter masses greater than 3.0 GeV/c^2. There does appear to be a source of charge Z = -2 background which yields calorimeter masses below 3.0 GeV/c^2. This is believed to be a faint scattering background from ^{3}He, but has not been studied thoroughly. Regardless, our search is limited to masses greater the 5.0 GeV/c^2. In this range, no candidates have any reasonable agreement between tracking mass and calorimeter mass. We therefore need not apply any cuts other than reasonable mass agreement to improve the signal to noise in the calorimeter. A cut on a calorimeter mass within $\pm 3\sigma$ of the calorimeter's resolution for the mass from tracking is adequate and is essentially 100% efficient.[2] We will therefore set an upper limit based on a null result.

[2] A kinetic energy agreement is actually used instead of a mass agreement. Section 5.2.2 describes why these are effectively the same.

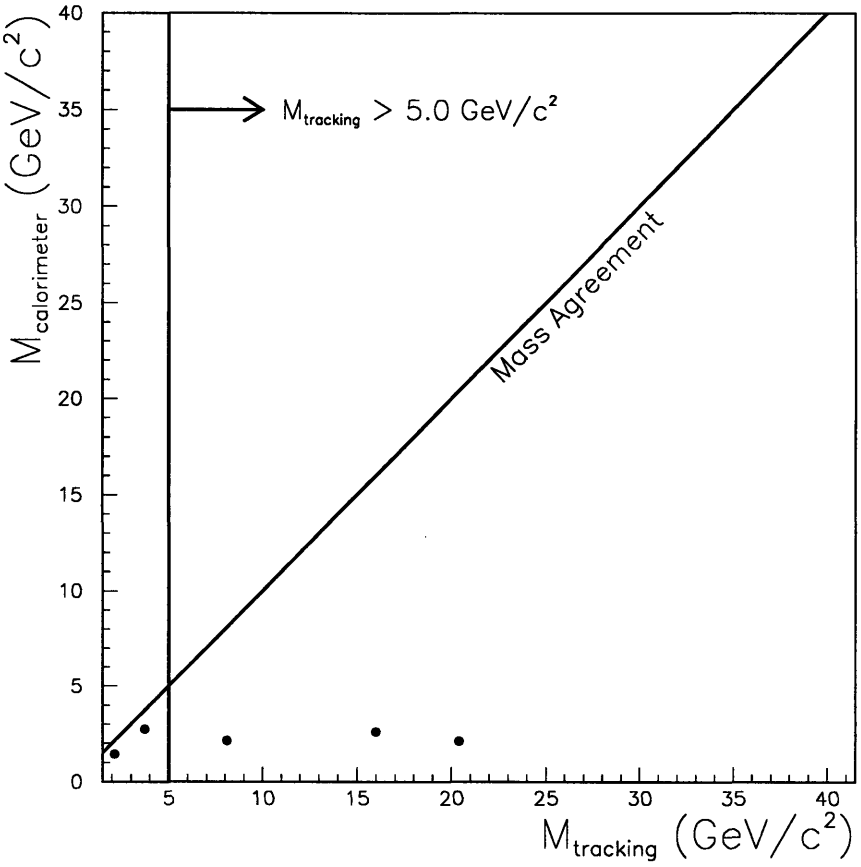

Figure 5-16: Charge -2 strangelet candidate distribution in calorimeter mass versus tracking mass. The cut at 5.0 GeV/c^2 for the minimum tracking mass is shown, as well as the line of mass agreement.

Efficiencies

The efficiencies for the charge -2 search involve the following:

$$\epsilon = \epsilon_{\text{tracking}} \cdot \epsilon_{\text{agree}} \cdot \epsilon_{\text{trigger}} \tag{5.25}$$

$$\epsilon_{\text{tracking}} = \epsilon_{\text{accept}} \cdot \epsilon_{\text{detect}} \cdot \epsilon_{\text{overlap}} \cdot \epsilon_{\chi^2} \cdot \epsilon_{\text{charge}} \tag{5.26}$$

As before, $\epsilon_{\text{detect}} = 91\%$ and $\epsilon_{\chi^2} = 81\%$. The agreement efficiency between tracking and calorimeter masses (ϵ_{agree}) is 100%. The efficiencies for acceptance (ϵ_{accept}), overlap ($\epsilon_{\text{overlap}}$), and the LET trigger ($\epsilon_{\text{trigger}}$) are all determined in the manner described

in Section 5.2.3 using strangelets from both models I and II using the Monte Carlo. The values found for these efficiencies, along with the total efficiency calculated using the efficiencies described below, are presented in Table 5.3.

Model	Strangelet Mass (GeV/c^2)	ϵ_{accept}	$\epsilon_{overlap}$	$\epsilon_{trigger}$	Total ϵ
I	5	6%	83%	82%	2.5%
I	8	8%	81%	85%	3.3%
I	20	11%	73%	97%	4.7%
I	100	11%	66%	99%	4.4%
II	5	7%	86%	96%	3.7%
II	8	10%	80%	97%	4.7%
II	20	13%	71%	99%	5.6%
II	100	13%	65%	99%	5.1%

Table 5.3: Various efficiencies for finding charge -2 strangelets with the E864 experiment. Strangelets of different masses produced with Models I and II are shown.

ϵ_{charge}: Charge Cut Efficiency

The efficiency for the charge cuts is not 100% for charge $|Z| = 2$. Some of the tracks come much closer to one end of hodoscope slats than the other, producing a much stronger signal for one of the two PMTs. This is correctable to some extent, but not when the signal causes the ADC digitizing the pulse to overflow. Additionally, some tracks pass through the hodoscopes at angles measurably different from normal, resulting in varying pathlengths in the hodoscopes which may even be cut short in a single slat by passing through the wall into a neighboring slat.

The hodoscopes are all required to see a charge $1.75 < |Z| < 2.75$ to pass the charge 2 cut. The efficiency for this cut is determined using ^{3}He, which has a unique mass-to-charge ratio of $\sim$1.4 among light nuclei. This permits a cut to be placed on using a reasonably identified Z = 2 particle species without actually using the charge 2 cut. For each ^{3}He track, the charge distribution in H1 is histogrammed while using the charge 2 cuts on H2 and H3 to insure that it is indeed a ^{3}He, and not charge 1 background. Figure 5-17 shows this charge distribution in H1 along with the cuts to

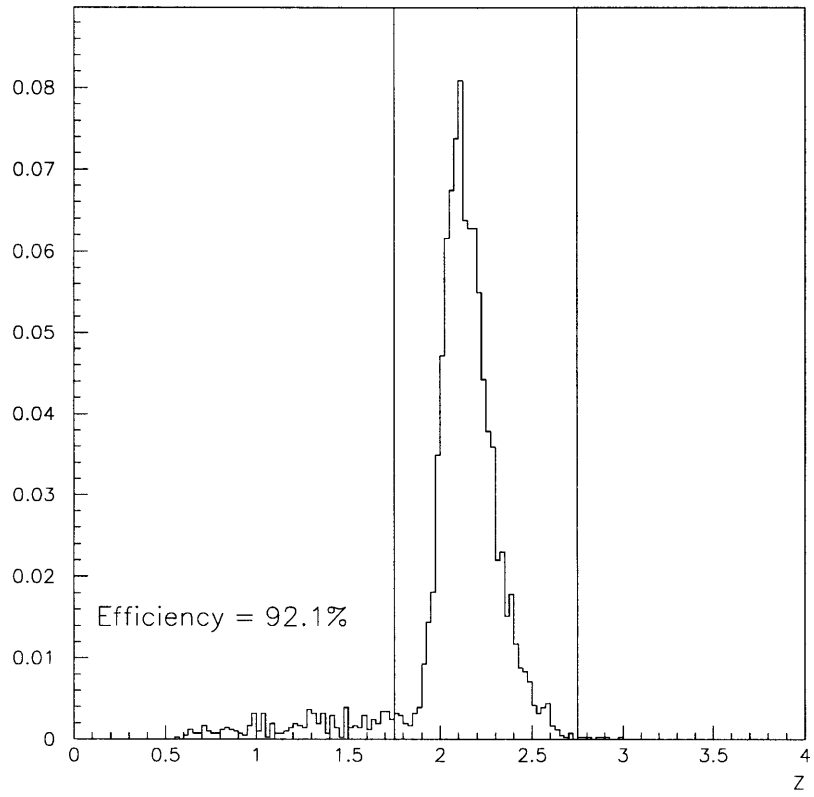

Figure 5-17: Charge distribution in H1 requiring identification of tracks as ^{3}He using only H2 and H3 for the charge. Cuts are placed at 1.75 and 2.75 for charge 2 as indicated by the vertical lines. The measured efficiency of the cuts is shown.

be placed on the charge. H2 and H3 charge distributions are histogrammed similarly using the remaining hodoscopes each time as a check to insure ^{3}He.

For each of the three hodoscopes, the efficiency of the charge 2 cut is determined by the percentage of hits in the charge distribution histogram which fall inside the range of the cut. The efficiency of the cut for each hodoscope plane should be independent, allowing an overall charge 2 cut efficiency to be calculated as follows:

$$\begin{aligned} \epsilon_{\text{charge}} &= \epsilon_{\text{H1 charge}} \cdot \epsilon_{\text{H2 charge}} \cdot \epsilon_{\text{H3 charge}} \\ &= 92.1\% \cdot 94.6\% \cdot 94.7\% \\ &= 82.5\% \end{aligned} \tag{5.27}$$

It is believed that the actual efficiency for charge Z = -2 strangelets is somewhat better than this calculation because the -0.75T field setting bends ^{3}He at sharper angles to the hodoscopes than negatively charged, massive strangelets, increasing the effect of varying pathlengths described earlier. The difference between the efficiency measured from ^{3}He and the true efficiency for strangelets is not expected to be considerable (only a few %) and is not corrected.

Final Upper Limits for Charge -2 Strangelets

The null result means that we should use $N_{\text{Poisson}} = 2.30$ in Equation 5.24. Again, 1.38×10^{10} events have been sampled for this result. The calculated 90% confidence level on the upper limits of Z = -2 strangelets produced in Au + Pt collisions at 11.6 GeV/c per nucleon are shown in Table 5.4.

Model	Strangelet Mass (GeV/c^2)	90% C.L. Upper Limit on Overall Multiplicity
I	5	6.7×10^{-9}
I	8	5.1×10^{-9}
I	20	3.5×10^{-9}
I	100	3.8×10^{-9}
II	5	4.5×10^{-9}
II	8	3.5×10^{-9}
II	20	3.0×10^{-9}
II	100	3.3×10^{-9}

Table 5.4: Final upper limits for charge -2 strangelets using Models I and II.

Chapter 6

Results

6.1 Antiproton Results

The measurement of antiproton invariant multiplicities in this thesis was intended to solidify confidence in the data set and analyses thereof. Towards this goal, we will compare our results with previously published results.

Many experiments at the AGS besides E864 have studied antiproton production in heavy ion collisions at similar energies [28, 32, 33, 34]. While performing comparisons of the results from E864 with these experiments is a worthwhile endeavor, it has been done elsewhere [27, 21, 35, 36]. Our results from the analysis contained in this thesis will therefore be examined against previous E864 antiproton invariant multiplicity measurements only.

6.1.1 Distributions of Antiproton Invariant Multiplicities

In Figure 6-1 we show the antiproton invariant multiplicities from Section 5.1.6 for 10% central Au + Pt collisions at 11.6 GeV/c per nucleon ("1996-1997 -0.75T"). The antiproton spectra have been studied previously at the same magnetic field setting of the spectrometer from the 1995 run [21]. The invariant multiplicities derived in that analysis are also shown in Figure 6-1 ("1995 -0.75T"). However, this is not the best field setting for accepting antiprotons in the spectrometer. As discussed in Section 2.1,

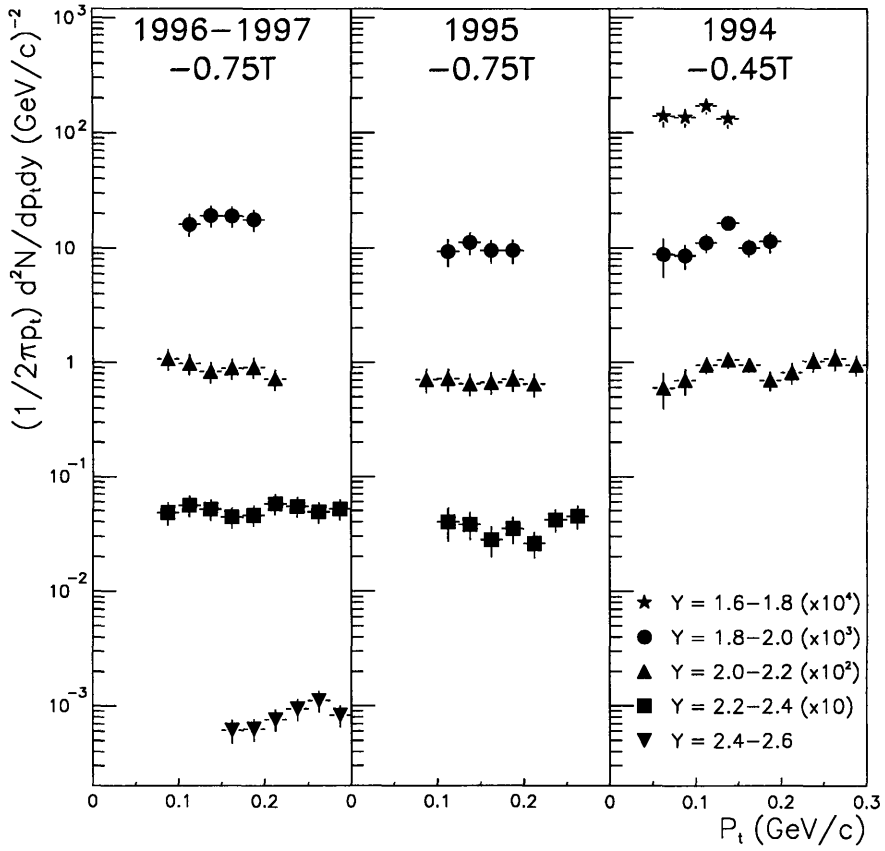

Figure 6-1: Comparison of antiproton invariant multiplicities for different E864 analyses. The data from this analysis are labeled "1996-1997 -0.75T". Errors shown are statistical and systematic added in quadrature for the 1996-1997 and 1995 data, and statistical only for the 1994 data.

the -0.45T field setting is considered optimal for the antiprotons. A thorough analysis was performed on data taken from the 1994 run at the -0.45T field setting [27, 35]. These results are plotted in Figure 6-1 as well ("1994 -0.45T").

Differences in the data sets used for these three analyses include use of the the LET trigger in the 1995 and 1996-1997 data only,[1] use of a 30% interaction length Pb target during the 1994 and 1995 runs (a 60% Pt target was used during the 1996-

[1]The calorimeter was not complete in 1994. The calorimeter and LET became operational for the 1995 run. Antiproton data at the -0.45T field setting was taken using the LET during the 1996-1997 run, but the results of the analysis on that data were not obtained in time for this thesis.

1997 running), a beam momentum of 11.5 A GeV/c in 1994 versus 11.6 A GeV/c for later runs, and the introduction of the S1 apparatus between the two dipole magnets of the spectrometer for the 1996-1997 run only. While any of these differences may introduce some biases in the data, the differences are expected to be small. We will not attempt to determine any physics differences between the data sets here. We simply want to see if our results are in reasonable agreement with the earlier E864 data. All three analyses focused on the 10% most central interactions.

Relative to the 1995 results, the data from the 1996-1997 data appear to be generally high. This is especially so for the points in the lowest rapidity bins. In other rapidity bins, agreement appears to be within one standard deviation of errors. The improved statistics on the 1996-1997 data, and time shifting of the LET trigger curves (see Section 4.4.2) has allowed new measurements to be feasible at rapidities between 2.4 and 2.6 which were not available from the 1995 data analysis at -0.75T.

Where comparable, the 1994 data seems to match the 1996-1997 data slightly better. With the lower field setting, antiprotons with lower rapidities are admitted into the acceptance. This data was taken without the aid of the LET in selecting interesting 10% central collisions from Au + Pb. Figure 6-1 confirms that the current data is in reasonable agreement with the earlier E864 data.

6.1.2 Rapidity Widths of Antiproton Production

We have no direct comparisons available for invariant multiplicity distributions in our highest rapidity bins. However, another gauge af the data is the rapidity distribution of invariant multiplicities at $p_t = 0$. Finding these values requires some assumption about the shape of the invariant multiplicity distribution as a function of p_t. If we believe that the production of antiprotons follows a Boltzmann distribution, then the p_t dependence of the invariant multiplicity should have the following form:

$$\frac{d^2N}{dy\,dp_t} \propto M_t e^{-\frac{M_t}{T_B}} \tag{6.1}$$

$$M_t = \sqrt{{p_t}^2 + M_{\bar{p}}^2} \tag{6.2}$$

M_t is referred to as the transverse mass, and T_B is the Boltzmann temperature, assuming thermal equilibrium for the production of particle species. The antiprotons presented in this analysis range in p_t from 75 MeV/c to 300 MeV/c. It has been suggested that the shape of the antiproton spectra indicate a Boltzmann temperature of 200 MeV [37]. If this is the case, fitting the antiproton invariant multiplicities with a flat function in p_t would underestimate the invariant multiplicity at $p_t = 0$ by less than 10%. This is certainly reasonable for the purposes of this comparison. Additionally, because the same fit will be used in each rapidity bin for all data sets, the relative distributions are still directly comparable. However, we will not concern ourselves here with the absolute scale of the measurements.

Figure 6-2 presents the results of the extrapolations to $p_t = 0$ for the antiproton invariant multiplicities. Here, the differences between the analyses become more apparent. The disagreement between the current analysis and the previous results at midrapidity is evident.

We may further assume a Gaussian form to the y dependence of the invariant multiplicities:

$$\frac{d^2N}{dy\,dp_t} \propto e^{-\frac{(y-y_{cm})^2}{2\sigma_y^2}} \tag{6.3}$$

Fitting to the determined invariant multiplicities at $p_t = 0$ yields a rapidity width $\sigma_y = 0.34 \pm 0.01$, as shown in Figure 6-2. Similar fits to the other data sets yield $\sigma_y = 0.44 \pm 0.01$ and $\sigma_y = 0.49 \pm 0.05$ for the 1995 and 1994 data respectively. If a fit is made to the 1996-1997 data points excluding the point at $2.4 < y < 2.6$, the new value for σ_y is 0.42 ± 0.2. So it appears that the shape of the data in rapidity agree for each of the three data sets below rapidity 2.4. However, the new data point at high rapidity makes a sharp difference in the fit to the rapidity distribution of the invariant multiplicities. Whether the difference is real or an artifact of the procedure used for determining invariant multiplicities of antiprotons is unclear. There are reasons to believe that the method used for determining the observed multiplicity of antiprotons in LET events in Section 5.1.5 may be flawed, particularly in the highest rapidity bin

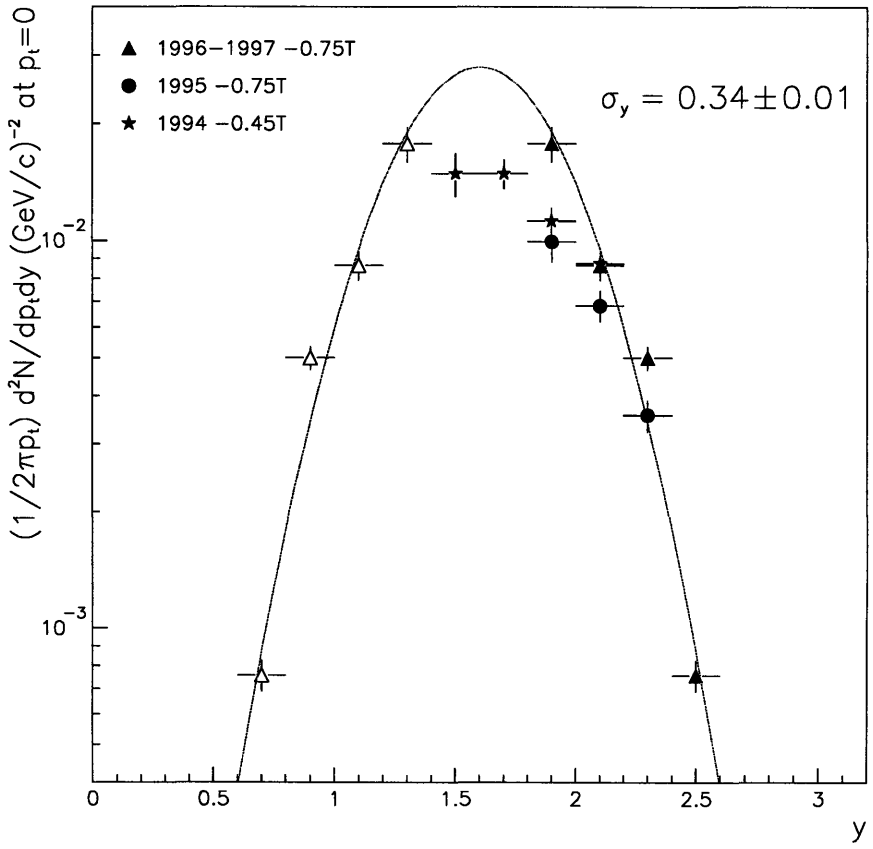

Figure 6-2: Comparison of antiproton invariant multiplicities extrapolated to $p_t = 0$ for different E864 analyses. The data from this analysis are labeled "1996-1997 - 0.75T". The hollow symbols below midrapidity ($y_{cm} = 1.6$) are the 1996-1997 points reflected about midrapidity.

where any timing fluctuations of the LET curve have the greatest impact. Additional factors from the differences in the data runs (discussed in Section 6.1.1) may also be more significant than we are aware.

But an investigation of the antiproton physics and counting techniques is not a goal of this thesis. That the antiproton invariant multiplicities found in this analysis are not unreasonable is evident. At this point, we have gained enough confidence in the analysis and data set to trust the results of our searches for negatively charged strangelets.

6.2 Negative Strangelet Results

6.2.1 Summary of Upper Limits

E864 cannot prove with absolute certainty whether any single candidate is in fact a strangelet. However, an operational and efficient S1 straw tube tracking chamber (or similar device) between the two dipole magnets of the spectrometer would be most beneficial in improving the confidence placed on any conclusions drawn from an individual candidate. It is unfortunate that this is not the case for this analysis. In that light, the remainder of this discussion will be made on the assumption that the strangelet candidate documented in Section 5.2.2 at charge -1, mass 7A is understood as background.

Table 6.1 summarizes the upper limits set on the production of negatively charged strangelets from this analysis. These are limits for strangelets which are stable, or have proper lifetimes of at least 50 ns in order to survive traversal of the entire spectrometer.[2] If strangelets are in fact produced with lifetimes under 50 ns, the probability that any will be seen in the E864 apparatus decreases with the probability of survival with shorter lifetimes, thereby increasing the upper limits. The two models used in calculating the upper limits in Table 6.1 are Model I and Model II from the parameterization below.

$$\frac{d^2N}{dy\,dp_t} \propto p_t e^{-\frac{2p_t}{<p_t>}} e^{-\frac{(y-y_{cm})^2}{2\sigma_y^2}} \tag{6.4}$$

Model I. $\sigma_y = 0.5,\ < p_t >= 0.6\sqrt{A}$

Model II. $\sigma_y = 0.5/\sqrt{A},\ < p_t >= 0.6\sqrt{A}$

Model III. $\sigma_y = 0.5,\ < p_t >= 0.5\sqrt{A}$

The upper limits for charge Z = -1 and charge Z = -2 strangelets are displayed in Figures 6-3 and 6-4 respectively, along with results from other experiments. The

[2]The quoted proper lifetime limit of E864 assumes production and detection of strangelets at midrapidity. The E864 apparatus requires a laboratory lifetime $t_{lab} > 100$ ns at midrapidity, where $\gamma_{cm} \approx 2$ and $\tau t_{lab}/\gamma > 50$ ns, in order to detect strangelets in the calorimeter.

Model	Charge (Z)	Strangelet Mass (GeV/c^2)	90% C.L. Upper Limit on Overall Multiplicity
I	-1	5	1.5×10^{-8}
I	-1	20	8.3×10^{-9}
I	-1	100	9.3×10^{-9}
II	-1	5	1.0×10^{-8}
II	-1	20	7.3×10^{-9}
II	-1	100	8.8×10^{-9}
I	-2	5	6.7×10^{-9}
I	-2	8	5.1×10^{-9}
I	-2	20	3.5×10^{-9}
I	-2	100	3.8×10^{-9}
II	-2	5	4.5×10^{-9}
II	-2	8	3.5×10^{-9}
II	-2	20	3.0×10^{-9}
II	-2	100	3.3×10^{-9}

Table 6.1: Final upper limits for negatively charged strangelets. The limits assume no unexplained candidates.

results from this analysis are shown as the "New E864" curves. The limits for masses between those specifically calculated in Section 5.2.4 have been interpolated under the assumption that the acceptances and efficiencies of strangelets vary smoothly with mass. The results from both Models I and II are shown in the two figures for charges Z = -1 and Z = -2 and typically agree within a factor of less than 1.5. Other experimental results are also included in the figures, as well as the previous limits set by E864 [21]. These are discussed below.

6.2.2 Comparison with Other Experiments

Previous E864

The previous upper limits for production of negatively charged strangelets set by E864 were found from the 1995 running of the experiment [21]. A similar analysis to the one detailed in this thesis was performed on a smaller set of data, and the same two models were examined for upper limits. The bulk of the difference between the

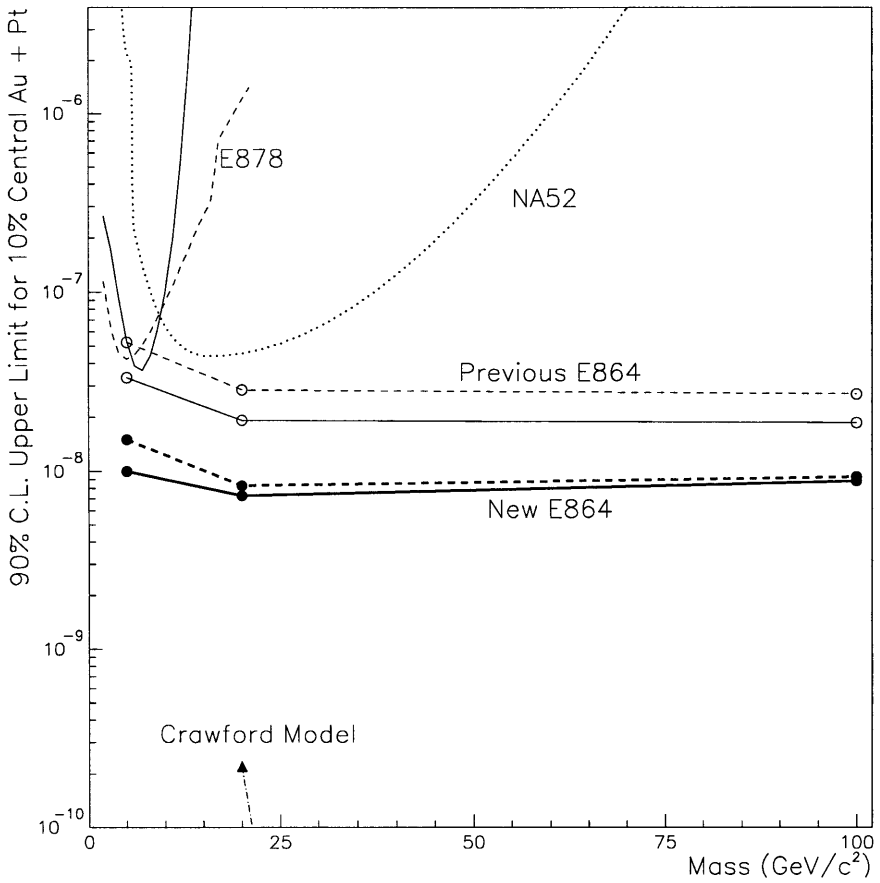

Figure 6-3: 90% confidence level for upper limits on charge Z = -1 strangelets produced in 10% central Au + Pt collisions at 11.6 A GeV/c. The limits from Model I are shown as dashed lines, while those from Model II are shown as solid lines. Also shown are previous limits from E864, limits from E878 using Models I and II, limits from NA52 using Model III (see Section 6.2.1), and the predicted production probabilities of the Crawford Model. See text for discussion.

previous upper limits and the new limits is due to the increased data sample. Other differences which are expected to contribute only minor effects include a different LET setup (see Section 2.6), a few small hardware changes, and a different target (the 1995 run used a Pb target of 30% interaction length, while the 1996-1997 run used 60% Pt). As these differences are not significant, the new upper limit curves reflect a similar profile to the previous limits and are in general a factor of approximately 3 better for charges Z = -1 and Z = -2.

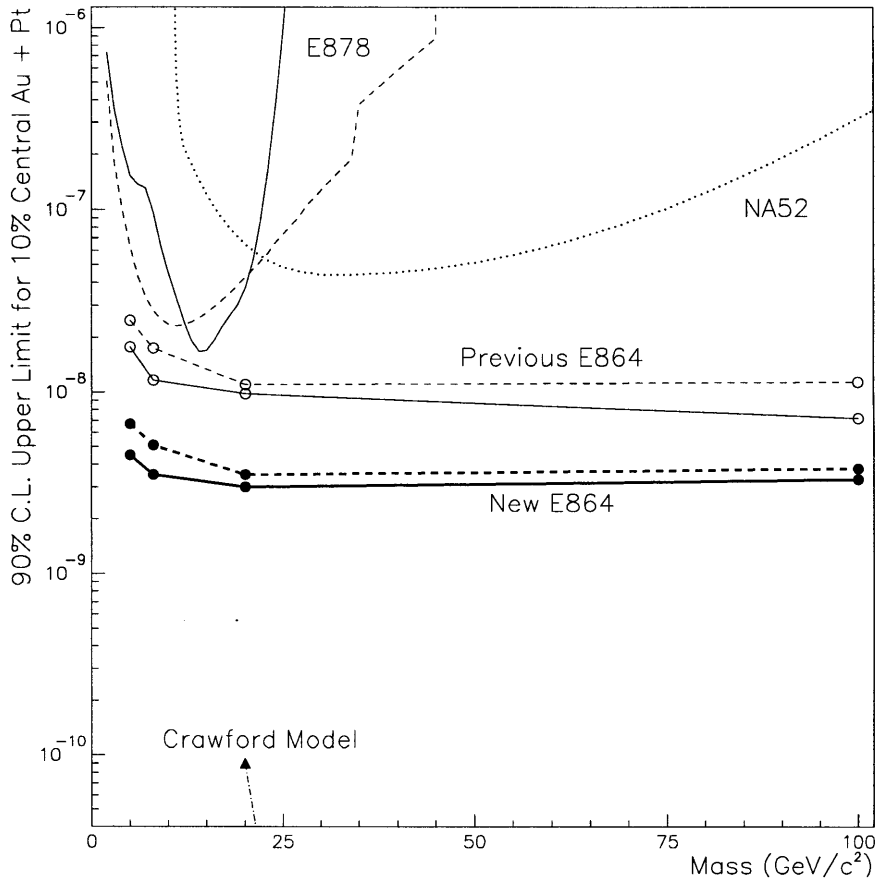

Figure 6-4: 90% confidence level for upper limits on charge Z = -2 strangelets produced in 10% central Au + Pt collisions at 11.6 A GeV/c. The limits from Model I are shown as dashed lines, while those from Model II are shown as solid lines. Also shown are previous limits from E864, limits from E878 using Models I and II, limits from NA52 using Model III (see Section 6.2.1), and the predicted production probabilities of the Crawford Model. [1]. See text for discussion.

E878

E878 was a focusing spectrometer experiment at BNL using Au + Au at 10.8 GeV/c per nucleon [38]. Their original strangelet production limits were set for minbias collisions and have been multiplied by a factor of 10 to quote limits for the 10% most central collisions here [20]. The acceptance efficiencies for a focusing spectrometer, which studies particles at fixed rigidities, are highly model dependent for strangelet production. Acceptance is limited in a range of p_t near zero, and at low rapidities for high masses. A sharp cut-off occurs at masses so large that the low rapidities

necessary to accept them are too slow for the active time gates of the experiment.

E878 applied the same two models, Model I and Model II above, to set their upper limits for charge Z = -1 and Z = -2 strangelets, as shown in Figures 6-3 and 6-4. These limits degrade for strangelets whose proper lifetimes are below ~100 ns. The previous E864 upper limits were comparable to the E878 limits at low masses as seen in the figures. This new E864 upper limits are clearly better than E878 in the low mass region where E878 has acceptance.

NA52

Another focusing spectrometer experiment was conducted at CERN using NA52 [39, 40]. This experiment used a Pb + Pb colliding system at a beam momentum of 158 A GeV/c to search for negatively charged strangelets [30, 41]. The published limits for NA52 were found for minbias events using Model III (described in Section 6.2.1), which differs from Model I in using $< p_t >= 0.5\sqrt{A}$ instead of $< p_t >= 0.6\sqrt{A}$. These limits have also been multiplied by a factor of 10 to quote limits for the 10% most central collisions. Again, the acceptance is highly model dependent and is better for their experiment in Model III than in Model I. Thus, the limits shown in Figures 6-3 and 6-4 from NA52 using Model III would be somewhat higher if Model I were used.

It is very important to note that NA52 examines a heavy ion colliding system at much higher energies than either E878 or E864. Strangeness production and the nature of the colliding systems is expected to be significantly different in these two energy regimes [1, 42, 43]. Additionally, strangelets which are detectable in the NA52 experiment are required to have lifetimes of $t_{lab} > 1.2$ μs.[3] Therefore one must be very careful about making any direct comparisons between the limits set by these experiments. While the upper limits set by E864 and E878 are essentially directly comparable in Figures 6-3 and 6-4, the NA52 limits are presented only as an example of what else has been done in the field of strangelet searches in heavy ion collisions.

[3] At midrapidity for NA52, $\gamma_{cm} = 9$. Thus, a midrapidity strangelet needs a proper lifetime of $\tau > 130$ ns for detection in the experiment.

6.2.3 Comparison with Theory

Also presented in Figures 6-3 and 6-4 are production probabilities for strangelets using a model detailed by Crawford et al. [44, 1] (herein referred to as the Crawford Model). This model assumes formation of a quark gluon plasma in every 10% central heavy ion collision above some minimum energy and minimum colliding system size. The QGP then breaks up into smaller QG drops which cool and may evolve into strangelets through kaon emission [45] and finally γ emission. The stability of these strangelets is determined through the mass formula derived by Berger and Jaffe for strangelets [11]. The Crawford Model has been empirically defined to match experimental data for strangeness production and the inclusion of surface effects on the stability of hyperonic particles. Unfortunately, these surface effects have been calculated to cause destabilization of strangelets at masses below $\sim$20A [46].

While uncertainties in some of the parameters of the model prevent us from taking these production probabilities as exact, they do at least provide for a qualitative comparison with the data. The inclusion of the destabilization of low mass strangelets from surface contributions to the energy densities has avoided comparisons at these low masses. Before this correction had been made, it had appeared that the upper limits from this analysis would be below the predicted production probabilities [44]. However, none of the new upper limits from this analysis are within an order of magnitude of the current predictions of the Crawford Model. At this point it can only be said that experiments have not yet pressed the Crawford Model.

Regardless, we may use the results of this analysis to place limits on the formation of QGPs which result in the production of negatively charged strangelets. If we take the probability of QGP formation from Au + Pt collisions at 11.6 A GeV/c to be a branching fraction (BF), and also consider the branching fraction of QGPs into negatively charged strangelets, then the upper limit on negatively charged strangelets can be expressed as follows:

$$\text{Upper Limit} = \text{BF}(\text{Au} + \text{Pt} \rightarrow \text{QGP}) \times \text{BF}(\text{QGP} \rightarrow \text{Strangelet}) \quad (6.5)$$

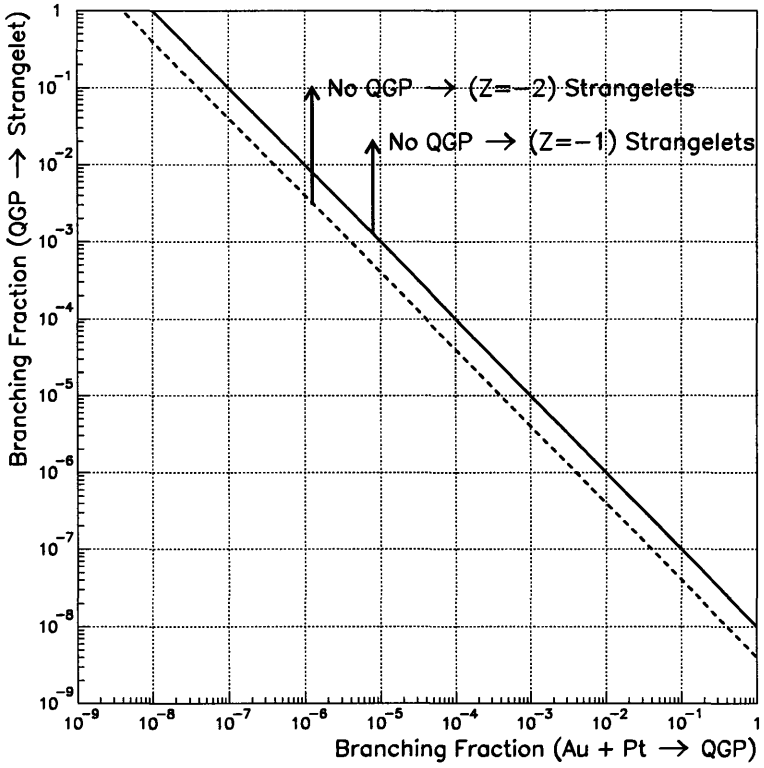

Figure 6-5: Branching fraction limits for distillation of negatively charged strangelets from a QGP.

The upper limits that have been found in this analysis are in general flat as a function of mass, and are similar for each of the two models selected. Thus, we can conservatively approximate an upper limit for the production of strangelets of each charge as a whole for central collisions. These global limits are selected at 1×10^{-8} for charge Z = -1 strangelets, and 4×10^{-9} for charge Z = -2. Using Equation 6.5 results in the diagram of Figure 6-5. Here we can see the region of branching fractions which have been ruled out by this analysis for distillation of negatively charged strangelets from a QGP in 10% central Au + Pt collisions at 11.6 A GeV/c.

Chapter 7

Summary

The primary goal of this research is to look for strange quark matter in the form of negatively charged strangelets produced in high energy heavy ion collisions. We use the E864 spectrometer experiment with the Alternating Gradient Synchrotron (AGS) at Brookhaven National Laboratory to investigate the 10% most central collisions of Au + Pt at 11.6 GeV/c per nucleon beam momentum. In this experiment, a specially designed high-mass trigger makes possible searches for exotic particle species with exceptional sensitivity, while an open geometry allows broad mass searches over large y and p_t ranges.

During data collection, the spectrometer is optimized for massive, negatively charged particles. Approximately 80% of the 287 million triggered and saved collision events are examined and calibrated for analysis. A technique for saving the calibrated data and improving analysis efficiency is designed and implemented with a Data Summary Tape (DST) method. The DST is used for subsequent analyses.

To understand the data set and analysis techniques better, a measurement is first made of the invariant multiplicities of antiprotons produced in these heavy ion collisions. A comparison of the invariant multiplicity distributions is made with previous measurements from the E864 collaboration. While some discrepancies are observed, the new measurements do not appear unreasonable. Invariant multiplicities are also found at higher rapidities than previously measured by E864. The results of the antiproton invariant multiplicities gives us confidence in searching for new matter in the

data set.

A search is conducted for strangelet candidates with masses greater than 5 GeV/c^2 for charges of Z = -1 and Z = -2. The search is restricted to stable or meta-stable (proper lifetimes $\tau \geq 50$ ns) strangelets for their detection with the E864 apparatus. A single candidate is observed with a mass of ~7A and charge negative one. This candidate does not constitute a conclusive signal for strangelets. We set 90% confidence levels on the upper limits for production of negatively charged strangelets in 10% central Au + Pt collisions at this energy at the level of approximately 1×10^{-8} for charge negative one strangelets, 4×10^{-9} for charge negative two strangelets.

These upper limits are the world's best to date and the most production model-independent for high mass strangelets. Current model predictions made on the production of negatively charged strangelets from a quark gluon plasma (QGP) are not tested by these limits. They do, however, allow us to set new limits on the branching fractions of Au + Pt collisions into QGPs from which negatively charged strangelets are formed.

With the commencement of physics using colliding Au beams at RHIC (the Relativistic Heavy Ion Collider) in 1999, no further strangelet searches at the AGS are planned at the present. Additionally, the 1998 run of experiment E864 did not spend any running time on strangelet searches. Therefore, the upper limits set on strangelets from this data set are expected to be the final limits from the AGS. Focus for the future of strange quark matter searches in heavy ion collisions are now directed towards RHIC and CERN.

Appendix A

Hodoscope Resolution Formulae

In order to find the time resolutions of the hodoscopes, one must look at the time residuals from tracks at each hodoscope plane. The residuals are the distributions of the difference between the time which a hodoscope says a particle passed through it, and the time which the particle's track indicates it passed through it. This track is a linear fit to the space-time points from the experiment's detectors, and its time at a hodoscope can be found by projecting the linear fit to the hodoscope.

The residuals can be found for tracks which are fit including the hodoscope under examination, and excluding it. Here, the widths of the distributions for the two residuals will be labeled σ_{in} and σ_{ex} respectively. The actual, intrinsic time resolution of the individual hodoscope is σ_{intr}. A tracking projection resolution σ_{proj} is defined to be the resolution associated with the projection of a track which was fit excluding the hodoscope. Using these quantities,

$$\sigma_{ex}^2 = \sigma_{intr}^2 + \sigma_{proj}^2 \tag{A.1}$$

because the exclusive residuals involve the difference of the projection times and the hodoscope times.

For an individual track, take ΔT_{proj} to be the true error of the measurement of the time projection of the track without using the hodoscope, and ΔT_{track} to be the

true error of the measurement for the track which includes the hodoscope in its fit.

$$\sigma^2_{proj} =< \Delta T^2_{proj} > \tag{A.2}$$

If ΔT_{intr} is then the true error of the time measurement from the hodoscope,

$$\sigma^2_{proj} = < \Delta T^2_{proj} > \tag{A.3}$$

$$\sigma^2_{intr} = < \Delta T^2_{intr} > \tag{A.4}$$

$$\Delta T_{track} = \left(\frac{\sigma\prime^2_{intr} \Delta T_{proj} + \sigma^2_{proj} \Delta T_{intr}}{\sigma\prime^2_{intr} + \sigma^2_{proj}} \right) \tag{A.5}$$

Equation A.5 is the formula for the error on a quantity which is the weighted average of two other quantities. Here, the weights are the reciprocals of the time resolutions squared. Since σ_{intr} is an unknown, an intial guess of $\sigma\prime_{intr}$ is used. Therefore, assuming ΔT_{proj} and ΔT_{intr} are uncorrelated, $< \Delta T_{proj} \Delta T_{intr} >= 0$,

$$\sigma^2_{in} = < (\Delta T_{intr} - \Delta T_{track})^2 > \tag{A.6}$$

simplifies to

$$\sigma^2_{in} = \sigma\prime^4_{intr} \frac{\left(\sigma^2_{intr} + \sigma^2_{proj}\right)}{\left(\sigma\prime^2_{intr} + \sigma^2_{proj}\right)^2} \tag{A.7}$$

$$= \frac{\sigma\prime^4_{intr} \sigma^2_{ex}}{\left(\sigma\prime^2_{intr} + \sigma^2_{ex} - \sigma^2_{intr}\right)^2} \tag{A.8}$$

$$\sigma_{intr} = \sqrt{\sigma^2_{ex} - \sigma\prime^2_{intr} \left(\frac{\sigma_{ex}}{\sigma_{in}} - 1 \right)} \tag{A.9}$$

The same equations apply to the y resolutions of the hodoscopes. In that case, the residuals must be found for the y positions of tracks.

Bibliography

[1] H. Crawford et al. *Phys. Rev. D*, 48:4474, 1993.

[2] A.R. Bodmer. *Phys. Rev. D*, 4:1601, 1971.

[3] S.A. Chin and A. Kerman. *Phys. Rev. Lett.*, 43:1292, 1979.

[4] G. Chapline and M. Nauenberg. *Phys. Rev. D*, 16:450, 1977.

[5] B. Freedman and L. McLerran. *Phys. Rev. D*, 17:1109, 1977.

[6] E. Witten. *Phys. Rev. D*, 30:272, 1984.

[7] J.D. Gjorken and L.D. McLerran. *Phys. Rev. D*, 20:2353, 1979.

[8] E. Farhi and R.L. Jaffe. *Phys. Rev. D*, 30:2379, 1984.

[9] R.L. Jaffe. *Phys. Rev. Lett.*, 38:195, 1977.

[10] M.S. Berger, B.S. Thesis, Massachusetts Institute of Technology, 1986.

[11] M.S. Berger and R.L. Jaffe. *Phys. Rev. C*, 35:213, 1987.

[12] F.C. Michel. *Phys. Rev. Lett.*, 50:677, 1988.

[13] J.W. Harris and B. Muller, preprint hep-ph/9602235. 1996.

[14] A.J. Baltz et al. *Phys. Lett. B*, 325:7, 1994.

[15] A. Rusek et al. *Phys. Lett. B*, 585:59c, 1995.

[16] C. Pruneau for the E864 Collaboration, contribution to Quark Matter 97 proceedings.

[17] J. Schaffner-Bielich et al. *Phys. Rev. C*, 55:3038, 1997.

[18] P. Stankus et al. *Nucl. Phys. A*, 544:603c, 1992.

[19] A. Rusek et al. *Phys. Rev. C*, 52:1580, 1995.

[20] D. Beavis et al. Search for new metastable particles produced in Au + Au collisions at 10.8 A GeV/c. *Phys. Rev. Lett.*, 75:3078, 1995.

[21] J. Nagle. PhD thesis, Yale University, 1997.

[22] J. Sandweiss et al. E864: Proposal for funding - measurements of rare composite objects and high sensitivity searches for novel forms of matter produced in high energy heavy ion collisions. 1991.

[23] D. Acosta et al. *NIM*, A294:193, 1990.

[24] T.A. Armstrong et al. The E864 lead - scintillating fiber hadronic calorimeter. *NIM*, A33:100, 1998.

[25] J.C. Hill et al. A late energy trigger for the E864 strangelet search experiment at the AGS accelerator. *Submitted to NIM A*, July 1998.

[26] K. Barish. PhD thesis, Yale University, 1996.

[27] J. Lajoie. PhD thesis, Yale University, 1996.

[28] M.J. Bennet et al. Antiproton distribution in Au+nucleus collisions. *Phys. Rev. C*, 56:1521, 1997.

[29] A. Chikanian et al. *NIM A*, 371:480, 1996.

[30] G. Ambrosini et al. Strangelet search and antinuclei production studies in Pb + Pb collisions. *Nucl. Phys. A*, 610:306c, 1996.

[31] S.D. Coe. PhD thesis, Yale University, 1997.

[32] J. Barrette et al. *Phys. Rev. Lett.*, 70:1763, 1993.

[33] T. Abbott et al. *Phys. Rev. C.*, 47:1351, 1993.

[34] G.E. Diebold et al. *Phys. Rev. C.*, 48:2984, 1993.

[35] T.A. Armstrong et al. Antiproton production in 11.5A GeV/c Au + Pb nucleus-nucleus collisions. *Phys. Rev. Lett.*, 79:3351, 1997.

[36] J.L. Nagle for the E864 Collaboration. Antiproton production and antideuteron limits from experiment E864. *J. Phys. G: Nucl. Part. Phys.*, 23:2145, 1997.

[37] The E866 Collaboration, H. Sako et al. Heavy Ion Physics at the AGS (HIPAGS 96), edited by C.A. Pruneau, G. Welke, R. Bellweid, S.J. Bennett, J.R. Hall, and W.K. Wilson (Wayne State University Report No. WSU-NP-96-16, 1996).

[38] M.J. Bennet. PhD thesis, Yale University, 1995.

[39] K. Borer et al. *Phys. Rev. Lett.*, 72:1415, 1994.

[40] G. Appelquist et al. *Phys. Rev. Lett.*, 76:3907, 1996.

[41] G. Appelquist et al. Strangelet search in Pb-Pb interactions at 158 GeV/c per nucleon. *Phys. Rev. Lett.*, 76:3907, 1996.

[42] T. Abbott et al. *Phys. Rev. Lett.*, 64:847, 1991.

[43] E. Andersen et al. NA36 Collaboration. *Phys. Lett. B*, 294:127, 1992.

[44] H. Crawford et al. *Phys. Rev. D*, 45:857, 1992.

[45] H. Liu and G.L. Shaw. *Phys. Rev. D*, 30:1137, 1984.

[46] J. Madsen. *Phys. Rev. Lett.*, 70:391, 1993.